INVESTIGATION OF THE SURFACE-ELECTROLYTE INTERFACE OF SEMICONDUCTORS AND METALS

BY

DENNIS P BUTCHER

DISSERTATION

Submitted in partial fulfillment of the requirements
for the degree of Doctor of Philosophy in Chemistry
in the Graduate College of the
University of Illinois at Urbana-Champaign, 2012

Urbana, Illinois

Doctoral Committee:

Professor Andrew A. Gewirth, Chair
Professor Gregory S. Girolami
Professor Kenneth S. Suslick
Professor Catherine J. Murphy

Abstract

This thesis focuses upon investigating the interface between semiconductors or metals with electrolyte. Understanding the interfacial dynamics are important to improving process performance, whether investigating photocatalytic systems or the nature of adsorption and reaction dynamics on metal surfaces.

The first project presents the photoelectrochemical characteristics of $TlVO_4$, a previously uncharacterized candidate for photocatalytic water splitting. Additionally, a composite of $InVO_4$ and $TlVO_4$ was synthesized by a facile solution method using orthorhombic $InVO_4$ as a seed for growth of crystallographically similar orthorhombic $TlVO_4$. Photoelectrochemical measurements indicate an increase in photocurrent and more negative flatband potentials for $TlVO_4$ and the $InVO_4$:$TlVO_4$ composite relative to $InVO_4$. Diffuse reflectance UV-visible measurements were used to determine bandgaps of 3.50 eV, 2.94 eV, and 2.98 eV for $InVO_4$, $TlVO_4$, and $InVO_4$:$TlVO_4$, respectively. DFT calculations were performed to elucidate the band structures and correlate well with experimental data. The results indicate higher photoelectrochemical activity for $TlVO_4$ and the $InVO_4$:$TlVO_4$ composite relative to $InVO_4$.

The second project investigates the potential dependent assembly of 2,2'-bipyridine molecules on both Au(100) and Au(111) surfaces using a newly developed SHINERS technique. We present potential dependent SHINERS spectra of 2,2'-bipyridine adsorbed on both surfaces collected under anodic as well as cathodic polarization. A series of processes were characterized by the analysis of the data set with Perturbation Correlation Moving Window Two Dimensional Spectroscopy (PCMW2D) and Two Dimensional Correlation Spectroscopy (2DCOS). Exquisite spectral detail was achieved and allowed for the characterization of complicated ring breathing mode and C-C inter-ring stretching modes that are diagnostic of molecular orientation on the

surfaces. Detection of several occluded vibration peaks was also made possible with SHINERS. Analysis reveals that in very negative potentials, 2,2'-bipyridine adsorbs in a disordered, mixed state with both π-flat cis and several different vertically N-bound cis orientations, in contrast to previously published reports. Our findings provide insight into 2,2'-bipyridine adsorption on Au single crystals and also powerfully combine SHINERS with two dimensional correlation analysis to yield a more detailed view of spectral transitions.

The third project details the origin of differential nitrate reduction activity between the (100), (111), and (110) faces of Cu using vibrational spectroscopy and calculations. Shell isolated nanoparticle enhanced Raman spectroscopy (SHINERS) reveals a suite of intermediates from the nitrate reduction process on Cu(100), Cu(111), and Cu(110) including NO_2^- and HNO. All three faces show similar intermediates, suggesting the same mechanism is operative on all of them. Critical to the reduction pathway on the bare Cu surfaces is the autocatalytic reduction of nitrate to nitrite concomitant with partial oxidation of the Cu surface. This priming action facilitates nitrate reduction and reduces overpotentials, particularly on the Cu(111) and Cu(110) faces, which are more susceptible to oxidation. Calculations show that the trend in activity between the different single crystal faces of Cu follows the strength of the adsorption of intermediates on the corresponding oxides; this trends was not found in calculations on the bare metal surfaces. Decoration of the surfaces with Cl^- suppresses nitrate autocatalysis, resulting in higher overpotentials and lower current density. NH_3 is observed by SHINERS as a direct nitrate reduction product in the presence of Cl^-, rather than NO_x species observed on the bare Cu surfaces, indicating a reaction pathway unique from the bare, undecorated surface.

The fourth project examines the coadsorption of water and potassium on a Au(100) surface using variable temperature Scanning Tunneling Microscopy (STM). The two-layer

system initially formed on the reconstructed Au(100) through addition of K is converted into a labyrinthine row structure upon the introduction of water. This structure features KOH molecules likely covered with a water adlayer. Density Functional Theory (DFT) calculations provide further insight into the observed labyrinthine striped structures formed by adsorbed KOH. Images obtained following limited introduction of water feature larger unreacted areas and a more disordered row structure.

For My Girls

Kendra, Allison, and Kennedy

Acknowledgements

Many people have helped me to learn, succeed, and grow throughout my life. It all starts with my parents, Rebecca Wojno and Dennis Butcher Sr. Your guidance kept me on track and motivated. Your encouragement helped me through difficult times, especially in high school. You gave me support when I needed it and pushed me to become independent and self-sufficient when the time was right. So thank you for all you've done.

I've had many teachers and professors who've had an enormous impact on my life as well. Mr. Matt Young from high school chemistry first sparked my interest in the field that has become my passion. Mrs. Sue Korosa, Mrs. Alice Rote, and Mr. Andy Stevens gave generously of their time to support Copley High School's Academic Challenge team. My four years competing on the team was a fun time, and I learned more from our coaches than I ever did from a class or a book.

Once I graduated from Copley and moved on to Ohio University, I received excellent direction from the Department of Chemistry. Dr. Karen Eichstadt provided incredible academic advising and presented me with opportunities to conduct Peer Led Team Learning (PLTL) mentoring sessions as well as undergraduate laboratory teaching. She also referred me to Dr. Jeff Rack to perform undergraduate research in his laboratory during my freshman year. At the time, I was unsure of what I wanted my career path to be, but that changed quickly as I started to work with Jeff and graduate students Aaron Rachford and Nicholas Mockus. The research was exciting and showed me the link between what is learned in the classroom and how it is applied in the laboratory. Jeff, Aaron, and Nick worked with me extensively over the course of three years. I can say with certainty that my experience with them, and the broader department, forged me into a scientist and pushed me to seek a graduate degree in chemistry.

I have been fortunate to work with many talented researchers here at Illinois. I appreciate the direction and encouragement from my advisor, Dr. Andrew Gewirth, during my time here. I've also had tremendous assistance from Matt Thorseth during my work with metal oxide photocatalysts. Once I transitioned to spectroscopy based projects, Jeremy Hatch, Brandon Long and Nicole Honesty took the time to assist me with learning new instruments and techniques.

While I appreciate the time and effort of my colleagues to assist my development, the most important contribution to my success has been my wife Kendra. She has been there to support and encourage me when I wanted to give up on graduate school, and she has provided inspiration through her own efforts to obtain a nursing degree while working. I couldn't have done this without her. My daughters Allison and Kennedy have been my motivation to keep pushing through the frustration and difficulties of earning a Ph.D. I hope I've made them proud, and I thank everyone, mentioned and unmentioned, for helping me to discover and start my career.

Table of Contents

Chapter 1. Introduction

Charge transfer at interfaces is a fundamental chemical event of great importance within a broad set of disciplines. One of the overarching goals of a chemist is to understand the flow of charge and matter at the interface. With this knowledge, the process can be controlled or modified to generate desired products or improve yields. These goals are central to the work presented in this thesis, whether through photochemically driven catalytic reactions to generate hydrogen or through electrochemically driven adsorption and reaction processes on metal surfaces. In each case, the nature of the solid-electrolyte interface is explored to give some explanation to how adsorption or reaction processes proceed and to give insight into how this information can prove useful to future investigations.

Photocatalysis

For decades, the prospect of an emerging solar hydrogen based economy to phase out the existing fossil fuel dependent economy has been a goal sought by policymakers and environmentalists alike. Transitioning to solar hydrogen has the potential to eliminate political, security, and economic concerns regarding the origin of some fossil fuels in unstable regions of the world. More relevant from a scientific perspective, solar hydrogen generation has clear environmental benefit by removing the greenhouse gas emissions of traditional fuels such as coal, petroleum, and natural gas.[1-8]

Energy from the sun is virtually limitless. As a point of reference, more energy strikes the Earth's surface in one hour than the amount of energy demand worldwide for an entire year.[2] Unfortunately, the solar energy flux at a particular spot on the Earth's surface is low. Nature has dealt with this obstacle by covering a significant portion of the planet's land and ocean surfaces with photosynthetic organisms to convert sunlight into useful chemicals; as a result, the sun

provides for almost all of the planet's biological energy needs through the action of photosynthesis, even though the process is typically only around 1% efficient.[9] This option is not ideal for human energy needs, however, because significant areas of land are required to generate enough power to replace traditional energy sources with today's technology. Thus, significant research effort is directed to improving solar energy technology to not only increase efficiency, but also to make energy systems more adaptable to existing developed land and structures.[10-14]

Ultimately, even with efficiency and cost improvements, solar energy and its derivatives (wind, wave) are limited by the intermittent nature of energy conversion. The sun doesn't always shine just as the wind does not always blow. Because of this drawback, engineering and chemical solutions have been investigated to store excess energy that is produced at off-peak demand times in order to provide a steady, reliable, on-demand power supply. Methods to achieve this goal include storage of energy as heat in salts, pumping water, and direct conversion of solar energy into chemical fuels for later use.[15] One of the chemicals proposed to store solar energy is hydrogen. About 95% of the total hydrogen supply comes from steam reforming of methane, which is not a carbon neutral process, with only about 5% generated by electrolyzers run by solar arrays. Electrolyzers are themselves limited to electricity to hydrogen efficiencies of only 65%, and are as a result another limiting factor to photovoltaic driven hydrogen production.[16] When powered by affordable photovoltaics, often less than 20% efficient turning sunlight to electricity, the effective photon to hydrogen efficiency of the entire system is around 10%.[16]

Thus, significant research has been conducted to allow the direct generation of H_2 from semiconducting materials in water, rather than relying on a solar array/electrolyzer system.

Fujishima and Honda were the first to demonstrate this photocatalytic effect on TiO_2 crystals immersed in solution.[17] After this discovery, many particulate photocatalysts have been reported that have the added benefit of a greater surface area to allow more efficient use of photogenerated charges.[4, 18-21] Additional benefits to direct water photocatalysis are a simpler, self-contained cell with a potential for much lower material processing costs and greater flexibility in how the system can be designed.[4] While particulate photocatalysts show some promise, the highest reported photocatalytic efficiency is around 2.5%.[22] Thus, much research is left to elevate water-splitting photocatalysts to economic viability for the direct production of hydrogen from sunlight.

One of the significant challenges of designing water-splitting photocatalysts, is to understand the complex interface between the semiconductor and electrolyte and how engineering the band structure of the material can lead to more effective use of photogenerated charge carriers. Since the particles are both the solar collectors and the catalytic site of water reduction and oxidation, exquisite control over the band position and species present on the surface is a necessary condition for effective photocatalysts.[23] Synthetic techniques to incorporate different metals into the corrosion resistant oxide materials have been shown to influence conduction and valence band positions.[16, 24] Photoelectrochemical analysis provides information regarding the reaction of surface species with the photogenerated charge carriers and is used to evaluate the effects of band engineering on the photocatalytic materials detailed in Chapter 3.

Surface Adsorption and Reactivity

The association of water with cations and anions at metal surfaces is central to many processes. The fundamental significance of solvation of ions is very clear in the realm of

electrochemistry. Most of electrochemical reactions take place in the electrochemical double layer which is composed of solvent molecules, ions, and the metal surface.[25] Thus, one key to understanding the chemistry of many interesting reactions and processes is to learn about the nature of the metal and electrolyte interface. One particularly relevant example is the solvation and desolvation of Li^+ and other cations, which forms the basis of battery technologies.[26-28] Studies have been conducted for decades in order to elucidate the structure and properties of the electrochemical double layer.[29-33]

The surface and electrolyte interface is also critically important for the mediation and catalysis of a wide range of useful reactions. Some prominent examples include the oxygen reduction reaction (ORR) for fuel cell applications or the reduction of NO_3^- on a wide array of different metals including Pt, Pd, and Cu for environmental remediation or chemical manufacturing.[34-38] The adsorption of the reactant to the catalytic surfaces facilitates the making and breaking of bonds critical to each process. Discovering the modes of reactant binding to the surface and how such binding assists the formation of desired products aids in the design and choice of materials for ever more efficient electrocatalysts.

Another area where the nature of the surface and electrolyte interaction is important is in the field of corrosion and polishing, particularly in relation to the microelectronics industry. Chemical mechanical planarization (CMP) is used to remove overlayers of Cu leftover from Cu electroplating processes during the manufacture of integrated circuits.[39] CMP slurries are typically composed of chelating agents, oxidizers, corrosion inhibitors, buffers, surfactants, and abrasives.[40] An understanding of the surface interactions of the various CMP slurry components with the surface is critically important to formulating effective and efficient planarization mixtures.

Raman spectroscopy is proposed as an effective means of probing surface adsorbed molecules to provide insight into the structure of the surface electrolyte interface and the implications of that structure toward film formation and small molecule reactivity. Since Raman interrogates inelastic scattering of visible light, rather than absorption of infrared light, the technique experiences minimal attenuation is common solvents (water). Raman provides a highly specific chemical fingerprint, with some vibrational frequencies of molecules being extremely sensitive to orientation on the surface. Additionally, no tags or markers are necessary to enable measurements and the technique is highly versatile, allowing data of solid, liquid and gas phases. Unfortunately, molecules typically exhibit Raman scattering cross sections of around 10^{-29}, resulting in low signal and poor surface selectivity.[41]

Because of these drawbacks, significant effort has been devoted to increasing surface sensitivity and signal intensity of Raman scattering. These efforts led to the development of surface enhanced Raman spectroscopy (SERS).[41-42] SERS enhances the signal by exciting surface plasmons on the substrate, which when in resonance with the incident photons amplify the electromagnetic (EM) fields at the interface. These plasmons are typically parallel to the surface, so at a smooth interface, EM enhancement occurs only parallel to the plane of the surface.[41] In order to achieve enhancement into the electrolyte, features smaller than the wavelength of incident photons are necessary to activate dipole oscillations, which are perpendicular to the surface. Surface roughness is generally imparted by deposition of nanoparticles or electrochemical roughening procedures. In these conditions, both the incident and scattered photons are enhanced and result in an enhancement of scattering from the target analyte. An additional requirement for strong enhancement is that the metal chosen should

contain plasmons that are in resonance with the visible radiation source, which generally limits substrates to the coinage metals of Cu, Ag, and Au.[41]

SERS produces strong signal enhancement, but is still limited by the fact that single crystal surfaces cannot be interrogated and the choice of substrate metal is confined to Cu, Ag, and Au. Many chemical processes experience different rates or reaction mechanisms at different crystal facets, making spectroscopic understanding of adsorption dynamics to these surfaces of great interest. Even deposition of enhancing nanoparticles, such as Ag, on a non-enhancing surface yield unsatisfying results because signal could originate from adsorption of analyte to the surface of interest, or from adsorption to the particles themselves. Efforts have been made in recent years to overcome this constraint using a probe microscopy tip as the enhancement probe and rastering it over the surface and electrolyte interface of a non-enhancing material. Tip enhanced Raman spectroscopy (TERS) can provide spatial resolution, but is limited by low detection sensitivity and fouling of the tip by molecules in solution, which can lead to unreliable or inconclusive results. Other efforts have been directed to coat enhancing surfaces or nanoparticles with thin coatings of non-enhancing metals to take advantage of the long range EM enhancement from the underlying particles, but without any interference from direct adsorption of analyte to the enhancing structures.[41] Ultimately, this technique disallows investigation of single crystal surfaces and may give an incomplete picture of the surface electrolyte interface because of differences in the characteristics of thin metal films and bulk metals.

In order to address these issues of low signal, poor selectivity, and interference from the enhancement probes, the shell isolated nanoparticle enhanced Raman spectroscopy (SHINERS) technique was developed by Li and coworkers.[43-46] A Raman enhancing core of Au, or more recently Ag[47], is coated with a thin insulating film of SiO_2 to isolate the metal nanoparticle from

the electrolyte. Since analyte cannot adsorb or react on the Au surface, there is no longer interference from such processes in collected spectra. With coatings on the order of 3-5 nm, the EM enhancement mechanism is still strong and provides more than enough signal enhancement to obtain good spectra. These particles provide a significant amount of versatility since the choice of substrate is no longer constrained by having to choose Cu, Ag, or Au. Raman enhancement has been demonstrated on non-enhancing surfaces, even detecting the presence of pesticides on an orange peel in one example and H adsorption on Pt.[43] More importantly from the perspective of the electrochemical surface electrolyte interface, adsorption at single crystal surfaces can now be examined because roughening procedures are no longer required and deposited nanoparticles no longer impart signal interference.

Thus, SHINERS is an ideal spectroscopic method to probe the orientation and composition of adsorbed films on a diverse set of substrates and to monitor electrocatalytic reaction processes, as detailed in Chapters 4 and 5.

Research Goals

The goal of the research described in this dissertation is to improve our understanding of dynamic reaction processes on a diverse set of surfaces including semiconductors and metals. Additionally, new methods, particularly SHINERS were adapted and improved to enable the identification of reaction intermediates and to determine the nature specifically adsorbed films to a surface of interest.

Chapter 3 details my work developing metal oxide semiconductors to enable direct photocatalytic water-splitting. $InVO_4$ and $TlVO_4$ were explored as candidate materials, along with a composite of the two, to investigate the effects cation substitution and composite formation on photocatalytic activity. The morphology and composition of the synthesized

nanoparticles is described along with photoelectrochemical evaluation of water-splitting activity. DFT calculations provided insight into the relative activities of materials on the basis of the calculated bandgap as well as orbital composition of the valence and conduction bands.

Chapter 4 presents my findings regarding 2,2'-bipyridine adsorption to Au single crystal surfaces. The SHINERS technique is used to determine the spectral signature of various conformations of 2,2'-bipyridine on the surfaces and gives a detailed account of the transformation of the surface film during potential scanning. 2D correlation analysis is used to deconvolute complicated spectral regions to support the analysis of the surface dynamics.

Chapter 5 moves on from surface adsorption phenomena and explores the differential activity of the low Miller index faces of Cu toward nitrate reduction. SHINERS and linear sweep voltammetry reveal unique nitrate reduction intermediates. Comparison to Cl^- surfaces gives insight into the surface mediated reaction mechanism, which is supported by calculations using VASP.

Chapter 6 provides details of the adsorption of hydrated potassium under UHV conditions to a Au(100) surface. DFT calculations complement STM observations to explain geometrical ordering of potassium species on the surface.

All of these studies contribute to the known literature about the interaction of adsorbing or reactant molecules with a semiconducting or metal electrode.

Chapter 2. Experimental Procedures

General Procecures

All glassware and electrochemical or spectroscopic cells were extensively cleaned in order to remove potential contaminants. The equipment is first rinsed well with DI water and then transferred to a bath with sulfuric acid and NoChromix (Godax Laboratories) to soak for several hours to remove organic contamination. The residue from the sulfuric acid bath is rinsed away with DI water and then the equipment is placed in a 35% nitric acid bath to remove metal contaminants. Nitric acid is removed by DI water and then all equipment is rinsed with boiling Milli-Q water (18.2 MΩ) prior to use.[36]

Standard solutions for adsorption and reactivity studies on Cu and Au were prepared from ultrapure nitric acid (J.T. Baker – Ultrex II), sodium nitrate (99.999%, Fluka), sodium nitrite (ReagentPlus, Aldrich), pyridine (Fisher Scientific, Certified ACS), 2,2'-bipyridyl (Sigma-Aldrich, ReagentPlus >99%), $HClO_4$ (J.T. Baker – Ultrex II), $KClO_4$ (Alfa-Aesar, ACS 99-100%), and Milli-Q water (18.2 MΩcm, Millipore Inc.).

Preparation of $InVO_4$

1 g (.0085 mol) NH_4VO_3 (Sigma-Aldrich, 99+% ACS Reagent Grade) was dissolved in 125 mL of 60°C water (Milli-Q UV Plus, 18.2 MΩ) and 3.342 g (.0085 mol) $In(NO_3)_3*xH_2O$ (Aldrich, 99.9% metals basis) was dissolved in 25 mL of water. After dissolution, the NH_4VO_3 solution was cooled to room temperature. $In(NO_3)_3*xH_2O$ solution was added to NH_4VO_3 solution resulting in a yellow/orange suspension. The suspension was heated to 100°C and stirred under reflux conditions for 24 hours. A yellow powder was isolated by vacuum filtration, washed with water (3 × 50 mL) and acetone (3 × 15 mL), and allowed to air dry.

Preparation of $TlVO_4$

0.1319 g (0.001125 mol) NH_4VO_3 was dissolved in 145 mL of 60°C water and 0.5 g $Tl(NO_3)_3*3H_2O$ (Aldrich, 98%) was dissolved in 5 mL of water with 5-10 drops of HNO_3 (Fisher, certified ACS Plus). After dissolution, the NH_4VO_3 solution was cooled to room temperature. $Tl(NO_3)_3*3H_2O$ solution was added to NH_4VO_3 solution to immediately yield an orange suspension. The suspension was heated to 100°C and stirred under reflux conditions for 24 hours. An orange/brown powder was isolated by vacuum filtration, washed with water (3 × 50 mL) and acetone (3 × 15 mL), and allowed to air dry.

Preparation of $InVO_4$:$TlVO_4$ composite

0.1319 g NH_4VO_3 was dissolved in 140 mL of 60°C water and 0.5 g $Tl(NO_3)_3*3H_2O$ was dissolved in 5 mL of water with 5-10 drops of HNO_3. After dissolution, the NH_4VO_3 solution was cooled to room temperature and 0.258 g (0.001125 mol) $InVO_4$ was added to create a yellow suspension. To this suspension, the $Tl(NO_3)_3*3H_2O$ was added dropwise (<1 drop per second), creating a tan/brown suspension. The suspension was stirred at 100°C under reflux conditions until a yellow suspension returns (1 hour). This yellow powder was isolated by vacuum filtration, washed with water (3 x 50 mL) and acetone (3 x 15 mL), and allowed to air dry.

Physical Characterization Methods

Powder X-ray diffraction (XRD) measurements were collected using a Rigaku D-MAX diffractometer using Cu Kα radiation operated at 45 kV and 20 mA, 1.5°/min scan rate, 0.02° step size. Samples were mounted on a glass slide using two-sided tape. Elemental analysis determined sample composition and purity. Transmission electron microscope (TEM) images were collected using a JEOL 2100 Cryo operating at 200 kV with samples supported on lacey

Formvar/carbon 200 mesh copper grids (Ted Pella, Inc.). EDS spectra were collected using a JEOL 2010F STEM equipped with an EDS probe. Diffuse reflectance UV-visible measurements were taken using a Varian Cary 5G spectrophotometer and transformed into absorbance units by the Kubelka-Munk relationship $\frac{K}{S} = \frac{(1-R)^2}{2R}$ where R is reflectance, K is the absorption coefficient, and S is twice the scattering coefficient[48].

Photoelectrochemical Measurements

Working electrodes were constructed by depositing sample onto indium tin oxide coated glass slides (70-100Ω/sq surface resistivity, Aldrich) previously rinsed with isopropanol. Sample slurry in ethanol was dropped onto an area marked off by scotch tape. After being air dried with the tape removed, electrodes were heated at 200°C for 12 hours. Copper wire was brought into contact with ITO using InGa eutectic (99.99+%, Aldrich) and adhered using epoxy. Electrochemical measurements were performed using a CHI 760C bipotentiostat (CH Instruments) with a platinum gauze counter electrode and a Ag/AgCl reference electrode. All potentials are reported in reference to Ag/AgCl. A xenon arc lamp (Newport) operated at 150 W and equipped with a water filter was used to irradiate samples from the back side of the electrode, which reduces the influence of semiconductor film thickness[49]. The photoelectrochemical cell has a circular sample port of 1 cm diameter, which allows for an electrode area of 0.785 cm^2. A 0.1 M K_2SO_4 (99.99% metals basis, Aldrich) solution, adjusted to pH=4 by H_2SO_4,was used as the electrolyte. Electrolyte was purged for 20 minutes with Ar before measurements and a positive Ar pressure over the solution was maintained during experiments. The apparatus was fitted with a 400 nm cutoff filter (Edmund Industrial Optics) to test visible light response.

Band Structure Determination

Density Functional Theory[50] calculations were performed using CASTEP[51] code within Materials Studio 4.4 (Accelrys)[52]. Three dimensional periodic cells were constructed from the published space group and crystal structure parameters of $InVO_4$[53] and $TlVO_4$[54]. Atomic coordinates were approximated for $TlVO_4$ because of lack of published data; the structure was geometrically optimized before proceeding. The band structure of the composite was obtained by layering the cell of $InVO_4$ with that of $TlVO_4$ to form a new supercell containing the unit cell of both materials. Calculations were performed within the generalized gradient approximation (GGA)[55-56] using the Perdew-Burke-Ernzerhof (PBE)[57] exchange-correlation functional. Band structure and partial density of state determinations were carried out with ultrasoft pseudopotentials, 4x4x3 k-point density, $5.0x10^{-7}$ eV/atom SCF tolerance, density mixing electronic minimization, fixed orbital occupancy, 380 eV energy cutoff, and density of states integration by the interpolation method.

SHINERS particle synthesis

A modification of the previously reported method to make SHINERS particles was used.[43, 45] Gold (III) chloride trihydrate, sodium citrate, (3-aminopropyl) trimethoxysilane (APS), sodium silicate solution (26.5 % SiO_2) were purchased from Sigma Aldrich. We followed the Turkevich method to synthesize the spherical gold nanoparticles.[58] The synthesis was carried out in a clean 200 mL conical flask. To this flask 2.5 mL of 0.01 M gold chloride trihydrate was diluted to 100 mL of deionized water. The solution was subsequently heated to boiling. To the boiling solution 10 mL of (10 mg/mL) sodium citrate solution was added, and further boiled for about ten more minutes. The final red colored solution was cooled and the

volume was adjusted to 100 mL with deionized water. The solution was purified by centrifugation (8600 rcf, 20 minutes) to remove excess citrate.

The silica layer was applied to the surface of the gold nanoparticles based on a protocol published by Liz-Marzan et al.[59] and modified by Li et al.[44] To 30 mL of the purified citrate nanoparticle solution, 0.4 mL of APS (1 mM) was added under vigorous magnetic stirring. After 30 minutes, 3.2 mL of sodium silicate (0.54 wt %, at pH 9.5 to 11 adjusted with HCl) was added to the solution and reacted for 2-3 minutes. The solution was placed in a hot water bath at 90 °C for 30 minutes and then cooled by placing in ice. The obtained silica capped gold nanospheres solution was purified through a centrifugation step at 2,200 RCF for 30 minutes followed by dialysis against pure deionized water using 10,000 MWCO dialysis cassettes (Thermo Scientific). Dialysis was carried over a period of 48 hours, and the water was changed at least four times during this period of time. The obtained silica coated gold nanoparticles were characterized by transmission electron microscopy (TEM) and are presented in Figure S1. The Au core was found to be 16.7 nm ± 1.8 nm with a shell thickness of 2.6 nm ± 0.7 nm.

Solutions were prepared from purified water (Milli-Q UV plus, 18.2 MΩ cm), $KClO_4$ (Alfa-Aesar, ACS, 99-100%), pyridine (Fisher Scientific, Certified ACS) and 2,2'-bipyridyl (Sigma-Aldrich, ReagentPlus ≥99%).

SHINERS Particle Validation

SHINERS particles dropcast on glassy carbon were interrogated by electrochemical measurements to determine whether there was any exposed Au. Batches used in these measurements did not show any evidence for the Au oxide stripping peak in 0.5 M H_2SO_4. (see supporting information Figure S2) Cyclic voltammetry in a 1 mM 2,2'-bipyridine, 0.1 M $KClO_4$

solution, both with and without SHINERS particles exhibited broadly similar features to each other consistent with previous reports of 2,2'-bipyridine on Au.[60-61] This implies that the presence of SHINERS particles does not significantly perturb the adsorption of 2,2'-bipyridine when compared to a bare surface, consistent with the observations of Huang et al. of pyridine on a smooth silver surface.[42]

Au Surface Preparation

Before each experiment, 1 cm diameter Au(100) and Au(111) single crystals (Monocrystal, Inc.) were mechanically polished using successively finer grits of 9, 3, 1, and 0.25 μm diamond paste (Buehler). The crystals were sonicated in purified water after each level of grit and were subsequently annealed in a hydrogen flame for 3 minutes. The crystal was allowed to cool in air for 10 minutes. The SiO_2 coated Au nanoparticle suspension was then dropcast onto the polished, flamed Au single crystal and dried under a gentle flow of Ar (2 times).

Copper Surface Preparation

Before electrochemical and SHINERS experiments, 10 mm diameter discs of Cu(100), Cu(110), and Cu(111) (Monocrystals, Inc.) were polished to a mirror finish using 9, 3, 1, and 0.25 μm diamond suspensions (Buehler), sequentially. The crystals were sonicated after each level of grit. The crystals were then electropolished in 50/50 v/v% H_3PO_4/H_2O,[62] and then rinsed with copious amounts of Milli-Q water. For SHINERS and some electrochemical experiments, the SiO_2-coated Au nanoparticles were then dropcast onto the Cu electrodes and allowed to dry under gently flowing Ar.

Cyclic Voltammetry for Copper and Gold crystals

Cyclic voltammetric data (CV) were obtained in a two-compartment, glass electrochemical cell, as previously reported.[63] The Au or Cu crystal was placed in the cell in a hanging meniscus configuration. The solutions were purged with Ar prior to use, and an Ar atmosphere was maintained in the cell during all electrochemical measurements. Scan rates for measurements were 50 mV/s.

Raman Measurement Parameters

Raman spectra were collected using previously described cells[64] and instrumentation.[65-66] A HeNe laser (632.8 nm) was used as the excitation source. The acquisition time at each potential was 30 s with 0.05 V potential steps between acquisitions for 2,2'-bipyridine studies on Au while 120 s acquisition times with 0.05 V potential steps were used for nitrate reduction studies on Cu. The potentials were controlled using staircase voltammetry with a CHI760D (CH Instruments) bipotentiostat with the Au or Cu working electrodes, a no-leak Ag/AgCl reference(Cypress Systems), and Au wire counter electrode. All potentials are reported versus the Ag/AgCl reference.

Chemometrics Methods.

As the raw data present strong potential dependent background, prior to the calculations background correction was performed using the method of Mazet *et al.*[67] The background corrected SERS spectra were arranged in the columns of data matrix **M**. Prior to the calculations, the average (or mean) spectrum of the spectra in the data set was subtracted from each of the spectra to obtain a set of "dynamic" spectra. Synchronous and asynchronous correlation spectra were then calculated from these dynamic spectra.

The mathematical procedures for the calculation of PCMW2D correlation are described in detail elsewhere.[68-69] The method provides a pair of synchronous and asynchronous spectra plotted in a 2D map between a spectral variable (here, Raman shift) axis and a perturbation (here, electrode potential) axis. The synchronous and asynchronous PCMW2D correlation spectra are proportional to spectral gradient (first perturbation derivative) and negative rate of the spectral gradient change (perturbation second derivative) along the perturbation direction, respectively. Thus a spectral intensity variation at a typical point on the plane between a spectral variable axis and a perturbation variable axis, such as potential dependent phase transitions of 2,2'-bipyridine on gold electrodes, should be visualized in the PCMW2D. Here we used synchronous PCMW2D to analyze complicated spectral variations and to choose potential range to employ 2DCOS. A window size of (2j +1 = 7) points, corresponding to 0.30 V, was used in the present study.

The 2D-COS is a data analysis technique that is well established in many fields of spectroscopy.[70] In short, the mathematical formalism of 2DCOS compares changes at every spectral variable (e.g., Raman shift) with changes at all other variables and leads to two 2D correlation maps with the variable axes; one synchronous and the other asynchronous.[70] The peaks in these plots provide evidence for change in the spectral intensities in the dataset. The changes in the spectral intensity can be caused, for example, by variations in potential, pressure or concentration of reactants which result in perturbations that affects the system. The synchronous correlation is symmetric with respect to the diagonal line and the presence of positive cross peaks indicates that intensity changes in a pair of peaks are occurring in the same direction, while the opposite is true for negative synchronous cross peaks.

The 2DCOS asynchronous spectrum is asymmetric with respect to the diagonal line and develops cross peaks only if the intensities of two spectral features change out of phase with each other (i.e., delayed or accelerated). The sequential order rules derived by Noda[71] apply at both upper and lower triangles of the 2D correlation map. Choosing the interpretation of the upper triangle of asynchronous correlation maps, a positive cross-peak indicates that the intensity change at spectral variable ν_1 (with ν_1 corresponding to y axis and, $\nu_1 > \nu_2$) occurs prior to the change of intensity at ν_2 in the sequence of spectra. However, if the sign of the corresponding synchronous intensity is negative, this rule is reversed.

The collected spectra comprise a wide range of spectral variable (Raman shift), thus it is important to investigate the correlation between different vibrational modes. The 2D correlation approach between the different spectral regions is referred as heteromode correlation and allows the investigation of the correlation of each component correlation. Heteromode 2DCOS are calculated in the same manner as standard 2DCOS correlation spectra. It is essentially the correlation result observed in the 2D correlation map away from the main diagonal. If we consider a large 2D correlation spectrum covering a relatively broad spectral region, any section of the map comparing different vibrational modes can be viewed as a hetero-mode correlation region. In hetero-mode 2D-COS analysis, the correlation spectrum is no longer symmetric with respect to the diagonal line, as data set is partitioned in two subsets of completely different vibrational modes, although the Noda's rules apply in the same manner as in conventional 2DCOS. PCMW2D and 2DCOS calculations were performed by using in-house designed software using the formalisms described by Morita and Noda, respectively.[68, 70]

Since the 2DCOS analysis of our data results in many peaks, summarizing all this information in tables can became tedious and prone to errors. In order to simplify the 2DCOS

data interpretation and comparison between Au(111) and Au(100), we employed a simplified method for sequential order determination and peaks presentation[69, 72-73] in which a multiplication was performed on the sign of each cross-peak in asynchronous and the sign of the corresponding area in synchronous spectra. Since one of the objectives of this work is to perform an effective comparison of the behavior of adsorbed 2,2'-bipyridine on both Au(111) and Au(100) by the analysis of *in situ* SHINERS spectra, the results of multiplication were presented in an upper (and lower) triangular matrix-like table. In this approach, the upper triangle of the matrix-like table represents the combination of signals from synchronous and asynchronous correlations of 2,2'-bipyridine spectra measured on Au(111) surface, with the larger spectral variable (ν_1) corresponding to the right column of spectral variable while the lower triangle corresponds to correlation results associated with 2,2'-bipyridine spectra collected on Au(100) surface, with bottom row of Raman shifts corresponding to the larger spectral variable (ν_1). If the sign is positive (+), the spectral intensity measured at the larger spectral variable (ν_1) will respond to the perturbation earlier than the spectral intensity measured at the smaller spectral variable (ν_2). If the sign is negative, the sequential order is reversed.[70]

Scanning Tunneling Microscopy Preparation

Experiments were conducted in a UHV-STM system (Omicron) which has been described before.[74] A Au(100) single crystal was cleaned by Ar^+ bombardment and annealing to 900 K. The substrate was dosed with potassium at room temperature, using a well-degassed getter source (SAES Getters). The coverage of K was estimated by comparing images of surfaces at different exposures to STM findings by Barth et al.[75] The flux at the surface is *ca.* 4 $\times 10^{13}$ atoms cm^{-2} min^{-1}. Millipore water (18.2 MΩ·cm) was used and was further purified by

performing several pump-freeze-thaw cycles. Adsorption of water was conducted by filling the chamber with water vapor to 1×10^{-8} mbar while keeping the substrate at 80 K. Using an in situ residual gas analyzer, the flux of water is estimated to be 3.7×10^{13} molecules cm^{-2} min^{-1}.

STM images were acquired in constant current mode. The Pt/Ir tips were commercially obtained (Materials and Analytical Services, Raleigh, NC). Before use, tips were either annealed to 423 K for 24 hours or bombarded with 4.5 keV electrons for 15 min. The tunneling conditions and the temperature of the substrate are indicated in figure captions. Base pressure of the chamber is 1×10^{-10} mbar. In the present study, we define one monolayer (ML) to be the density of adsorbates equal to the density of gold atoms on a (1×1) unreconstructed surfaces, i.e., 1 ML $\equiv 1.202 \times 10^{15}$ atoms or molecules cm^{-2}. Assuming that the sticking coefficients of K and water equal to one, dosing rates for K and water are *ca.* 0.033 ML min^{-1} and 0.031 ML min^{-1}, respectively.

Density Functional Theory Calculations for Au, Cu, and Cu_2O Surfaces

Density Functional Theory (DFT)[76] calculations were performed using the ab-initio total-energy and molecular dynamics program VASP 5.2 (Vienna ab-initio simulation program)[77]. A graphical user interface program, GoVASP 1.0.1 (Windiks Consulting), was used to generate the models. Au(100) surfaces were generated as a slab 2 layers thick with a 10 Å vacuum layer. The surface was extended as a 4×4×1 supercell to yield a surface with 16 Au atoms, onto which KOH molecules were brought into close contact. For the calculations, Au atoms were frozen in place. Molecular dynamic simulations were run using the micro canonical (nVE) ensemble with a 180 fs run time and 1 fs time steps. For all calculations, the generalized gradient approximation (GGA)[55-56] using the Perdew-Burke-Ernzerhof (PBE)[57] exchange-correlation

functional and projector augmented wave (PAW) potentials[78-79] were employed along with a 300 eV planewave cutoff, $1e^{-5}$ eV SCF convergence tolerance, and fast Davidson and RMM-DIIS algorithm.

Adsorption energies on Cu and Cu_2O surfaces were calculated from slabs two layers thick with a 10 Å vacuum layer. The surface was extended as a 2×2×1 supercell onto which NO_2^- and NO_3^- molecules were brought into close contact. For the calculations, atoms within the Cu and Cu_2O lattice were frozen in place. To determine adsorption energies, the energy of the minimized bare surface and the NO_x molecule is subtracted from the energy of the minimized surface/NO_x configuration.[80] For all calculations, the generalized gradient approximation (GGA)[55-56] using the Perdew-Burke-Ernzerhof (PBE)[57] exchange-correlation functional and projector augmented wave (PAW) potentials[78-79] were employed along with a 400 eV planewave cutoff, $1e^{-5}$ eV SCF convergence tolerance, and fast Davidson and RMM-DIIS algorithm.

Chapter 3. Photoelectrochemical Response of $TlVO_4$ and $TlVO_4$:$InVO_4$ Composite

Introduction

There are considerable economic, environmental, and security benefits involved in transitioning to a hydrogen based economy[1-8]. The discovery of photoelectochemical hydrogen evolution on TiO_2 by Fujishima and Honda in 1972[17] sparked intense research efforts into overall water splitting by semiconductor photocatalysis with the hope of attaining sustainable hydrogen production from solar energy. There remains considerable interest in overall water splitting today[15]. Particulate photocatalyst systems, which provide the advantages of simple cell construction and lower cost when compared to photoelectrochemical cells using massive or single crystal electrodes[4], have received significant research attention since the early reports of overall water splitting in these systems in 1980[18-20]. Since those early reports, many photocatalyst systems have been catalogued[21], though none approach commercially viable efficiency levels in visible light.

Semiconductor overall water splitting photocatalytic efficiency is limited by recombination of electron/hole pairs, fast back reactions of photocatalytic products, and insufficient visible light absorption[7]. The basic requirements of an effective total water splitting photocatalyst include strong visible absorption, stability toward photocorrosion, efficient charge transfer with limited recombination effects, low cost, and suitable band positions for water oxidation/reduction accompanied with low overpotentials[16]. The positions of the conduction and valence band edges of the semiconductor are particularly crucial to the photocatalytic activity. The conduction band must lie at potentials more negative than H^+/H_2 (0 V vs. NHE at pH=0) and

the valence band must lie at potentials more positive than O_2/H_2O (1.23 V vs. NHE at pH=0)[81]. Without these conditions being met, total water splitting cannot occur thermodynamically and must be driven by an external bias.

While a number of semiconductor materials are relatively efficient at hydrogen production, this efficiency often comes at a cost of diminished stability in the aggressive aqueous environment, particularly in the case of metal chalcogenides[4, 21, 23]. Metal oxides are generally stable enough to resist photocorrosion if the kinetics of water oxidation are faster than anodic decomposition, and have thus been the focus of many researchers as viable water splitting photocatalyst materials[16]. The primary drawback of metal oxide systems are typically large bandgaps (low visible absorption) or conduction bands too low in energy for hydrogen evolution.

In an attempt to address this shortcoming, significant research efforts have been directed to dye sensitization of metal oxide materials to improve visible light absorption and overall activity[82-84]. In addition, doping metal oxides with metal cations, carbon, sulfur, and nitrogen has been explored as a way to increase visible absorption[85-89]. Attempts have also been made to incorporate metal oxides into heterostructures to improve optical absorption and charge separation characteristics. Recent reports on the $BiVO_4$:Co_3O_4 system indicate enhanced photocatalytic activity and photoinduced charge separation when compared to the materials individually[49, 90]. Studies on the ZrO_2:TiO_2 system also indicate that the interface between the two types of particle leads to diminished recombination[91].

One promising class of materials for semiconductor photoelectrochemical purposes are the vanadates. In particular, a number of reports suggest that $InVO_4$ and $BiVO_4$ might be good candidate materials for photocatalysis[81, 92-97]. However, the vanadates as a class are relatively

unexplored especially when compared to well-known materials such as TiO_2 or ZnO. Given the success of these materials, we wondered whether incorporating $InVO_4$ into a heterostructure might provide synergies leading to enhanced activity. Given theoretical discussion about how cation exchange might affect the VO_4^{3-} band gap[24], we also wondered whether using a cation like Tl might change the photoelelectrochemical properties relative to In.

Utilizing this strategy, we report here the synthesis of $InVO_4$, $TlVO_4$, and an $InVO_4$:$TlVO_4$ composite by facile aqueous solution methods for the purpose of improving charge separation and the photoelectrochemical characteristics of the system. $InVO_4$ has two stable phases, monoclinic (Cm/2) and orthorhombic (Cmcm). Our work makes use of orthorhombic form of $InVO_4$[98]. Both $InVO_4$ and $TlVO_4$ share the orthorhombic Cmcm (63) crystal structure, which is comprised of edge sharing $(In/Tl)O_6$ octahedra with VO_4 tetrahedral linkers. In and Tl have nearly identical atomic radii (1.93 Å and 1.96 Å, respectively[99]), which naturally leads to similar lattice dimensions and volumes for $InVO_4$[53] and $TlVO_4$[54] (325$Å^3$ vs. 345 $Å^3$, respectively). The similarity of crystal structure and dimension allows for $InVO_4$ to seed $TlVO_4$ growth, thereby providing an avenue for effective composite formation. These composites provide an opportunity to tune the band positions and study how these changes affect photoelectrochemical activity.

Results and Discussion

$InVO_4$ is typically synthesized by solid state method involving the reaction of In_2O_3 and V_2O_5 at high temperature[94, 100]. Sample particles made by this method tend to be large and have a correspondingly low surface area. Also reported are wet chemical precipitation methods followed by subsequent calcination at around 600°C[101-102]. The synthetic method reported here

differs from previous approaches to making $InVO_4$. The reflux conditions of the aqueous environment at pH=4 induces crystallization of nanoparticulate orthorhombic $InVO_4$ that is ordinarily accessed at temperatures above 680°C[101]. These same conditions also lead to crystallization of orthorhombic $TlVO_4$.

Figure 3.1 shows powder X-ray diffraction data of $InVO_4$, $TlVO_4$, and $InVO_4$:$TlVO_4$ composite. The $InVO_4$ diffractogram features broad, low intensity peaks indexed to orthorhombic $InVO_4$ (JCPDS no. 04-008-7237)[53]. The peak broadening apparent in the diffractogram arises as a consequence of the small $InVO_4$ crystallite size (vide infra).

The $TlVO_4$ diffractogram contains sharp, intense peaks which match orthorhombic $TlVO_4$ (JCPDS no. 35-0086)[54] well. Minor deviations in diffractogram intensities in the low angle region between that reported here and that reported by Touboul and Ingrain[54] are likely caused by different preferred orientations or preparation methods between the crystals studied[103]. The diffractogram for the $InVO_4$:$TlVO_4$ composite matches that of $TlVO_4$, but with contributions from $InVO_4$ apparent as shoulders or broadened peaks; $InVO_4$ peaks appear roughly 0.5° higher in 2θ than $TlVO_4$ peaks. This observation indicates that both $InVO_4$ and $TlVO_4$ were synthesized and are present in the composite sample.

Figure 3.2 shows TEM micrographs of $InVO_4$, $TlVO_4$, and the $InVO_4$:$TlVO_4$ composite. Images A and B contain $InVO_4$ nanoparticles ranging from 10 nm to 30 nm in diameter and agglomerated into large clusters of discernable particles. The small size of these particles is consistent with the diffractogram peak broadening discussed above. Images C and D display $TlVO_4$ particles which range from 1 μm to 5 μm in diameter. $TlVO_4$ particles do not agglomerate and appear smooth with few surface defects. $TlVO_4$ generally melts under focused,

high energy e^- beam while $InVO_4$ particles are robust and able to dissipate the injected charge. Previous studies have indicated that $TlVO_4$ is susceptible to decomposition above 300°C[54, 104], which explains the e^- beam sensitivity of this system.

Image E contains a TEM image of $InVO_4$:$TlVO_4$ composite nanoparticles between 20 nm and 40 nm in diameter with significant agglomeration into clusters. These clusters are altered in shape by the e^- beam, though not as strongly as is $TlVO_4$, which causes individual particles to fuse into larger masses. Image F displays a small cluster of composite material collected by STEM. The particles in images E and F show no evidence of a core-shell boundary or any other type of distinct heterostructure visible by TEM.

Figure 3.3 displays the EDS spectrum of $InVO_4$:$TlVO_4$ composite taken in STEM mode. The EDS spectrum of the composite was collected to determine whether $TlVO_4$ was successfully deposited onto the surface of $InVO_4$ nanoparticles. EDS spectroscopy indicates the presence of Tl, In, and V in the $InVO_4$:$TlVO_4$ composite sample. Measurements performed on agglomerated regions as well as individual particles and small clusters revealed comparable ratios of indium and thallium throughout the sample, which excludes the possibility of separate domains of $TlVO_4$ and $InVO_4$. The presence of oxygen prevents accurate quantitative analysis of sample composition because of selective low energy X-ray absorbance by the beryllium window of the EDS detector[105]. Extraneous peaks of copper originate from the supporting grid. Thus, XRD confirms the presence of orthorhombic $InVO_4$ and $TlVO_4$, indicating that both crystal systems have been incorporated into the composite material. The lack of definable structure between the two materials in TEM images is likely the result of nearly identical crystal structures, allowing growth of $TlVO_4$ to take place on the $InVO_4$ crystals without significant strain being introduced.

Figure 3.4 shows cyclic voltammagrams of $InVO_4$, $TlVO_4$, and $InVO_4$:$TlVO_4$ composite under no illumination, full xenon arc lamp illumination, and xenon arc lamp illumination with a 400nm cutoff filter. Photocurrent density measurements were compiled at -0.5 V, 0 V, and 1 V in Table 3.1. Samples show anodic photocurrent with onset of 0.25 V for $InVO_4$ and roughly 0.35 V for both $TlVO_4$ and the composite material. $TlVO_4$ shows roughly a tenfold increase in anodic photocurrent over $InVO_4$ while the composite shows a twofold increase. Illumination also increases cathodic photocurrent in each sample, with significant photocurrent increases and potential onsets of 0.3 V for $InVO_4$ and 0.4 V for $TlVO_4$ and the composite. Again, both the $TlVO_4$ and the composite show more than a tenfold increase in cathodic photocurrent over $InVO_4$.

There exist several possible explanations for the larger photocurrent density exhibited by $TlVO_4$ and $InVO_4$:$TlVO_4$ composite. Ordinarily, one would expect a sample with larger electrochemical surface area (smaller particles) to display more photoelectrochemical activity; however, the response of our samples is counter to the results that may be expected based on particle size considerations alone. The $TlVO_4$ particles are at least an order of magnitude larger than $InVO_4$ and should correspondingly have a smaller surface area and thus lower electrochemical activity, but $TlVO_4$ exhibits a greater photoelectrochemical response. Disparate film thicknesses could also account for different photoelectrochemical, however, we controlled the film thickness of all samples studied to roughly 10 μm. These observations strongly suggest that the differences in photoelectrochemical activity relate to differences in materials chemistry.

Typically, for an n-type semiconductor, no cathodic photocurrent is observed as photocurrent is the result of minority carrier generation and subsequent oxidation of solution species. However, previous research has noted the occurrence of an anomalous photoeffect

(APE) in semiconductors arising from surface states within the energy bandgap, which could be the origin of anomalous cathodic photocurrent in $InVO_4$, $TlVO_4$, and the composite[106-107]. In each sample, the I-V curve has a general tilt indicative of redox processes on the surface, particularly as vanadium oxoanions are progressively oxidized or reduced.

Figure 3.4 shows that both the $TlVO_4$ and $InVO_4$:$TlVO_4$ composite contain a reversible redox couple near -0.8 V which is attributable to the Tl^0/Tl^+ couple (E_0= -0.336 V+ 0.0591*log[Tl^+] V). Studies on $TlVO_3$, which contains Tl^+, also indicate the same type of reversible redox peaks. Tl^{3+} is reduced to Tl^+ according to the Tl^+/Tl^{3+} redox couple at E_0=1.252 V, resulting in Tl^+ at the surface that is reduced to Tl[108]. However, the photoactivity of $TlVO_4$ and $InVO_4$:$TlVO_4$ composite is the same if the potential is reversed prior to accessing the Tl^+/Tl^0 couple.

Figure 3.5 shows Mott-Schottky plots constructed from capacitance measurements collected by AC voltammetry. This data was transformed to $1/C^2$ in order to fit the Mott-Schottky equation $\frac{1}{C_{sc}^2} = \left[\frac{2}{e\varepsilon\varepsilon_0 N_D}\right]\left[E - E_{fb} - \frac{kT}{e}\right]$ where C_{sc} is the space charge capacitance, e is the electron charge, k is the Boltzmann constant, T is temperature in Kelvin, ε_0 is the permittivity of free space, ε is the dielectric constant of the film electrode, N_D is the carrier density, and E and E_{fb} are the applied and flatband potentials, respectively[109-110]. When plotted, $1/C^2$ vs. E is linear in the depletion region of the semiconductor and allows estimation of flat-band potential, E_{fb}, at the intersection of the potential axis ($1/C^2$=0)[111]. The flat-band potential provides a good estimation of the conduction band edge in n-type semiconductors[112]. The band edge generally lies between 0.1 eV and 0.4 eV more negative depending upon conductivity of the semiconductor[113]. As compiled in Table 3.2, estimated flat band potentials are -0.041 V, -

0.221 V, and -0.217 V vs. Ag/AgCl for $InVO_4$, $TlVO_4$, and the $InVO_4$:$TlVO_4$ composite, respectively. These flat-band potentials give some insight into the photoactivity of the materials with water. Samples containing Tl appear to have a conduction band edge more negative than that of $InVO_4$, possibly allowing for better water reduction activity. None of the materials studied, however, has band positions ideal for photocatalytic water splitting without application of an electrochemical bias ($E°[H^+/H_2]$ = -0.236 V vs. NHE at pH=4, -0.458 V vs. Ag/AgCl)[114].

We recognize that our estimation of the conduction band level is at odds with reported observation of H_2 production from $InVO_4$ and $InVO_4$ loaded with Ni/NiO. Our own experience suggests that little or no H_2 is produced from samples of $InVO_4$. Additionally, there exist several potential experimental complications that could render a higher level of uncertainty into the results. Even in the case where the conduction band level of $InVO_4$ is around 0.4 eV more negative than the flatband potential, there will be little or no overpotential to perform the water reduction reaction, which leads to minimal H_2 production from H_2.

Figure 3.6 contains diffuse reflectance UV-vis spectra of $TlVO_4$, $InVO_4$, and $InVO_4$:$TlVO_4$ composite samples. Band gaps for samples are estimated by extrapolation of the linear portion of the absorption edge. Bandgaps for $InVO_4$, $TlVO_4$, and $InVO_4$:$TlVO_4$ are estimated as 3.50 eV (354 nm), 2.98 eV (422 nm), and 2.94 eV (415 nm), respectively. The presence of thallium in $TlVO_4$ and the composite serves to reduce the bandgap of these vanadates relative to $InVO_4$.

Figure 3.6 also reveals the presence of absorption in the visible wavelengths for each sample extending to approximately 600 nm (2.07 eV) for $InVO_4$ and the composite and roughly 800 nm (1.55 eV) for $TlVO_4$. Previous reports of the band gap of $InVO_4$ by diffuse reflectance

UV-visible spectroscopy have typically estimated it as 1.9-2.0 eV[93-94, 115-116]. The $InVO_4$ bandgap presented here significantly deviates from those of previous reports. Interestingly, we performed photoluminescence measurements on the $InVO_4$ material (not shown). These measurements revealed the presence of a luminescence peak at 550 nm with 325 nm excitation, but no luminescence was observed with 442 nm excitation. These results suggest that the $InVO_4$ band gap is at energies greater than 442 nm (or 2.8 eV).

In order to better understand these observations, DFT calculations were performed to elucidate the band structure. Figure 3.7 presents the partial density of states of the materials as calculated using CASTEP code within Materials Studio 4.4. 0 eV signifies the highest occupied state of the semiconductor, corresponding to the top of the valence band. The calculated bandgap of $InVO_4$, $TlVO_4$, and the $InVO_4$:$TlVO_4$ composite is 3.14 eV, 1.92 eV, and 2.25 eV, respectively. The bandgap for $InVO_4$ correlates well with the 3.1 eV predicted by Oshikiri et. al. in previous studies[95, 117], though is larger than the 2.3 eV calculated by Zhang and coworkers[115]. Results from these calculations match well with UV-vis observations and are consistent with bandgap underestimation typical of DFT calculations[24, 118-120].

The origin of the visible absorbance for $InVO_4$, $TlVO_4$, and the composite likely arise from oxygen vacancies and gap states lying above the valence band. These states lie closer to the conduction band and give rise to false band edges, albeit with significant absorption, that are lower in energy than the true bandgap. Similar observations are seen with $InTaO_4$, for which it has been determined that the apparent optical bandgap of 2.6 eV[121] actually arises from oxygen vacancy levels within the bandgap[120, 122] while the true optical bandgap is 4.3 eV[120]. A valence band to conduction band transition of 3.50 eV for $InVO_4$, as measured by diffuse reflectance UV-vis spectroscopy, is not surprising as calculations have predicted $InVO_4$ to have a smaller

bandgap relative to $InTaO_4$ (3.1 eV vs. 3.7 eV) because V 3d orbitals lie at lower energy, likely because of higher electronegativity and different crystal geometry[95]. $TlVO_4$, however, has lower energy band edge absorption at 2.94 eV with significant deviation from the predicted 1.92 eV bandgap. One reason this underestimation is so large could be the presence of a conduction band with more s orbital character, which has previously been shown to give rise to band gap determination errors exceeding 2 eV in DFT calculations.[123-125]. While the inaccuracies associated with uncorrected DFT bandgap calculations may be large, the DFT calculations still provide a point of comparison. The systems we study are similar enough in nature that the inaccuracies resulting from discontinuity in the exchange correlation functional and other correlation effects should be similar and allow evaluation of relative band positions and composition.

Our DFT calculations indicate that the primary contribution to the valence band of each compound comes from O 2p orbitals with small contributions from V 3d, In 5s, and/or Tl 6s and 6p. The valence bands of both $InVO_4$ and $TlVO_4$ would ordinarily be expected to occur at nearly the same level because of the dominant contribution of O 2p orbitals and the small energy difference between In and Tl. Estimation of the valence bands by the Mott-Schottky method coupled with UV-visible measurements, however, indicates the valence band tops of $TlVO_4$ and the composite lies nearly 0.7 eV more negative than that of $InVO_4$. A schematic representation of the proposed band structures of these compounds based upon Mott-Schottky flat-band potentials and UV-visible bandgap approximations is presented in Figure 3.8. Calculations performed by Walsh et. al. on $BiVO_4$ show that Bi 6s interaction with O 2p causes an upward dispersion in the maximum energy of the valence band of 0.4 eV[123]. The presence of Tl 6s and 6p orbitals and their coupling with O 2p orbitals in $TlVO_4$ and the composite thus could be the

cause of the higher valence band edges. Coupling between Tl 6s and O 2p in the valence band is qualitatively apparent as delocalization of the density of states when compared to that of $InVO_4$ where sharper, more localized states exist.

The conduction bands of both $TlVO_4$ and $InVO_4$ are primarily composed of V 3d orbitals with additional contribution from O 2p, In 5s, and/or Tl 6s, matching previous observations[115]. The contribution of Tl 6s orbitals, in contrast to In 5s orbitals, provides a more hybridized conduction band in $TlVO_4$ which again appears to slightly raise the conduction band bottom relative to that of $InVO_4$.

The diffuse nature of the Tl 6s orbitals incorporated into the conduction band and valence bandof $TlVO_4$ allows better contact and interaction with solution species. The Gerischer model of semiconductor-electrolyte interfaces suggests that the rate of reaction is dependent upon the overlap of the density of states of the semiconductor valence band and conduction band with the reactants[111, 126]. The more diffuse s orbitals incorporated into the conduction band of $TlVO_4$ would thus exhibit improved contact with the electrolyte and could result in greater photocurrent. Indeed, this is what is seen in Figure 3.4 for the Tl-containing species; s orbitals are available at the bottom of the conduction band to accept photogenerated electrons in order to reduce water when sufficiently negative potentials are reached. This effect is most likely enhanced by increased absorption into the visible region of the spectrum because of the lower energy bandgap of the $TlVO_4$. An alternative explanation for the different photocurrent densities of the materials could be differences in the photoelectrochemical surface area available because of different particle size and shape. The evidence contradicts this assumption, however, because more

photocurrent occurs for lower surface area $TlVO_4$ than either $InVO_4$ or $InVO_4$:$TlVO_4$ composite as discussed above.

The $InVO_4$:$TlVO_4$ composite material is dominated by $TlVO_4$ characteristics despite the fact that both $InVO_4$ and $TlVO_4$ are incorporated into the composite as inferred by XRD, TEM, and EDS. UV-vis shows the composite shares similar band edge absorptions with $TlVO_4$ with some small contribution from $InVO_4$. Photoelectrochemistry shows nearly identical flat band potentials and similar photoactivity; this result is not surprising since the synthetic method utilized deposits $TlVO_4$ onto the surface of $InVO_4$, thereby yielding surfaces of similar chemistry for $TlVO_4$ and the composite. The calculations also reinforce the dominant effect of Tl in the composite by yielding a similar band structure and density of states to that of $TlVO_4$.

Conclusion

In summary, we report a simple solution method to synthesize $InVO_4$, $TlVO_4$, and an $InVO_4$:$TlVO_4$ composite. Photoelectrochemical activity and the band structure of $TlVO_4$ has been characterized for the first time and compared to the better characterized $InVO_4$. We conclude from these results that the higher photoelectrochemical activity of $TlVO_4$ and the $InVO_4$:$TlVO_4$ composite arise from the more diffuse Tl 6s character of the valence and conduction bands relative to In; this enables better contact with electrolyte allowing photogenerated electrons and holes to more readily react with solution species, which decreases the likelihood of charge recombination. The results reported here provide the first evaluation of $TlVO_4$ as a photocatalyst and evidence that incorporating crystallographically similar metal oxides into a composite heterojunction can alter the band positions and bandgap, providing an opportunity for concerted band engineering and tuning. Figure 3.8 graphically presents this band

tuning and gives better approximations of the valence and conduction band positions than those previously published.

Acknowledgements

TEM, STEM, XRD, and diffuse reflectance UV-visible spectroscopy was carried out in part in the Frederick Seitz Materials Research Laboratory Central Facilities, University of Illinois, which are partially supported by the U.S. Department of Energy under grants DE-FG02-07ER46453 and DE-FG02-07ER46471. This work was supported by the National Science Foundation.

Tables

Table 3.1: Photocurrent at 1 V, 0 V, and -0.5 V.

Photocurrent Density ($\mu A/cm^2$)			
	$InVO_4$	$TlVO_4$	$InVO_4$:$TlVO_4$
1V	5.56	63.30	11.91
0V	-5.37	-180.38	-108.31
-0.5V	-8.19	-105.86	-245.61

Table 3.2: Flat-band potentials determined from Mott-Schottky method.

	Flat Band Potential (V) vs. Ag/AgCl		
Frequency	$InVO_4$	$TlVO_4$	$InVO_4$:$TlVO_4$ composite
1000 Hz	N/A	-0.280	-0.253
500 Hz	-0.038	-0.189	-0.186
100 Hz	-0.023	-0.182	-0.200
50 Hz	-0.063	-0.231	-0.228
Average	**-0.041**	**-0.221**	**-0.217**

Table 3.3: Comparison of calculated and experimental band gaps.

	Calculated band gap (eV)	Experimental band gap (eV)
$InVO_4$	3.14	3.50
$TlVO_4$	1.92	2.94
$InVO_4$:$TlVO_4$ composite	2.25	2.98

Figures

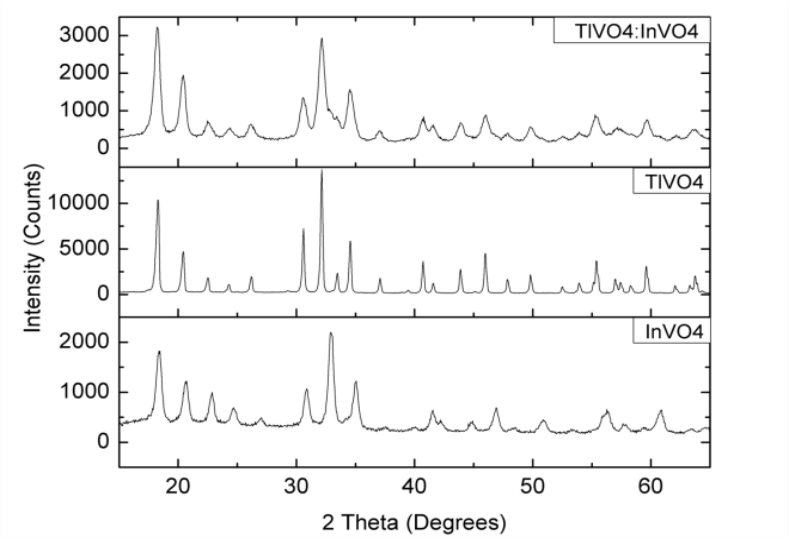

Figure 3.1: X-ray diffractograms of $InVO_4$:$TlVO_4$ composite, $TlVO_4$, and $InVO_4$.

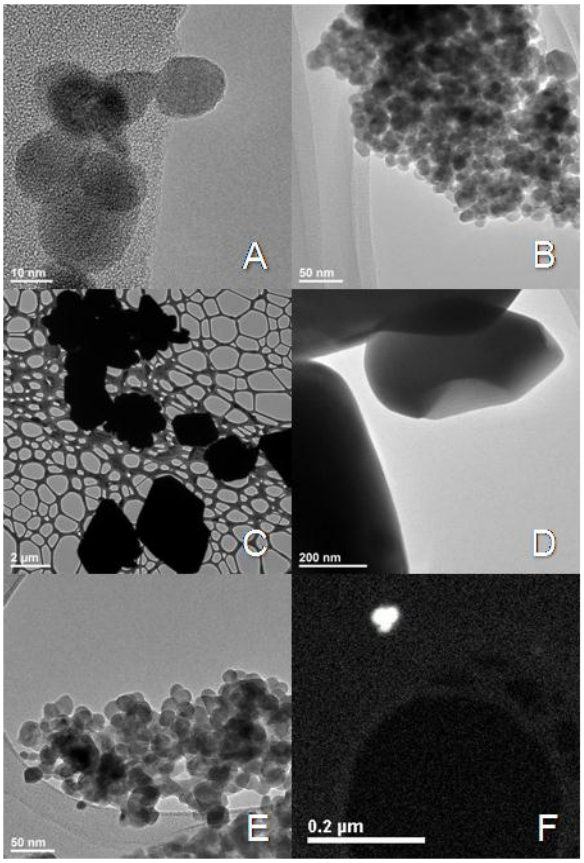

Figure 3.2: TEM images of (A, B) $InVO_4$, (C, D) $TlVO_4$, and (E) $InVO_4$:$TlVO_4$ composite, and (F) a STEM image of the $InVO_4$:$TlVO_4$ composite.

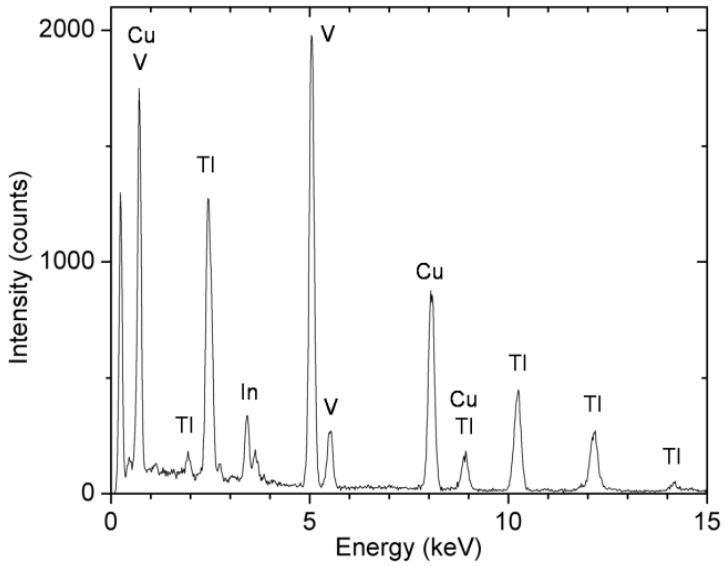

Figure 3.3: EDS spectrum of $InVO_4$:$TlVO_4$ composite.

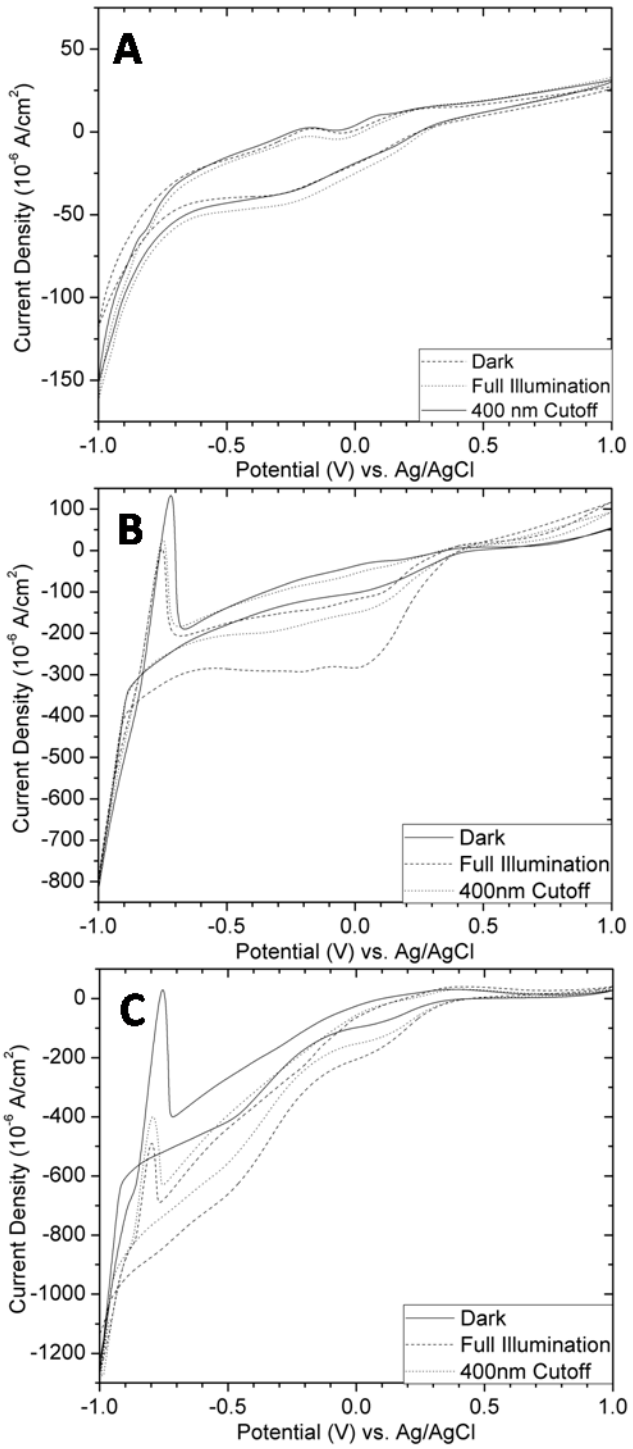

Figure 3.4: Cyclic voltammetry of (A) $InVO_4$, (B) $TlVO_4$, (C) $InVO_4$:$TlVO_4$ composite performed at pH=4 in 0.1 M $K_2SO_{4(aq)}$.

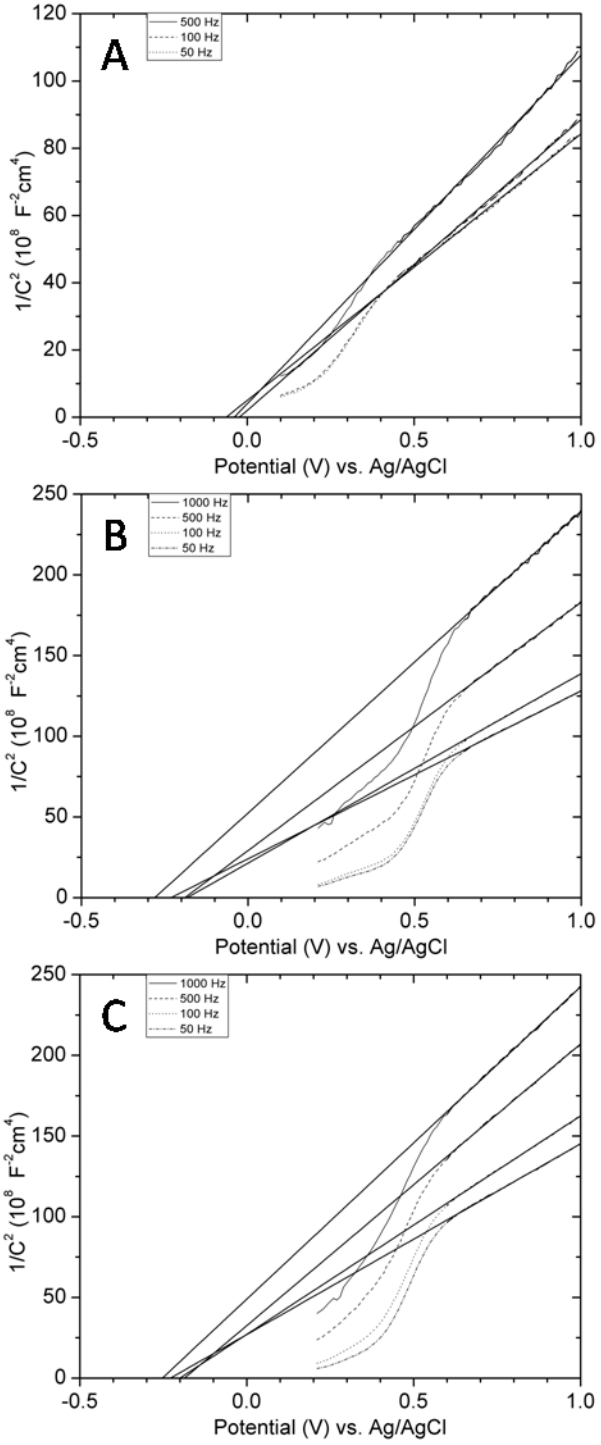

Figure 3.5: Mott-Schottky plots of (A) $InVO_4$, (B) $TlVO_4$, and (C) $InVO_4$:$TlVO_4$ composite performed in pH=4 0.1M $K_2SO_{4(aq)}$.

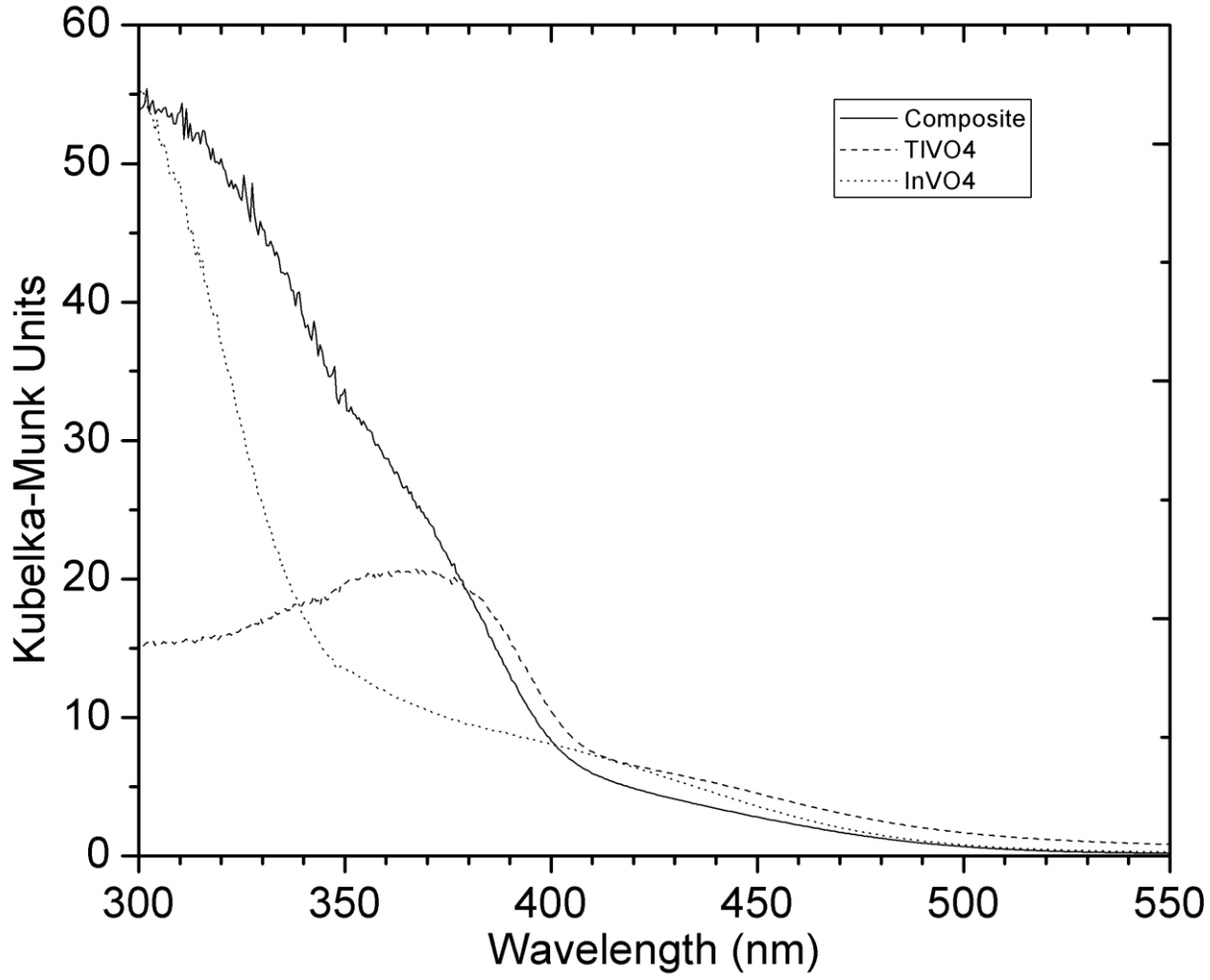

Figure 3.6: UV-visible diffuse reflectance spectra of $TlVO_4$, $InVO_4$, and $InVO_4$:$TlVO_4$ composite

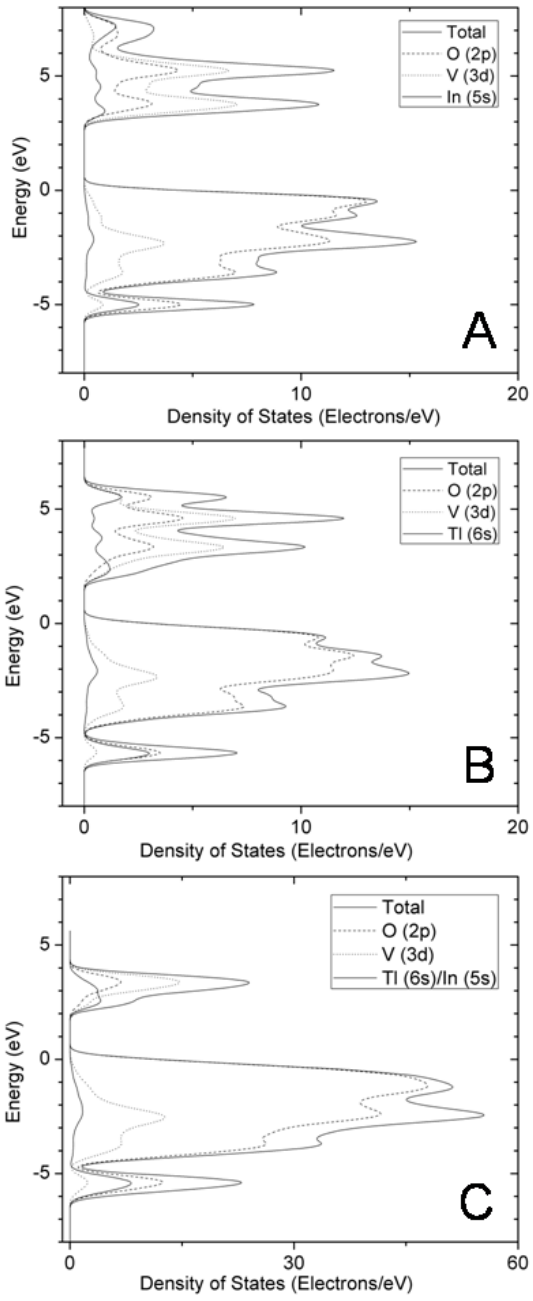

Figure 3.7: Partial density of states (PDOS) of (A) $InVO_4$, (B) $TlVO_4$, and (C) $InVO_4$:$TlVO_4$ composite. (PDOS labeled by primary contribution to s, p, and d orbitals)

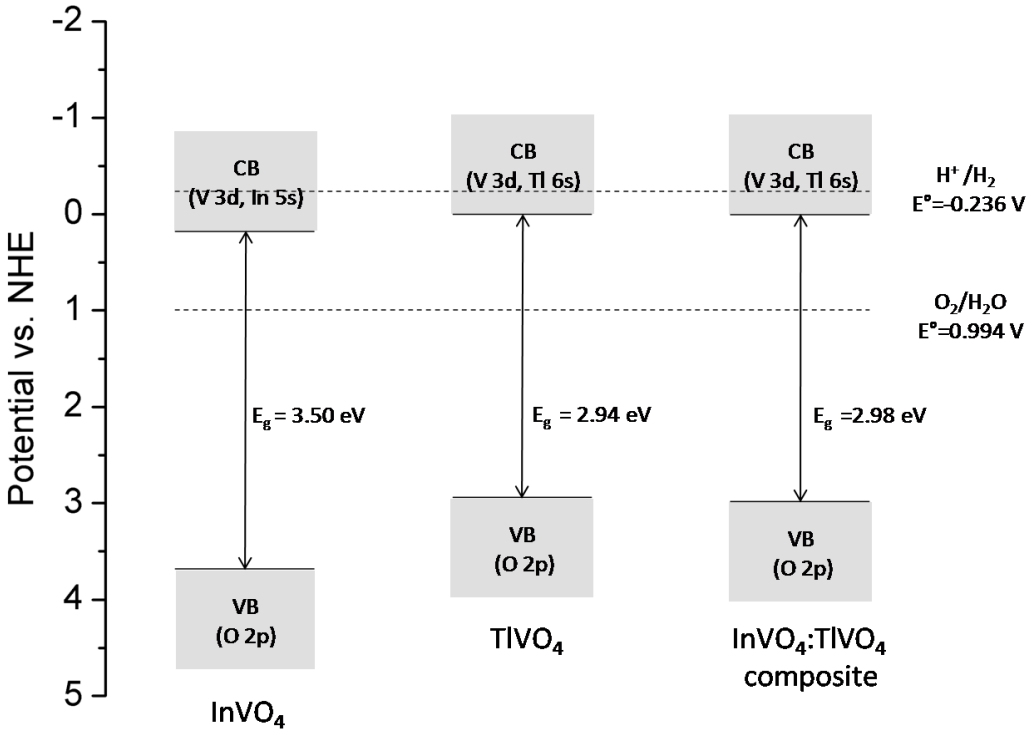

Figure 3.8: Representation of the band structures of $InVO_4$, $TlVO_4$, and $InVO_4$:$TlVO_4$ composite at pH 4.

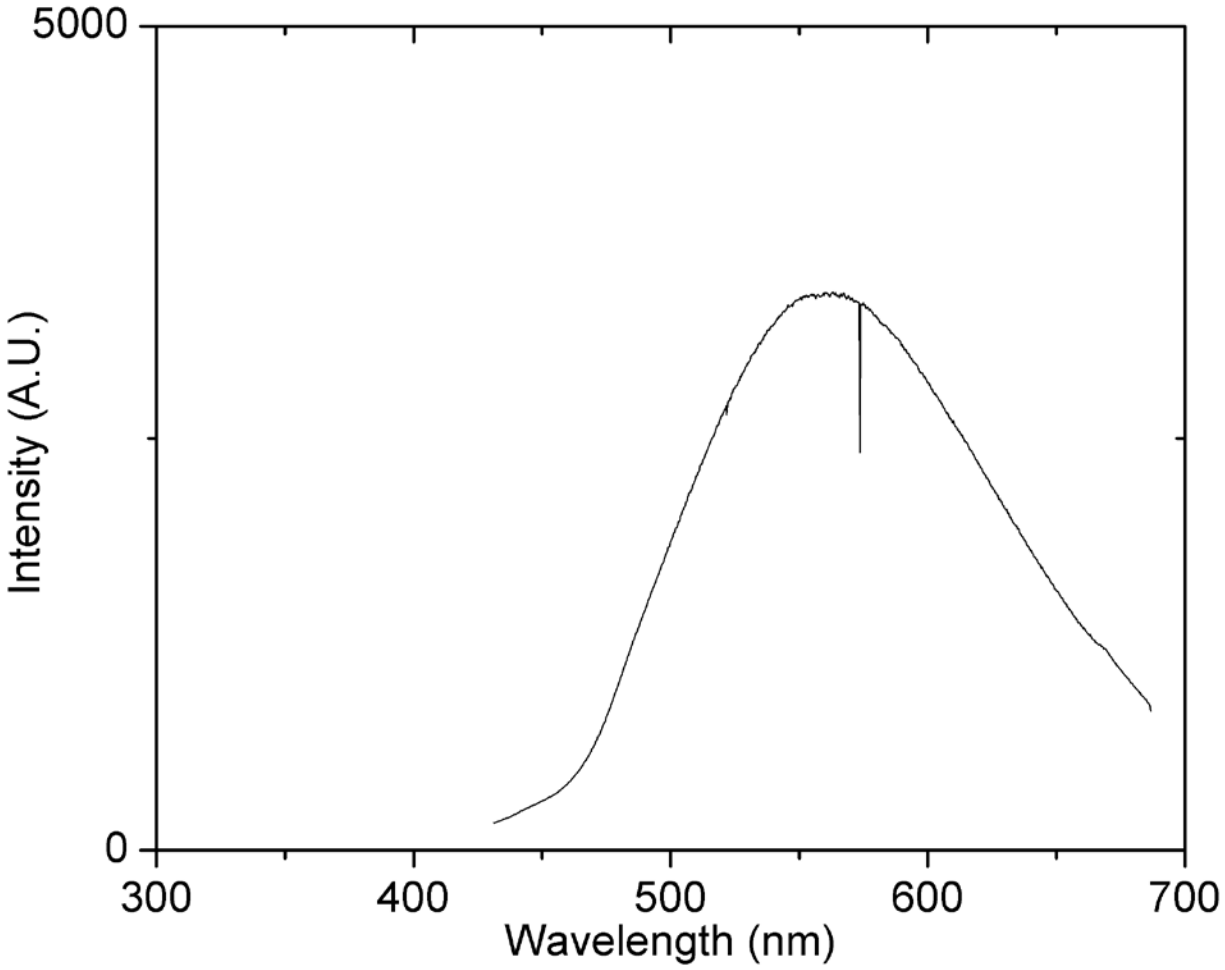

Figure 3.9: Photoluminescence of InVO4 at an excitation wavelength of 325 nm.

Chapter 4. Face Dependent Shell Isolated Nanoparticle Enhanced Raman Spectroscopy (SHINERS) of 2,2'-bipyridine on Au(100) and Au(111)

Reproduced with permission from Butcher, D. P.; Boulos, S. P.; Murphy, C. J.; Ambrosio, R. C.; Gewirth, A. A., J. Phys. Chem. C ***2012,*** *116, 5128.* *Stefano P. Boulos conducted synthesis of SiO_2 coated Au nanoparticles. Renato Canha Ambrosio performed Perturbation Correlation Moving Window 2-Dimensional (PCMW2D) and 2-Dimensional Correlation Spectroscopy (2D-COS) data transformations. He also contributed to the analysis of 2-Dimensional plots.*

Introduction

Surface-enhanced Raman scattering (SERS) provides an avenue for non-destructive detection of surface analytes down to the single molecule level.[127-130] The effectiveness of SERS is mostly limited to electrochemically roughened surfaces and nanoparticles of coinage metals (Ag, Au, Cu). Thus, the technique is not broadly applicable to other metals or to single crystal surfaces. Attempts have been made to expand SERS to other transition metals[131-132] and to generic surfaces using tip-enhanced Raman spectroscopy (TERS).[133-134] These techniques, however, experience many of the same drawbacks of SERS including low detection sensitivity and the inability to effectively study adsorbed species on single crystal electrodes because of signal interference from analyte adsorbing to the Raman probe.

To address some of these issues, Li, et al.[43-46] developed a new technique, shell-isolated nanoparticle-enhanced Raman spectroscopy (SHINERS), consisting of a gold nanoparticle Raman probe that is chemically isolated from the analyte by an insulating thin SiO_2 shell. This arrangement allows for the long-range electromagnetic (EM) enhancement to provide Raman signal while excluding any interfering signal from molecules adsorbing to the particles. Enhancement is strongest at the interface between the particle and surface, providing an effective probe for surface adsorbed analyte, as diagramed by Li, et al.[45] This unlocks a wide range of surfaces and solid/liquid systems for investigation by SHINERS.

The adsorption dynamics of 2,2'-bipyridine on Au single crystals have been studied extensively. Several transitions are anticipated upon potential scanning since differential capacity measurements performed by Lipkowski, et. al., show the presence of at least five capacity maxima associated with 2,2'-bipyridine on Au(111), starting on the anodic scan at ca. -600 mV and continuing to +200 mV vs. SCE.[135-136] Further, STM investigations by Noda, et al.[137] as well as Dretschow and Wandlowski[61, 138-139] indicate several transitions of 2,2'-bipyridine films on Au as the potential is scanned. Specifically, as potential increases, the 2,2'-bipyridine film becomes more ordered in N-bonded vertical orientations, while at more negative potential, the film is more disordered. Brolo, et al.[60] examined 2,2'-bipyridine adsorption on quasi Au(111) and determined that the molecules are cis N-bound at positive potentials, with indications of cisoid N-bound configurations at negative potentials. In these studies, the Au(111) surface was activated to produce SERS, and thus it cannot be excluded that signal originates from areas of local roughness, calling into question the full assignment of 2,2'-bipyridine adsorption on Au(111). Of particular interest is the nature of adsorption at negative potentials, since previous studies of pyridine and 2,2'-bipyridine on Au using IR are limited by selection rules that only allow in plane vibrations to be seen, which prevents observation of π-flat oriented molecules since the molecular dipole is not affected by electrode polarization.[135, 137, 140] Various reports have suggested that 2,2'-bipyridine below -500 mV vs. Ag/AgCl adsorbs in π-flat cis or trans configurations, as well as in N-bound cisoid orientations.[60, 136, 141]

In order to address these issues, we present here SHINERS spectra to learn more about the adsorption dynamics of 2,2'-bipyridine to Au single crystals with broader applicability to other solid/liquid interfaces.

By means of visual inspection, it is hard to pinpoint the spectral pattern differences of 2,2'-bipyridine in the complicated and sensitive regions of ring breathing modes (990 cm^{-1} to 1040 cm^{-1}) and C-C inter-ring modes (1290 cm^{-1} to 1340 cm^{-1}) between different surfaces upon potential cycling. Perturbation Correlation Moving Window Two Dimensional Spectroscopy (PCMW2D) is used to display the rate of spectral variation upon perturbation by an external variable[68-69, 72-73, 142]; in our case, correlation is plotted along the Raman shift and potential axes in order identify the vibrational transitions as potential is scanned. Two Dimensional Correlation Spectroscopy (2DCOS) is then used investigate interesting regions of spectral transition to provide information regarding the synchronization of peaks and the sequence of spectral variation.[70-73, 137, 143-146] These factors are used to investigate the delicate differences between 2,2'-bipyridine adsorption on the Au(111) and Au(100).

Results

Our analysis will be centered in two spectral regions: ring breathing modes, from ~990 cm^{-1} to 1040 cm^{-1}, and C – C interring stretching modes, from ~1290 cm^{-1} to 1340 cm^{-1}. These regions are more sensitive to potential perturbation because the vibrations exhibit significant frequency shifts dependent upon molecular orientation. Utilizing the high resolution provided by SHINERS will provide insight into the adsorption dynamics of 2,2'-bipyridine on Au(111) and Au(100) that has previously eluded researchers.

Conventional Spectral Analysis

Figure 4.1 shows an overlay of the 2,2'-bipyridine spectrum on Au(100) obtained at potentials between -800 mV and +1000 mV vs. Ag/AgCl. The spectrum contains some 23 peaks between 450 cm^{-1} and 1650 cm^{-1} at -600 mV, the potential at which the highest Raman

intensities are observed, which are denoted by labels **A-W**. Additional peaks at positive potentials are observed near in the region 1016 cm^{-1} to 1019 cm^{-1} and 1306 cm^{-1} to 1310 cm^{-1} and are labeled **Y** and **Z**, respectively. Detailed spectral analysis (vide infra) also reveals occluded peaks at 996 cm^{-1} (**X**), 1030 cm^{-1} (**β**), and 1317 cm^{-1} (**α**). These spectra feature peaks that are similar to those reported previously on Au, Cu, and Ag surfaces and colloids and display high signal to noise.[60, 147-151] Spectral regions characteristic for adsorbed 2,2'-bipyridine are identified and used to diagnose molecular orientation on the surface. In the region between 990 cm^{-1} and 1040 cm^{-1}, peaks **I-L**, **X**, **Y**, and **β** are ascribed to ring breathing modes of 2,2'-bipyridine. The very intense peaks between 1290 and 1340 cm^{-1} (peaks **Q**, **Z**, **α** and **R)** correspond to C – C inter-ring stretching modes.[60] Table 4.1 provides assignments of these and the other labeled peaks based upon the literature along with comparison to the known vibrations for solid 2,2'-bipyridine, aqueous 2,2'-bipyridine, and $Zn(bpy)_2Cl_2$.[60, 147, 149-150, 152-153]

In order to more fully represent the potential dependent spectra, Figure 4.2 shows the 3D representation of SHINERS background corrected spectra of 2,2'-bipyridine collected on Au(111) and Au(100) during anodic and cathodic polarization between -0.8 V and 1.0 V *vs*. Ag/AgCl. The spectra show little intensity at 1.0 V as a result of desorption from the oxidized surface, but intensity increases as the potential becomes more negative. It is interesting to note that on both electrodes, the intensities measured in the cathodic sweep are higher than the corresponding intensities measured during the anodic sweep. This hysteresis has also been observed by Brolo, et al.[60], Noda, et al.[137], and Kamyshny, et. al.[150] while studying 2,2'-bipyridine adsorption on Au(111) and colloidal Ag, respectively. Additionally, non-linear relationships between SERS intensity and adsorbate coverage have been observed in similar systems, resulting in decreasing SERS intensity with increasing surface adsorbate

concentration.[154-156] Spectral intensities are also larger for 2,2'-bipyridine on Au(100) than on Au(111). This is consistent with the VASP calculations by Li, et. al.[45] that pyridine interacts more strongly with Au(100) than Au(111). Li and coworkers also found that different dielectric constants for the different surfaces contribute to facet-dependent SHINERS intensity by making the surface film more polarizable, leading to greater EM enhancement intensity upon adsorption.[45] Our observations are in line with these results.

Since SERS is sensitive to conformation and the local environment of molecules arranged at the electrode surface, it is important to follow the correlations of all vibrational modes along the potential direction in order to further characterize the 2,2'-bipyridine film phase transition on both electrodes. This analysis will be performed with PCMW2D and 2DCOS.

Perturbation-Correlation Moving-Window Two-Dimensional Correlation Analysis

Figure 4.3A shows the synchronous PCMW2D plots in the ring breathing mode region constructed from the potential dependent spectra of adsorbed 2,2'-bipyridine on the Au(111) surface during positive potential excursions (2j+ 1= 7) (corresponding to a 300 mV window). The plots should be read from bottom to top corresponding to the potential sweep direction. At -0.65 V, a wide set of peaks in the region between 1000 cm^{-1} and 1035 cm^{-1} (peaks **I**, **J**, **K**, **L**) is assigned to ring breathing modes and the positive sign in the PCMW2D indicates these modes increase in intensity with potential. The positive correlation extends to -0.30 V at 1006 cm^{-1} and -0.35 V at 1012 cm^{-1}. At -0.65 V, the corresponding plot for the C – C inter-ring stretching modes (peaks **Q** and **R**) (Figure 4.3C) presents a positive band in the range of 1302 cm^{-1} to 1322 cm^{-1}, with positive correlation at 1304 cm^{-1} extending to -0.20 V.

As the potential becomes more positive, two negative regions are observed in Figure 4.3A. The first one starts at -0.55 V in the 1019 cm^{-1} to 1035 cm^{-1} region, with minimum correlation peaks at (1034 cm^{-1} × -0.15 V) and (1024 cm^{-1} × -0.10 V). A second set of negative peaks in this wavenumber region occurs at (1025 cm^{-1} × 0.35 V) and (1034 cm^{-1} × 0.35 V). Another negative correlation region develops in the range of 998 cm^{-1} to 1019 cm^{-1} by -0.25 V. There is a general blue shift as the potential is scanned in the positive direction with negative correlation peaks at (1008 cm^{-1} × 0.35 V) and (1013 cm^{-1} × 0.55 V). By 0.85 V, this negative correlation region has shifted to 1019 cm^{-1}. Synchronous PCMW2D correlation peak maxima are identified as the local maximum gradient of the spectral intensity variation along potential, while correlation valley minima are identified as the local minimum gradient.

The negative correlation valleys in the ring breathing mode region have counterparts in the C – C inter-ring stretching mode region as illustrated in Figure 4.3C. A negative correlation region begins by -0.60 V and peaks at (1320 cm^{-1} × -0.15 V) and (1319 cm^{-1} × 0.35 V). Another negative correlation regions is present by 0 V at 1304 cm^{-1} and peaks at (1304 cm^{-1} × 0.60 V) and (1307 cm^{-1} × 0.75 V).

The analysis of Figures 4.3B and 4.3D, representing the corresponding synchronous PCMW2D plot calculated with SHINERS spectra of adsorbed 2,2'-bipyridine on Au(100), shows similar trends to that observed on Au(111). Positive and negative correlation regions on each surface share similar footprints with slight differences in correlation peak positions. The minima and maxima for Figure 4.3 are tabulated in supporting information Table 4.5 for each surface.

The corresponding synchronous PCMW2D correlation plots calculated from potential-dependent SHINERS spectra of 2,2'-bipyridine adsorbed on Au(111) and Au(100) during the cathodic potential excursions are presented in Figure 4.4. In these spectra the linearly decreasing potential means that negative peaks are associated with an *increase* in spectral intensity, in contrast to the case in Figure 4.3. In addition, the correlation plots should be read from the top to the bottom. For Au(111), a negative correlation valley bottom in Figure 4.4A, initially centered at 1018 cm^{-1} appears by 0.60 V and red shifts to 1002 cm^{-1} by -0.50 V; this region contains a peak centered at (1014 cm^{-1} × 0.10 V). Almost simultaneously in Figure 4.4C, in the C – C inter-ring stretching mode region, a negative correlation valley appears at 1307 cm^{-1} by 0.60 V, peaks at (1305 cm^{-1} × 0.15 V), and evolves with a red shift until it vanishes around 1302 cm^{-1} at -0.25 V.

In Figure 4.4A, another negative valley in the ring breathing mode region develops in the range of 1020 cm^{-1} to 1038 cm^{-1} by -0.10 V and evolves with a slightly red shift. These negative correlations peak at (1024 cm^{-1} × -0.65 V) and (1034 cm^{-1} × -0.65 V). Almost concurrently, a positive correlation region (negative spectral intensity changes) extending from 1018 cm^{-1} at -0.20 V evolves to a range of 1002 cm^{-1} to 1014 cm^{-1} by -0.65 V, with positive correlation peaks at (1016 cm^{-1} × -0.35 V) and (1011 cm^{-1} × -0.65 V). Meanwhile, in Figure 4.4C, a second negative correlation region develops at 1320 cm^{-1} by 0 V and peaks at (1320 cm^{-1} × -0.65 V). A positive correlation region appears by -0.45 V at 1304 cm^{-1} and peaks at (1304 cm^{-1} × -0.65 V).

A comparison between the Figures 4.4A and 4.4C reveals that generally the same valleys and peaks appear in the ring breathing mode region on both Au(111) and Au(100). Similarly, the synchronous PCMW2D correlation plots in the C – C interring stretching modes region are very similar from Au(111) to Au(100) as seen in Figures 4.4C and 4.4D. The slight differences can

again be noted by the Table 4.5. Overall though, the main differences between PCMW2D on each surface is that the magnitude of synchronous correlations on Au(100) is about twice that measured on Au(111), indicating a higher gradient of the spectral intensity variations along the perturbation direction in Au(100) caused by a stronger interaction between 2,2'-bipyridine molecules and the electrode surface. The information obtained about the potential dependent intensity variations using PCMW2D synchronous correlation plots was used to identify potential ranges of complicated spectral variations for further investigation by 2DCOS.

Generalized Two-Dimensional Correlation Spectroscopy: Positive Sweep

In order to extract more detailed information about the structural evolution of the 2,2'-bipyridine molecules on Au occuring during the polarization process, 2DCOS was applied to selected potential ranges: between -0.8 V to -0.60V, between -0.35 V to 0.40 V, and between 0.40 V to 1.0 V in the positive sweep for SHINERS spectra collected on both surfaces. To simplify discussion, the correlation results on Au(111) are the focus of analysis, with comparisons made to differences observed on Au(100) correlation plots when they arise. Additionally, correlation peaks will be identified by their letter assignment from Figure 4.1 with the exact wavenumber peaks being identified in supporting information Tables 4.6 and 4.7. To summarize, the primary correlation peaks of interest from Figure 4.1 are **I** (1006 cm^{-1}), **J** (1011 cm^{-1}), **Y** (1016 cm^{-1} to 1019 cm-1), **K** (1024 cm^{-1}), **L** (1034 cm^{-1}), **Q** (1304 cm^{-1}), **Z** (1306 cm^{-1} to 1310 cm^{-1}), and **R** (1320 cm^{-1}). Detailed analysis of the correlation plots has also revealed vibrations that are occluded in the conventional spectra and are identified as **X** (994 cm^{-1} to 996 cm^{-1}), **α** (1316 cm^{-1} to 1318 cm^{-1}), and **β** (1030 cm^{-1}).

When the 2D correlation analysis was performed on the -0.8 V to -0.60 V potential range, variations in the intensities of **I**, **J**, **K**, and **L** were observed, as characterized by the positive sign of synchronous peaks with **R** (not shown). This positive synchronous correlation indicates a related cause or origin of these spectral variations.

Figure 4.5A displays synchronous correlation for the -0.35 V to 0.40 V potential range on Au(111) and Au(100), respectively. The positive synchronous peaks at (**R** × **L**) and (**R** × **K**) are consistent with the PCMW2D plots, which suggest the synchronization of ring breathing peaks at 1034 and 1024 cm^{-1} with C – C interring stretching mode band at 1320 cm^{-1}. In addition, a positive synchronous peak at (**R** × **I**) is present, suggesting the existence of a coupled or related origin of the spectral intensity variations measured at 1320 cm^{-1} with ring breathing mode peaks at 1006 cm^{-1}.

Figure 4.5C shows the asynchronous correlation in the -0.35 V to 0.40 V potential range on Au(111). Three positive asynchronous peaks correlating the ring breathing modes with C – C inter-ring stretching modes are observed at (**R** × **I**), (**R** × **J**), and (**R** × **X**), while five negative asynchronous peaks are seen at (***α*** × **K**), (***α*** × **L**), (**Q** × **K**), (**Q** × **L**), and (**Q** × **I**). The asynchronous peaks reveal an additional C – C inter-ring stretching band contribution around 1317 cm^{-1} (here named ***α***) partially obscured in the conventional 1D spectra. The synchronous and asynchronous correlation plots of 2,2'-bipyridine on Au(100) in Figures 4.5B and 4.5D are broadly similar to those of Au(111). The synchronous and asynchronous peaks on Au(111) are collected into supporting information Table 4.6, and peaks for Au(100) into Table 4.7.

The combination of the signs of synchronous and asynchronous signals in the -0.35 V to 0.40 V potential range on Au(111) has been tabulated in Table 4.2 to simplify interpretation of

sequential ordering on each surface as described above. Several positive correlations, (**K** × **J**) and (**L** × **J**), from peaks within the ring breathing region are also tabulated, though not shown in the figures. This indicates peaks **K** and **L** change before peak **J**. Other positive correlations associated with the peak **R**, (**R** × **I**), (**R** × **J**), and (**R** × **X**), indicate that spectral intensities at **R**, change prior to **I**, **J** and **X**. The negative correlations of the C-C inter-ring modes with the ring breathing modes at (**α** × **K**), (**α** × **L**), (**Q** × **X**), (**Q** × **I**), (**Q** × **K**), and (**Q** × **L**) indicate that the spectral variations in the ring breathing modes **I**, **K**, and **L** occur before the corresponding C-C inter-ring modes **α** and **Q**. The same transitions are observed for Au(100) with the exception of negative correlation at (**α** × **X**), rather than the positive correlation observed on Au(111) at (**R** × **X**). Weak correlation of these peaks, particularly on Au(100), prevents definitive conclusions from being drawn regarding correlations of peak **X**, though it may indicate slight differences in 2,2'-bipyridine dynamics in this potential region. The sequential order (where → means 'before') of spectral intensity variations is **R** → **K** and **L** → **J** and **I** → **α** and **Q** in the -0.35 V to 0.40 V range. This sequential order seems to be consistent with the visual inspection of PCMW2D plots.

The 0.40 V to 1.0 V region produces 2DCOS correlation plots with significant numbers of peaks resulting from non-monotonic spectral intensity variations caused by low signal intensity as the 2,2'-bipyridine desorbs from the surface. Thus, only high intensity correlations are considered reliable. These plots are presented in the supporting information Figure 4.12. From Figure 4.12A, the 2,2'-bipyridine on Au(111) presents strong positive synchronous correlation peaks at (**Z** × **Y**), (**Z** × **L**), (**α** × **Y**), and (**α** × **L**). Similar synchronous peaks are observed on Au(100) in Figure 4.12B. Positive asynchronous correlations for 2,2'-bipyridine on

Au(111) appear at (**α** × **Y**), (**Q** × **Y**), while negative correlations present at (**Z** × **J**), (**Z** × **K**), and (**Z** × **L**). The sequence of spectral variation is as follows: **α** and **Q** → **J**, **K**, **L** → **Y** and **Z**.

Generalized Two-Dimensional Correlation Spectroscopy: Negative Sweep

To interpret the SHINERS spectra collected in the cathodic sweep, we performed 2DCOS analysis in two potential ranges, 0.50 to 0 V and -0.15 to -0.60 V. Figure 4.6A and 4.6B displays the synchronous correlations on Au(111) and Au(100), respectively, in the 0.50 V to 0 V range. In Figure 4.6A, the synchronous 2DCOS presents positive correlation peaks at (**Q** × **Y**) and (**Q** × **L**), indicating these peaks change in phase. Similar peaks are observed for Au(100) in Figure 4.6B and are found in supporting information Table 4.7.

The corresponding asynchronous plots in Figure 4.6C present both positive (**Z** × **J**), (**Z** × **I**), and (**Z** × **X**), as well as a negative (**Q** × **Y**), correlation peak. Very weak asynchronous correlations are also observed at (**Z** × **L**), (**R** × **Y**), (**Q** × **β**), and (**Q** × **L**) and are not considered when determining spectral variations in this region. The spectral intensities of **K**, **β**, **L**, and **R** do not change significantly until potentials negative of 0 V, thereby explaining the incredibly weak correlations at these correlation peaks. Peak **β** at 1030 cm^{-1} is a new correlation observed that was previously occluded in the conventional spectra. Table 4.3 compiles the identical combination of signs of each correlation peak on Au(111) and Au(100). Taken together, the sequence of spectral variation is **Z** → **I**, **J**, and **X**, as well as **Y** → **Q**.

Figure 4.7A and 4.7B presents the 2DCOS synchronous correlation spectra in the potential range -0.15 V to -0.60 V on both Au(111) and Au(100), respectively. Figure 4.7A of 2,2'-bipyridine on Au(111) presents six positive synchronous peaks at (**R** × **I**), (**R** × **K**), (**R** × **L**), (**Q** × **I**), (**Q** × **K**), and (**Q** × **L**) as well as a negative synchronous correlation peak at (**R** × **Y**). In

contrast, Figure 4.7B of 2,2'-bipyridine on Au(100) contains a significantly different set of synchronous correlation peaks. Four positive peaks are observed at (**R** × **I**), (**R** × **K**), (**R** × **L**), and (**Q** × **J**) along with four negative peaks observed at (**R** × **Y**), (**Q** × **I**), (**Q** × **K**), and (**Q** × **L**).

In the asynchronous spectra in Figure 4.7C, negative correlation peaks are observed at (**R** × **J**), (**R** × **K**), (**R** × **β**), (**R** × **L**), and (**Q** × **Y**). Four positive correlation peaks at (**R** × **Y**), (**Q** × **I**), (**Q** × **K**), and (**Q** × **L**) are also observed. The asynchronous correlation peaks in Figure 4.7D on Au(100) follow much the same pattern as on Au(111). The notable difference is that the region around 1320 cm^{-1} from 1024 cm^{-1} to 1035 cm^{-1} has a positive asynchronous correlation sign instead of being a negative region as in Figure 4.7C. Given the significant differences observed in the synchronous plots of 2,2'-bipyridine on Au(111) and Au(100), the correlation chart in Table 4.4 displays major differences between the adsorption dynamics on each surface in this potential range. These differences are charted in the correlation Table 4.4, and suggest a spectral variation sequence on Au(111) of **Q** → **L**, **β**, **K**, **J**, **I**, and **X** → **R** → **Y**. On Au(100), the spectral variation sequence is **J**, **I**, **X** → **R** → **L**, **β**, **K**, **Y** → **Q**.

Discussion

Positive Sweep

The assignment of observed spectral features is critical to the understanding of the dynamics of 2,2'-bipyridine adsorption on Au(111) and Au(100). The results of the anodic sweep indicate that four major contributions are found in the ring breathing mode region in the range between 990 cm^{-1} and 1040 cm^{-1} at negative electrode potentials; the four contributions at 1006 cm^{-1}, 1010 cm^{-1}, 1024 cm^{-1} and 1034 cm^{-1} (**I**, **J**, **K**, and **L**) are positively correlated with the 1320 cm^{-1} (**R**) in the synchronous plots. The C – C inter-ring stretching peak at 1320 cm^{-1} has

been assigned to adsorbed coplanar cis conformations of 2,2'-bipyridine species such as in $Zn(bpy)Cl_2$[60, 157], $Ru(bpy)_2Cl_2$[158], and species adsorbed at low concentrations in AgBr sols.[150] The chelating action of 2,2'-bipyridine in these systems causes the ligand to adopt a cis conformation. Protonation of 2,2'-bipyridine has also been shown to cause conformational changes to a cis orientation, which also exhibits the C-C inter-ring stretch near 1320 cm^{-1}.[60, 159] This system is studied at neutral pH, excluding the possibility of 2,2'-bipyridine being protonated in the bulk solution environment. Therefore, the four ring breathing mode peaks at 1006 cm^{-1}, 1010 cm^{-1}, 1024 cm^{-1}, and 1034 cm^{-1} synchronizing with the C – C interring stretching peak at 1320 cm^{-1} allows assignment of these peaks to cis-oriented 2,2'-bipyridine species. Peaks from 990 cm^{-1} to 1000 cm^{-1} are attributed to solution phase 2,2'-bipyridine that is close enough to the SHINERS particles to experience EM enhancement. Solid and solution phase 2,2'-bipyridine typically adopts a trans conformation, and indeed the frequencies observed for peak **X** (996 cm^{-1}) support this assignment.[60, 150] Similarly, **Q** (1304 cm^{-1}) is assigned to trans C-C inter-ring stretches based upon solid and solution spectra of 2,2'-bipyridine.

Also in support of the assignment of cis oriented 2,2'-bipyridine species is the fact that potential dependent interaction of pyridine rings with substrate strongly influences the intra-ring force constants, and thus the vibrational shift and intensity. When considering the position of ring breathing mode peaks, the stronger the interaction, the higher the ring breathing mode peak upshift. Kim *et al*[148, 151], in their pioneering SERS investigation of potential-dependent 2,2'-bipyridine adsorption on halide-containing Ag electrode surface, suggested the peak at 1025 cm^{-1} (**K**) is associated with species in which the nitrogen atoms of the pyridine rings strongly chemisorb to silver atoms on the electrode surface to form a Lewis acid coordination structure. The ring deformation observed at 1034 cm^{-1} (**L**) is very close to that observed in $Zn(bpy)Cl_2$[60, 160]

and Ru-bipyridyl complexes[158], suggesting a strong intra-ring force constant by interaction of ligand with the Au surface. According to Gao et. al.[161] and Takahashi et. al.[162], a face-on orientation, featuring a metal to π* orbitals, or π orbitals to metal, leads to a significant downshift in ν_1 for benzene and substituted aromatics. This analogous interaction can be applied to the 2,2'-bipyridine systems, leading to an assignment of flat oriented 2,2'-bipyridine at 1006 cm^{-1} (**I**). This observation is also corroborated by Kim et. al.[151], who observe lower frequency (1003 cm^{-1} to 1005 cm^{-1}) ring breathing modes at very negative potentials on Ag electrodes, which is ascribed to a physisorbed state.

While **I** (1006 cm^{-1}) is attributed to π-flat cis-2,2'-bipyridine and **K** (1024 cm^{-1}), and **L** (1034 cm^{-1}) are attributed to strongly adsorbed N-bound 2,2'-bipyridine states, peak **J** (1010 cm^{-1}) matches known vibrations for cis oriented 2,2'-bipyridine on Ag surfaces protected by alkanethiols.[147] De Bonis, et al. determined that vibrations around 1010 cm^{-1} on Ag were the result of cis oriented 2,2'-bipyridine that was weakly adsorbed because all available direct binding sites were occupied by the SAM and closely matched 2,2'-bipyridine vibrations in cationic $Ag(bpy)_2^+$.[147-148] Relating to our system, the peak seen near 1010 cm^{-1} is assigned as cis 2,2'-bipyridine beyond the compact first monolayer, which still interacts with the chemical field. These molecules have a weaker interaction with the surface, resulting in less polarization of the adsorbate and a smaller frequency shift than those N-bound molecules that are fully chemisorbed. These molecules, along with those of solution phase trans 2,2'-bipyridine, can be observed because of the long-range EM enhancement mechanism and the fact that the enhancement probe rests on the surface, rather than beneath the film.

Brolo, et al. observed 2,2'-bipyridine vibrations around 1015 cm^{-1} (**Y**) and 1307 cm^{-1} (**Z**) as the Au surface was scanned toward negative potentials, similar to our own results. These

vibrations are assigned to a torsional cisoid configuration of 2,2'-bipyridine on the surface.[60] This configuration is considered to be a reasonable intermediate state between the trans 2,2'-bipyridine in the bulk solution and the cis oriented 2,2'-bipyridine physisorbed and chemisorbed on the Au surfaces.

At this moment, we can start developing a molecular picture of 2,2'-bipyridine organization at the electrode-electrolyte interface upon the anodic polarization. A proposed schematic of molecular transitions is shown in the cartoon in Figure 4.8. At very negative potentials, the spectral intensity increase observed during the positive sweep is consistent with the previous thermodynamic investigation in which the surface concentration vs. potential plots show that the 2,2'-bipyridine starts to adsorb at ~-0.75 V vs. SCE.[136] The same authors postulated that 2,2'-bipyridine molecules adsorb in a flat (π-bonded) coplanar s-trans configuration in the lowest surface concentration, corresponding to very cathodic potentials. But, as the above discussion suggests, the synchronous correlation between the three ring breathing mode peaks at 1006 cm^{-1}, 1010 cm^{-1}, 1024 cm^{-1}, and 1034 cm^{-1} with the C – C interring stretching peak at 1320 cm^{-1}, **R**, together with asynchronous correlation at (**Q** × **I**) rules out the possibility of coplanar s-trans configuration of adsorbed species and suggests rather a cis orientation. The C – C interring stretching band contribution at 1304 cm^{-1}, **Q**, coincides with the same band of dissolved trans 2,2'-bipyridine in neutral solution.[60]

Interestingly, our data show the presence of four cis 2,2'bipyridine ring breathing mode contributions even at very cathodic potentials. This strongly suggests that 2,2'-bipyridine at these potentials is not completely adsorbed in the π-flat cis configuration as previously proposed.[60, 136] Rather, the organization of 2,2'-bipyridine can be understood as a mixed state comprising flat (π-bonded) and vertical (N-bound) coplanar cis configurations, along with the

trans oriented solution phase in very cathodic potentials. This situation is represented in the first panel of Figure 4.8. Vertical N-bound cis 2,2'-bipyridine (peaks **K** and **L**) is in the compact first monolayer along with π-flat cis molecules (peak **I**). Beyond this compact layer are vertically oriented cis 2,2'-bipyridine molecules unable to chemisorb because of a lack of available surface sites (peak **J**). This suggestion is consistent with STM studies that showed individual 2,2'-bipyridine molecules are randomly oriented in a mostly disordered phase at low electrode potentials, but begin to line up in parallel as the potentials reaches a critical value via a first-order phase transition.[163]

As potential is scanned from -0.8 V to more positive potentials, the compact first monolayer develops more order. This situation is represented by the second panel in Figure 4.8. While that allows for greater surface concentration of 2,2'-bipyridine, the close contact of the molecules in the film reduces polarizability of 2,2'-bipyridine in this phase. This results in decreased SHINERS intensity as the film is polarized to more positive potentials as observed by PCMW2D in Figure 4.3A for Au(111), particularly for peaks **K**, **L**, and **R**. Concurrently, in the region from -0.6 V to -0.2 V, peaks associated with species in the layers beyond the compact layer still increase in intensity because the surface loses the negative charge that would otherwise repulse the negative dipole of 2,2'-bipyridine. Similar behavior was cited by Stolberg et al. of pyridine on polycrystalline Au, which was explained by invoking a model that high coverage of the adsorbed molecules depolarize the electromagnetic field, reducing SERS intensity.[154, 164] Concurrently, the development of an overlayer also causes scattering of laser intensity that further reduces the amount of Raman scattering that can occur at the surface, again lowering intensity of peaks originating from those species.

2D Correlation Spectroscopy in the range of -0.35 V to 0.40 V, displayed in Figure 4.5, also sheds some light on these transitions. The first interesting corellations to note, as summarized in Table 4.2, is that peak **R** changes before peaks **I** and **J**, but after peaks **K** and **L**. Peaks **I**, **J**, **K**, and **L** have all been identified as originated from cis-oriented 2,2'-bipyridine. This is another indication of multiple cis-oriented species on the surface, with molecules represented by peaks **I** and **J** in the extended adsorption layer behaving differently from molecules directly chemisorbed to the Au surface with vibrations at peaks **K** and **L**. This fact is also corroborated by direct investigation of Figure 4.3A, demonstrating that indeed peaks **K** and **L** decrease well before those of **I** and **J**. Additionally, 2D corellations not shown in figures indicated that peaks at **K** and **L** change before the peak at **J**. The sequential order of peak variation derived by the combination of signs, tabulated in Table 4.2, confirms the above determinations. All correlations with peak **Q** are negative, showing that the trans species exhibits different spectral variations than the various cis oriented molecules and further indicate the cis-orientation of 2,2'-bipyridine is present at the surfaces.

As potential is scanned positive beyond 0.4 V, all peaks decline in intensity as desorption processes take hold. The nature of this desorption can be inferred by the presence of a blue shift in the negative correlation region in the PCMW2D Figure 3A. This shifts to roughly 1019 cm^{-1} (peak **Y**) by 0.85 V, and by that point is the only negative correlation region still observed. Interestingly, 2DCOS also shows that correlation peaks at **Y**, and **Z** exhibit positive synchronous correlation, consistent with the PCMW2D plots. Literature recognizes there are stable torsional intermediates between the trans and cis conformers for 2,2'-bipyridine. Brolo, et al. observed vibrational frequencies in this range during cathodic polarization and attributed them to a torsional conformation.[60] This is broadly consistent with findings from Hoon-Khosla, et al. that

suggest there is little distinction spectrally between the cisoid torsional state and the cis orientation.[135] Thus, these peaks are assigned to the torsional cisoid configurations of 2,2-bipyridine. All other 2,2'-bipyridine species have either already desorbed or have transitioned to this species before desorbing in this potential range. This intermediate is then desorbed by 1.0 V as the Au surface becomes oxidized. This process is shown in the third panel of Figure 4.8.

Another interesting observation to note on the positively polarized surface is the slight red shift of peak **R** to roughly 1317 cm^{-1} (peak **α**). At more positive potentials, spectral transitions no longer occur at R, but instead at α. We hypothesize this dual frequency of cis N-bound 2,2'-bipyridine could be the result of compact film reorientation as observed in STM studies of 2,2'-bipyridine on Au.[61, 137] Changes in the film ordering change the energy of the C-C inter-ring stretching mode, causing a slight shift in frequency.

The primary spectral pattern difference noted between the two surfaces is the positive correlation of peak **R** with peak **X** on Au(111), while the correlation of **α** with **X** on Au(100) is negative in the range of -0.35 V to 0.40 V. This difference is not considered significant because it involves weak correlations between the surface adsorbed molecules and the bulk solution.

Negative Sweep

The potential range of 0.55 V to 0 V yielded similar transitions on each surface, as evidenced by the PCMW2D plots in Figure 4.4. Readsorption of 2,2'-bipyridine molecules begins by roughly 0.60 V. The first major contributions to the ring breathing modes and the C-C inter-ring stretching modes appear around 1018 cm^{-1} (**Y**) and 1307 cm^{-1} (**Z**), respectively. Peak **Y** was observed as the final 2,2'-bipyridine ring breathing mode present before full desorption during anodic polarization. From the previous assignments, a natural progression of 2,2'-

bipyridine adsorption emerges. 2,2'-bipyridine, initially in a trans configuration in bulk solution, adsorbs in a torsional configuration at the Au surface as potential becomes more negative and reduces surface Au oxide species. As negative polarization progresses, the species rotate yielding a cis orientation. This causes only slight shifts in the frequency of peak **Y**. This general process is depicted in the first panel of Figure 4.9.

Examination of the sequence of spectral variation generated from Figure 4.6 indicates that the cisoid C-C inter-ring stretch (**Z**) and the torsional ring breathing mode (**Y**) appears first. This is followed by **I**, **J**, **X**, and **Q**. **I** and **J** form an adsorption layer, without any compact monolayer present, while **Q** and **X** arise from solution 2,2'-bipyridine approaching the surface in range of the EM enhancement of the SHINERS particles. By 0 V, adsorption of cis N-bound is just beginning to appear (peaks **β** and **L**), but has very weak and unreliable correlations to study for the potential range of 0.5 V to 0 V, making any differences between the surfaces with regard to peak **L** trivial at these potentials.

In the potential range of -0.15 V to -0.60 V, synchronous 2D correlation peaks, as seen in Figure 4.7, associated with cis bpy (**R**, **I**, **K**, and **L**) indicate the reemergence of the cis 2,2'-bipyridine compact monolayer configurations previously observed in the anodic scans. The negative synchronous peak of (**R** × **Y**) shows that the torsional 2,2'-bipyridine species initially adsorbed to Au experiences spectral variations opposite from those of the cis oriented molecules. We postulate that the cisoid torsional 2,2'-bipyridine species is consumed as the compact monolayer is formed. This follows what is observed in Figure 4.4, where positive correlation (negative intensity changes) for peak **Y** occur simultaneously with negative correlations (positive intensity changes) for the cis π-flat and cis N-bound 2,2'-bipyridine. This transition is shown in the second panel of Figure 4.9. The third panel represents the final configuration (at -0.8 V)

where a mixed state of cis π-flat and cis N-bound 2,2'-bipyridine again predominates. This is in contrast to the anodic scan, where the compact layer was present along with an extended adsorption layer. In this case, the layers appear to be one in the same as the cis bound 2,2'-bipyridine is generated as the cisoid species is consumed. The absence of the extended adsorption layer during cathodic polarization is a possible explanation for the increased intensity of the first monolayer, as there is no longer a layer on top scattering the laser radiation.

Another observation to note is the decrease in spectral intensity of trans 2,2'-bipyridine associated with peak **Q**. This is a consequence of the repulsion of the negative dipole of bulk solution trans 2,2'-bipyridine from the increasingly negative charge of the Au surface. This phenomena also appears to affect the π-flat and weakly N-bound cis species, as the peaks associated with their adsorption (**I** and **J**) begin to decrease in intensity by -0.5 V. These species could either be completely desorbing, or as the cisoid species could be consumed to continue formation of the compact monolayer.

Examination of of the asynchronous corellation of bpy on Au(100) and Au(111) reveals similar sequences of transitions as the potential is scanned in the negative direction. However, with the differences observed in the synchronous correlation plots with cross peaks of peak **Q**, the combination of signs of synchronous and asynchronous plots results in vastly different sequencing of the spectral variations. The differential dynamics of the bpy film on Au(111) and Au(100) in the -0.15 V to -0.60 V range could be caused by the slight difference of surface energy.

Conclusions

We present here a detailed analysis of 2,2'-bipyridine adsorption on Au(111) and Au(100) using PCMW2D and 2DCOS on potential dependent SHINERS spectra. At negative potentials during anodic polarization, a disordered, mixed phase of π-flat cis and N-bound cis 2,2'-bipyridine develops, followed by formation of a compact first monolayer with an extended adsorption layer on top as potential is scanned in the positive direction. Desorption follows at positive potentials and proceeds through a torsional cisoid 2,2'-bipyridine species at positive electrode polarization. Cathodic polarization causes this cisoid species to readsorb, followed by formation of an adsorption layer consisting of weakly cis N-bound and π-flat 2,2'-bipyridine above 0 V. As potential is scanned in the negative direction, the compact layer of N-bound 2,2'-bipyridine reassembles as the torsional cisoid species is consumed. These transitions are depicted in cartoons in Figures 4.8 and 4.9.

Our work shows that SHINERS provides high signal to noise and exquisite spectral detail when examining potential dependent molecular adsorption to polished single crystal electrodes. The increased spectral detail paired with 2DCOS chemometric analysis of SHINERS spectra is an effective method for studying adsorption dynamics on single crystal surfaces. As an example, detailed analysis shows that while there are substantial similarities in the behavior of Au(111) and Au(100), they differ in an important respect on the cathodic sweep relating to the sequence of spectral variation in the range of -0.15 V to -0.60 V. The higher resolution provided by the 2D correlation also reveals new vibrations that otherwise were occluded by other peaks in the ring breathing modes and C-C inter-ring modes, thereby providing a better understanding of the potential dependent film dynamics. The utility of examing such structural transitions and chemical reactions at the electrifed solid/liquid interface is clear and will be used in the future.

Acknowledgements

We would like to thank the National Science Foundation for their generous support.

Supporting Information Available

Supporting information Table 4.5 features PCMW2D correlation peaks while Tables 4.6 and 4.7 feature 2DCOS correlation peaks for Au(111) and Au(100), respectively. Figure 4.10 displays a TEM micrograph of SHINERS particles. Figure 4.11 displays cyclic voltammetry of SHINERS particles adsorbed to glassy carbon. Figure 4.12 shows 2DCOS of 2,2'-bipyridine in the 0.4 V to 1.0 V potential range.

Tables

Table 4.1: Observed SHINERS peaks and assignments for 2,2'-bipyridine adsorbed on Au(100) and Au(111) at -0.2 V compared to previously reported examples.

Wavenumber (cm^{-1})			Peak	Wavenumber (cm^{-1})		Wilson no.	Assignment
Solid bpy	bpy ($_{aq}$)	$Zn(bpy)_2Cl_2$		Au(111)	Au(100)		
439		461	A	457	457	16b	o.p. ring def.
			B	496	496		Origin not clear
		639	C	643	641	6a	i.p. ring def.
653 (IR)		662	D	663	662	6b	i.p. ring def.
742 (IR)		733 (IR)	E	733	733	4	o.p. C-H def.
763	765	765	F	766	767	7a	i.p. ring def.
895 (IR)			G	883	881	10a	C-H wagging o.p.
			H	934	933		ClO_4^- symmetric stretch
994	1002	1030	X	996	996	1	Ring Breathing (trans solution)
			I	1006	1006	1	Ring Breathing (cis π-flat)
			J	1010	1010	1	Ring Breathing (physisorbed N-bound)
			Y	1019	1019	1	Ring Breathing (cisoid)
			K	1024	1024	1	Ring Breathing (cis N-bound)
			β	1030	1030	1	Ring Breathing (cis N-bound)
			L	1034	1034	1	Ring Breathing (cis N-bound)

Table 4.1 (Continued):

1044	1051	1063	M	1062	1064	12	C-H i.p. def. + ring str. and def.
1092		1101	N	1105	1106	18b	C-H i.p. def. + ring str.
1144	1156	1158	O	1170	1169	14	C-H i.p. def. + ring str.
1276	1276	1266	P	1272	1273	9a	Ring str. C-C, C-N + C-C Inter-ring str. + C-H i.p. def.
1300	1307	1299	Q	1304	1304	3	C-C inter-ring str. (trans)
			Z	1307	1307	3	C-C inter-ring str. (cisoid)
1307	1306	1314, 1322	α	1318	1318	3	C-C inter-ring str. (cis)
			R	1320	1320	3	C-C inter-ring str. (cis)
1445	1449	1447	S	1427	1429	19b	C=N str. + C-H i.p. def.
1481	1489	1493	T	1486	1485	19a	C=N str. + C-H i.p. def.
1571	1576	1569	U	1560	1559	8a	C=C str.
1589	1599	1599	V	1590	1589	8b	C=C str.
			W	1601	1600	8b	

Table 4.2: Combination of the signs of 2DCOS synchronous and asynchronous correlation signals obtained during the positive potential sweep in the range of -0.35 V to 0.40 V.

Au(111) - ν_2									
	R								
	α								
	Q								
	L		-	-					
	K		-	-					
	J	+			+	+			
	I	+		-					
	X	+		-					
ν_1		**R**	**α**	**Q**	**L**	**K**	**J**	**I**	**X**
Au(100) - ν_2									
	R								
	α								
	Q								
	L		-	-					
	K		-	-					
	J	+			+	+			
	I	+		-					
	X		-	-					

Table 4.3: Combination of the signs of 2DCOS synchronous and asynchronous correlation signals obtained during the negative potential sweep in the range of 0.50 V to 0 V.

Au(111) - ν_2	**R**										
	Z										
	Q										
	L										
	β										
	K										
	Y			-							
	J		+								
	I		+								
	X		+								
ν_1		**R**	**Z**	**Q**	**L**	**β**	**K**	**Y**	**J**	**I**	**X**
Au(100) - ν_2	**R**										
	Z										
	Q										
	L										
	β										
	K										
	Y			-							
	J		+								
	I		+								
	X		+								

Table 4.4: Combination of the signs of 2DCOS synchronous and asynchronous correlation signals obtained during the negative potential sweep in the range of -0.15 V to -0.60 V.

Au(111) - ν_2	**R**									
	Q									
	L	-	+							
	β	-								
	K	-	+							
	Y	+	+							
	J	-								
	I	-	+							
	X	-								
ν_1		**R**	**Q**	**L**	**β**	**K**	**Y**	**J**	**I**	**X**
Au(100) - ν_2	**R**									
	Q									
	L	+	-							
	β	+								
	K	+	-							
	Y	+	-							
	J	-								
	I	-	-							
	X	-								

Table 4.5: PCMW2D correlation peaks for 2,2'-bipyridine adsorbed on Au(111) and Au(100) during anodic and cathodic polarization.

Surface	Peak sign	Peak position
Anodic Scan		
Au(111)	+	(1006 cm^{-1} × -0.65 V)
	+	(1012 cm^{-1} × -0.65 V)
	+	(1024 cm^{-1} × -0.65 V)
	+	(1034 cm^{-1} × -0.65 V)
	+	(1304 cm^{-1} × -0.65 V)
	+	(1320 cm^{-1} × -0.65 V)
	-	(1024 cm^{-1} × -0.10 V)
	-	(1034 cm^{-1} × -0.15 V)
	-	(1320 cm^{-1} × -0.15 V)
	-	(1008 cm^{-1} × 0.35 V)
	-	(1025 cm^{-1} × 0.35 V)

Table 4.5 (Continued):

Au(111)	-	(1034 cm^{-1} × 0.35 V)
	-	(1319 cm^{-1} × 0.35 V)
	-	(1013 cm^{-1} × 0.55 V)
	-	(1304 cm^{-1} × 0.60 V)
	-	(1307 cm^{-1} × 0.75 V)
Au(100)	+	(1007 cm^{-1} × -0.65 V)
	+	(1013 cm^{-1} × -0.65 V)
	+	(1024 cm^{-1} × -0.65 V)
	+	(1034 cm^{-1} × -0.65 V)
	+	(1304 cm^{-1} × -0.65 V)
	+	(1320 cm^{-1} × -0.65 V)
	-	(1320 cm^{-1} × -0.30 V)
	-	(1024 cm^{-1} × -0.25 V)
	-	(1034 cm^{-1} × -0.25 V)
	-	(1005 cm^{-1} × 0.35 V)
	-	(1319 cm^{-1} × 0.40 V)
	-	(1034 cm^{-1} × 0.45 V)
	-	(1024 cm^{-1} × 0.50 V)
	-	(1307 cm^{-1} × 0.55 V)
	-	(1016 cm^{-1} × 0.60 V)
Cathodic Scan		
Au(111)	-	(1305 cm^{-1} × 0.15 V)
	-	(1014 cm^{-1} × 0.10 V)
	+	(1016 cm^{-1} × -0.35 V)
	+	(1011 cm^{-1} × -0.65 V)
	-	(1024 cm^{-1} × -0.65 V)
	-	(1034 cm^{-1} × -0.65 V)
	+	(1304 cm^{-1} × -0.65 V)
	-	(1320 cm^{-1} × -0.65 V)
Au(100)	-	(1304 cm^{-1} × 0.10 V)
	-	(1012 cm^{-1} × 0 V)
	+	(1011 cm^{-1} × -0.60 V)
	+	(1303 cm^{-1} × -0.60 V)
	-	(1024 cm^{-1} × -0.65 V)
	-	(1034 cm^{-1} × -0.65 V)
	-	(1319 cm^{-1} × -0.65 V)

Table 4.6: 2DCOS correlation peaks for 2,2'-bipyridine on Au(111).

Range	Peak sign	Peak Position
Synchronous		
-0.35 V to 0.40 V	+	1320 cm^{-1} × 1006 cm^{-1}
	+	1320 cm^{-1} × 1024 cm^{-1}
	+	1320 cm^{-1} × 1034 cm^{-1}
0.50 V to 0 V	+	1305 cm^{-1} × 1016 cm^{-1}
	+	1305 cm^{-1} × 1035 cm^{-1}
-0.15 V to -0.60 V	+	1320 cm^{-1} × 1005 cm^{-1}
	+	1320 cm^{-1} × 1024 cm^{-1}
	+	1320 cm^{-1} × 1034 cm^{-1}
	-	1320 cm^{-1} × 1016 cm^{-1}
	+	1302 cm^{-1} × 1006 cm^{-1}
	+	1302 cm^{-1} × 1024 cm^{-1}
	+	1302 cm^{-1} × 1035 cm^{-1}
Asynchronous		
-0.35 V to 0.40 V	+	1320 cm^{-1} × 996 cm^{-1}
	+	1320 cm^{-1} × 1006 cm^{-1}
	+	1320 cm^{-1} × 1010 cm^{-1}
	-	1318 cm^{-1} × 1023 cm^{-1}
	-	1317 cm^{-1} × 1034 cm^{-1}
	-	1303 cm^{-1} × 1006 cm^{-1}
	-	1303 cm^{-1} × 1024 cm^{-1}
	-	1303 cm^{-1} × 1034 cm^{-1}
0.50 V to 0 V	-	1319 cm^{-1} × 1019 cm^{-1}
	+	1310 cm^{-1} × 1011 cm^{-1}
	+	1308 cm^{-1} × 1006 cm^{-1}
	+	1307 cm^{-1} × 1037 cm^{-1}
	+	1306 cm^{-1} × 994 cm^{-1}
	-	1304 cm^{-1} × 1019 cm^{-1}
	-	1304 cm^{-1} × 1030 cm^{-1}
-0.15 V to -0.60 V	-	1321 cm^{-1} × 1024 cm^{-1}
	-	1321 cm^{-1} × 1030 cm^{-1}
	-	1320 cm^{-1} × 1011 cm^{-1}
	-	1320 cm^{-1} × 1035 cm^{-1}
	+	1319 cm^{-1} × 1019 cm^{-1}
	+	1304 cm^{-1} × 1005 cm^{-1}
	-	1303 cm^{-1} × 1016 cm^{-1}
	+	1303 cm^{-1} × 1024 cm^{-1}
	+	1303 cm^{-1} × 1033 cm^{-1}

Table 4.7: 2DCOS correlation peaks of 2,2'-bipyridine on Au(100).

Range	Peak sign	Peak Position
Synchronous		
-0.35 V to 0.40 V	+	1319 cm^{-1} × 1008 cm^{-1}
	+	1319 cm^{-1} × 1023 cm^{-1}
	+	1319 cm^{-1} × 1033 cm^{-1}
0.50 V to 0 V	+	1304 cm^{-1} × 1015 cm^{-1}
	+	1304 cm^{-1} × 1033 cm^{-1}
-0.15 V to -0.60 V	+	1319 cm^{-1} × 1005 cm^{-1}
	-	1319 cm^{-1} × 1015 cm^{-1}
	+	1319 cm^{-1} × 1024 cm^{-1}
	+	1319 cm^{-1} × 1034 cm^{-1}
	-	1305 cm^{-1} × 1002 cm^{-1}
	+	1304 cm^{-1} × 1013 cm^{-1}
	-	1304 cm^{-1} × 1024 cm^{-1}
	-	1304 cm^{-1} × 1034 cm^{-1}
Asynchronous		
-0.35 V to 0.40 V	+	1320 cm^{-1} × 1005 cm^{-1}
	+	1319 cm^{-1} × 1012 cm^{-1}
	-	1317 cm^{-1} × 1023 cm^{-1}
	-	1316 cm^{-1} × 1000 cm^{-1}
	-	1316 cm^{-1} × 1033 cm^{-1}
	-	1304 cm^{-1} × 1001 cm^{-1}
	-	1304 cm^{-1} × 1007 cm^{-1}
	-	1304 cm^{-1} × 1023 cm^{-1}
	-	1304 cm^{-1} × 1032 cm^{-1}
0.50 V to 0 V	-	1319 cm^{-1} × 1019 cm^{-1}
	+	1308 cm^{-1} × 1001 cm^{-1}
	+	1308 cm^{-1} × 1012 cm^{-1}
	+	1307 cm^{-1} × 996 cm^{-1}
	-	1304 cm^{-1} × 1030 cm^{-1}
	-	1304 cm^{-1} × 1037 cm^{-1}
	-	1303 cm^{-1} × 1018 cm^{-1}
-0.15 V to -0.60 V	-	1319 cm^{-1} × 1009 cm^{-1}
	+	1319 cm^{-1} × 1018 cm^{-1}
	+	1304 cm^{-1} × 1007 cm^{-1}
	-	1303 cm^{-1} × 1016 cm^{-1}
	+	1303 cm^{-1} × 1024 cm^{-1}
	+	1303 cm^{-1} × 1034 cm^{-1}

Figures

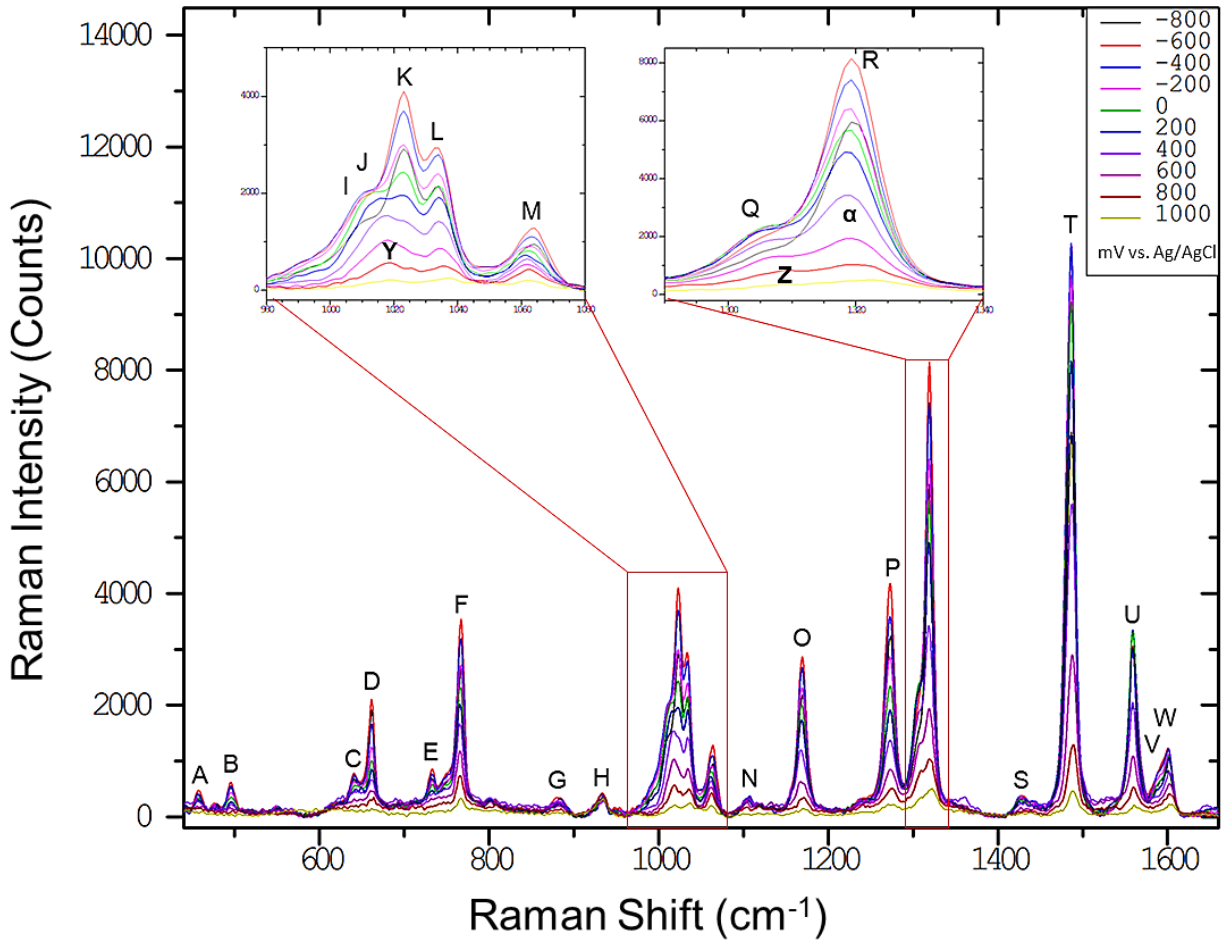

Figure 4.1: Background corrected SHINERS of 1 mM 2,2'-bipyridine in 0.1M $KClO_{4(aq)}$ on Au(100) under anodic polarization from -0.8 V to 1.0 V. Insets highlight the ring breathing region (980 – 1080 cm^{-1}) and the C-C inter-ring stretching region (1290 – 1340 cm^{-1}).

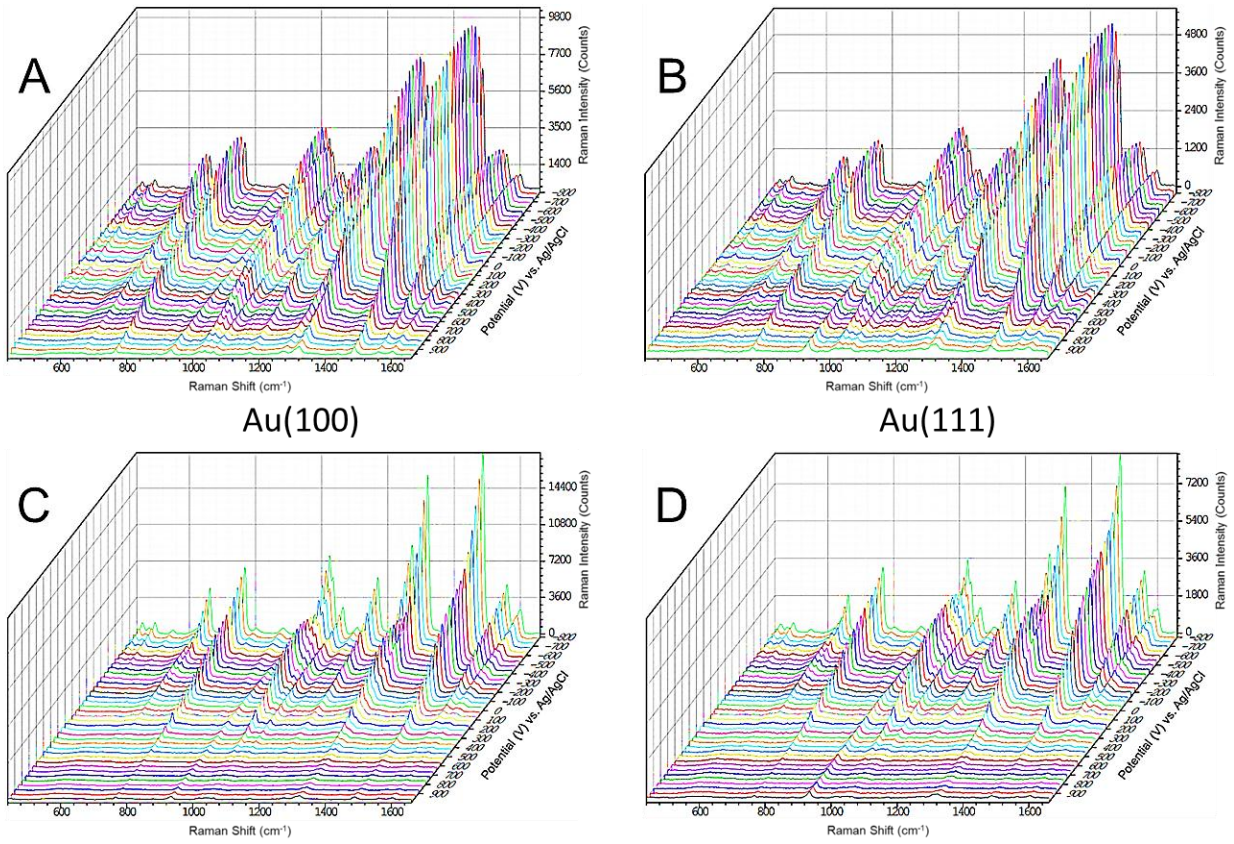

Figure 4.2: Background corrected SHINERS waterfall plots of 1 mM 2,2'-bipyridine in 0.1 M $KClO_{4(aq)}$. Anodic polarization on (A) Au(100) and (B) Au(111) and cathodic polarization on (C) Au(100) and (D) Au(111).

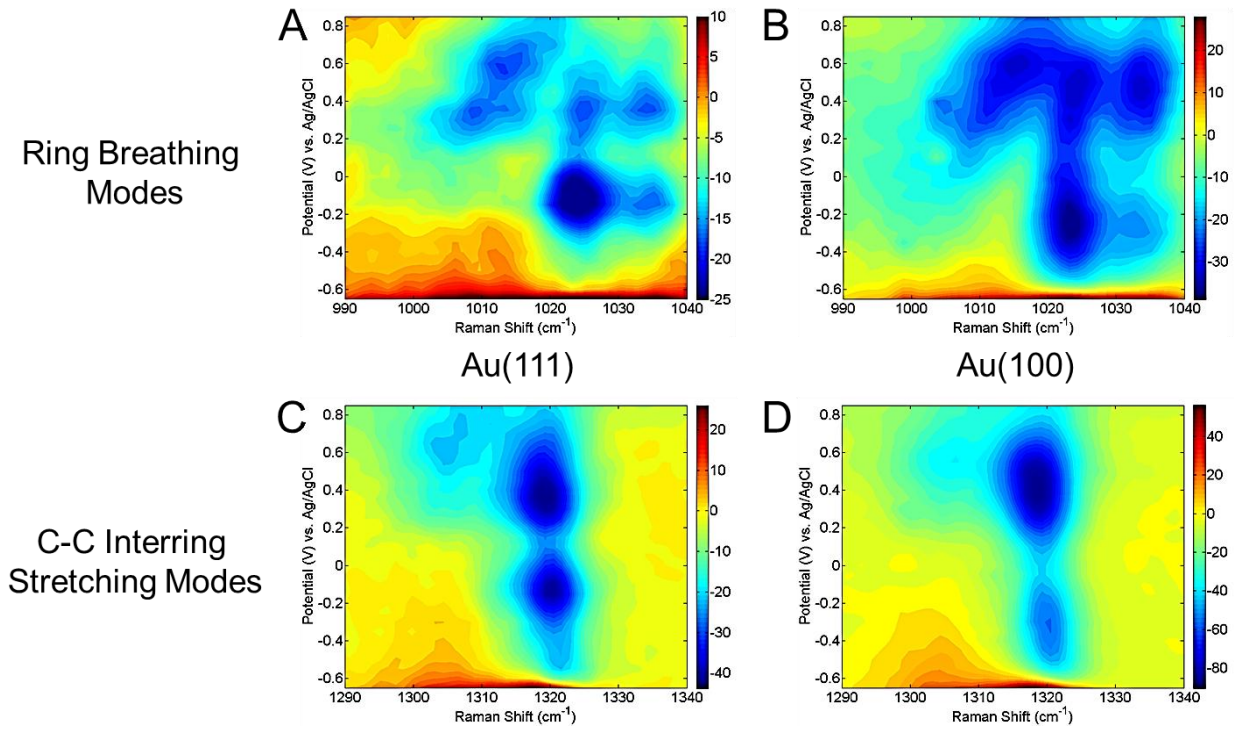

Figure 4.3: PCMW2D synchronous plots of 1 mM 2,2'-bipyridine in 0.1 M $KClO_{4(aq)}$ under anodic polarization. Plots read bottom to top. The ring breathing region on (A) Au(111) and (B) Au(100) as well as C-C inter-ring stretching region on (C) Au(111) and (D) Au(100) are shown.

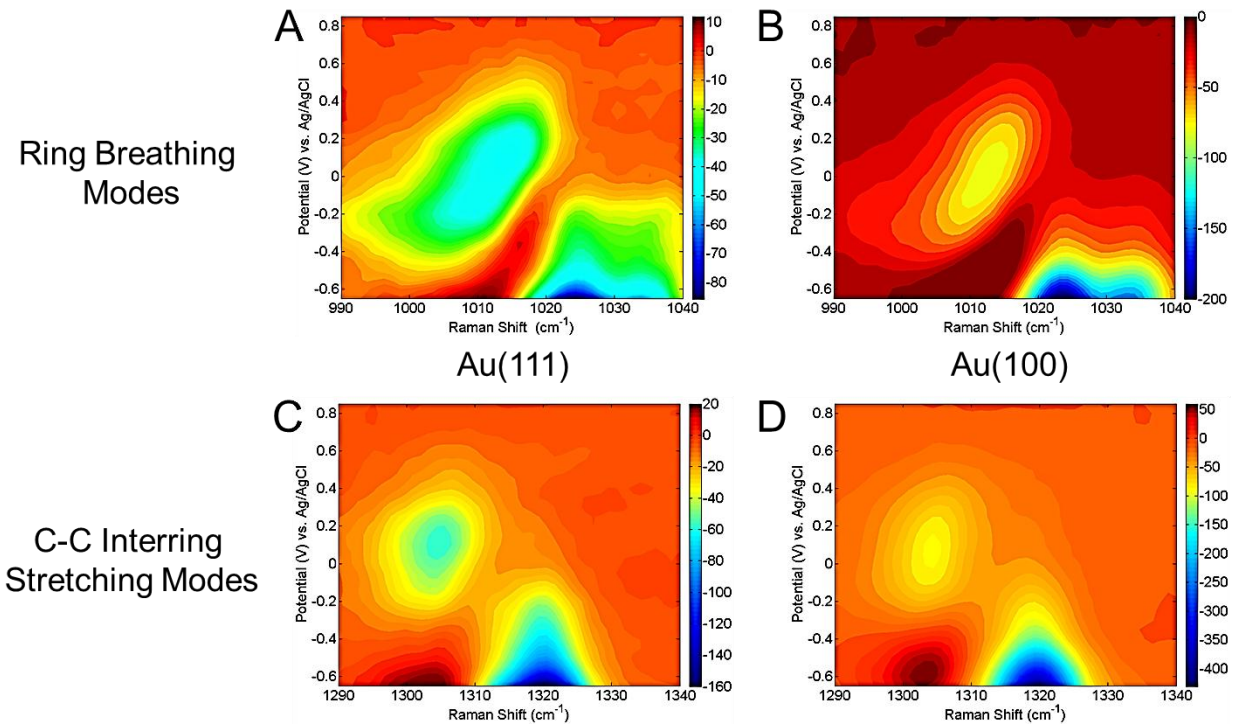

Figure 4.4: PCMW2D synchronous plots of 1 mM 2,2'-bipyridine in 0.1 M $KClO_{4(aq)}$ under cathodic polarization. Plots read top to bottom. The ring breathing region on (A) Au(111) and (B) Au(100) as well as C-C inter-ring stretching region on (C) Au(111) and (D) Au(100) are shown.

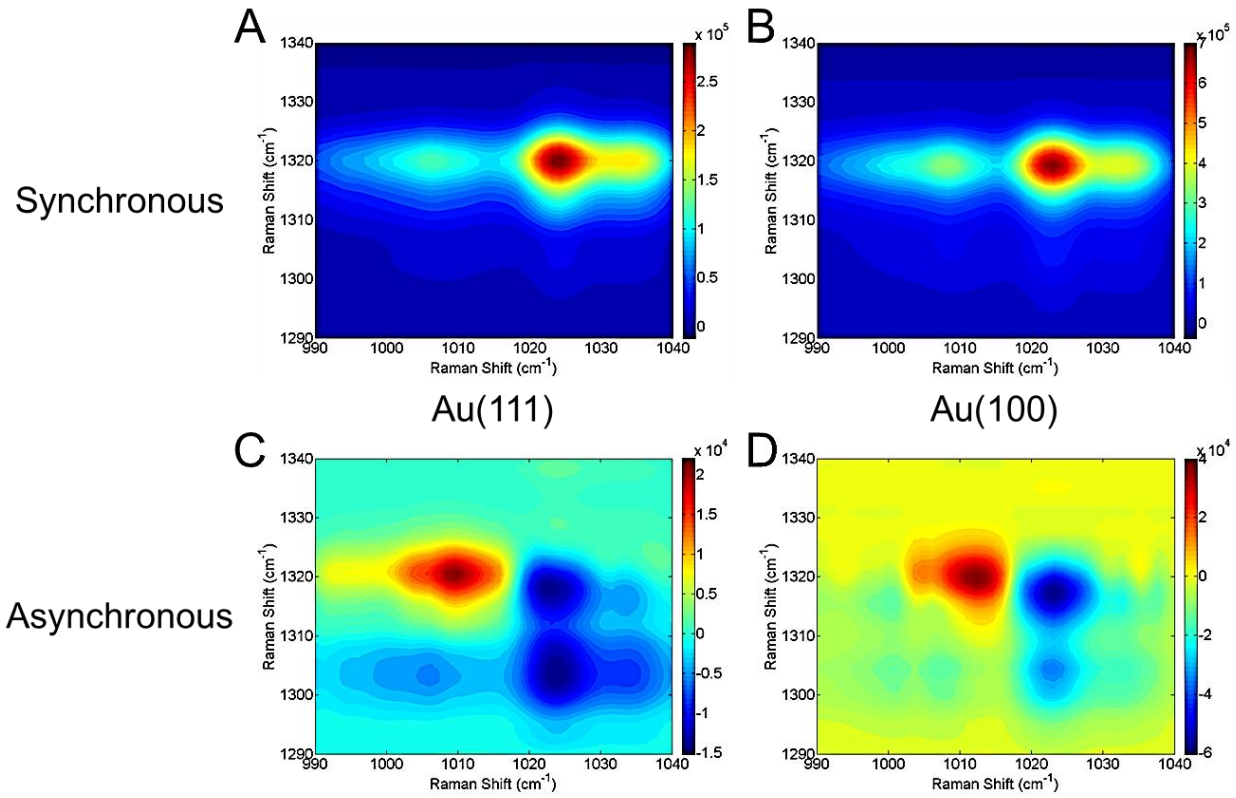

Figure 4.5: Hetero-mode 2DCOS correlation plots of 1 mM 2,2'-bipyridine in 0.1 M $KClO_{4(aq)}$ under anodic polarization from -0.35 V to 0.40 V. Synchronous plots for (A) Au(111) and (B) Au(100) as well as asynchronous plots for (C) Au(111) and (D) Au(100) are shown.

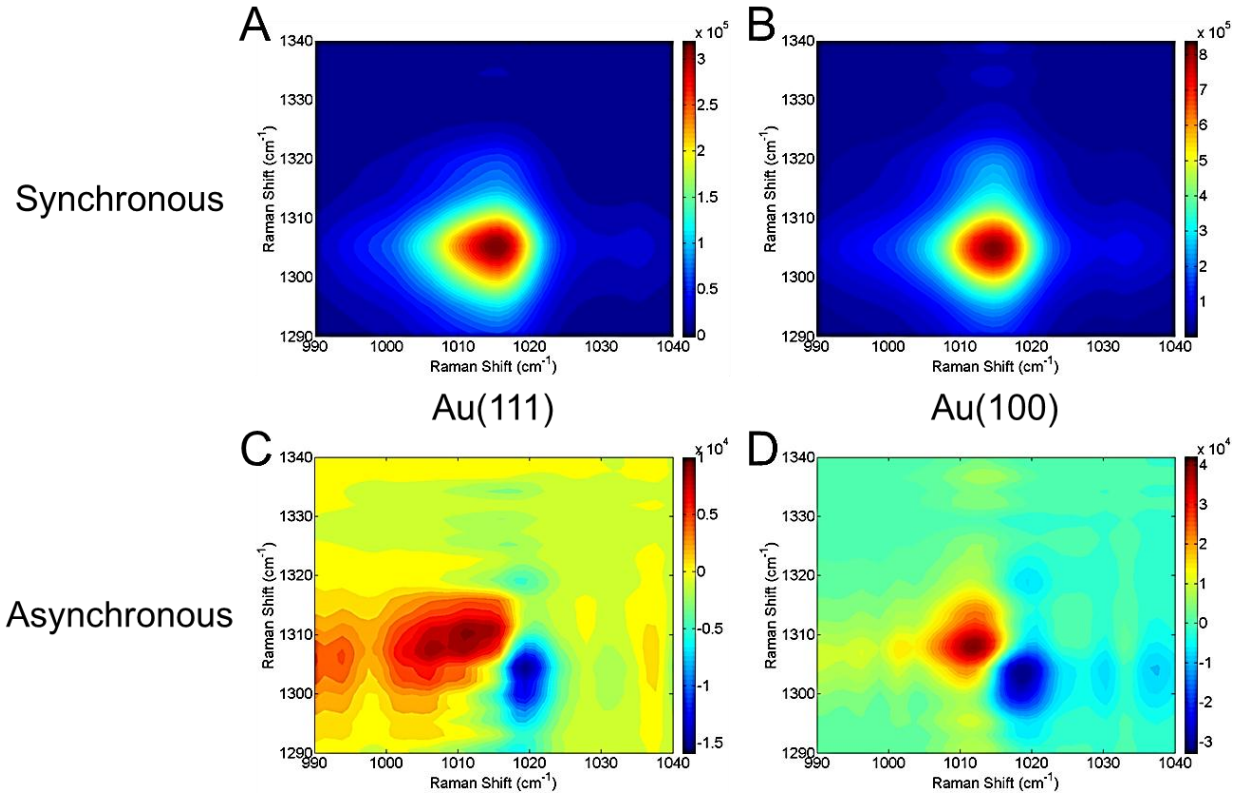

Figure 4.6: Hetero-mode 2DCOS correlation plots of 1 mM 2,2'-bipyridine in 0.1 M $KClO_{4(aq)}$ under cathodic polarization from 0.50 V to 0 V. Synchronous plots for (A) Au(111) and (B) Au(100) as well as asynchronous plots for (C) Au(111) and (D) Au(100) are shown.

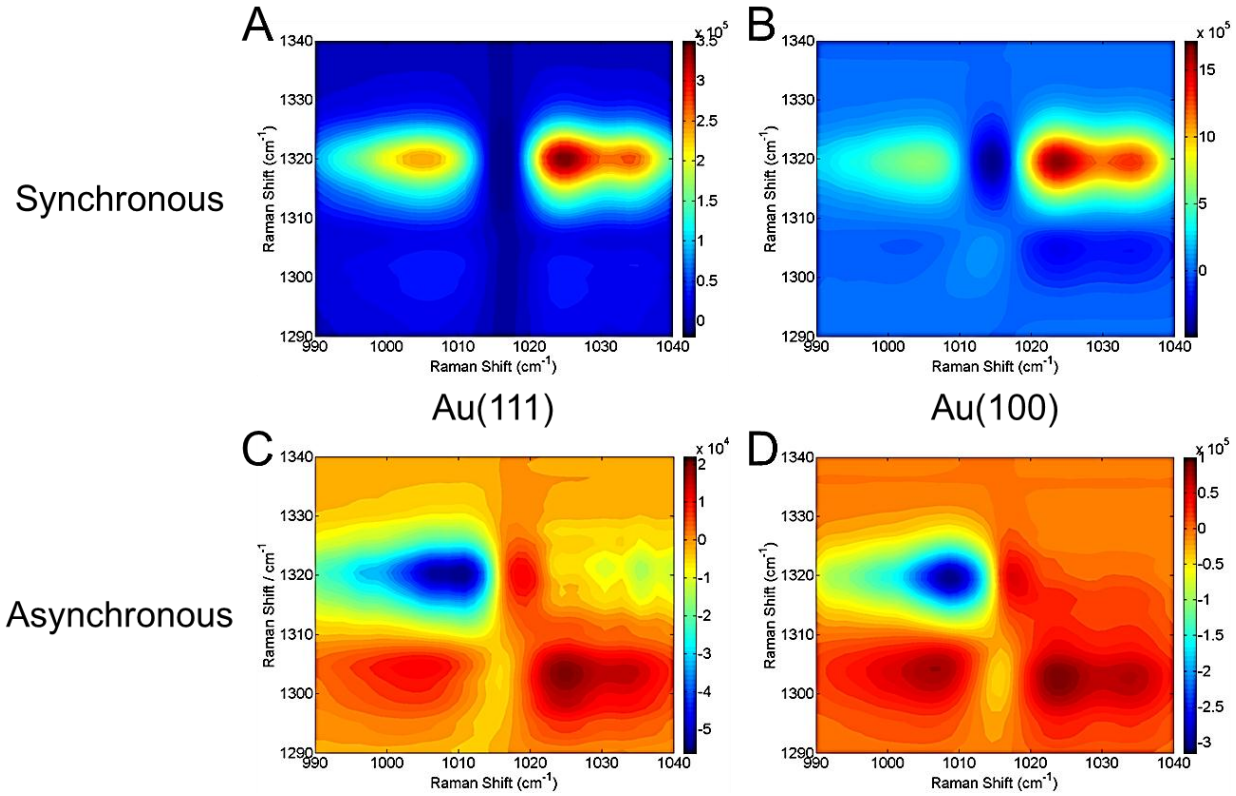

Figure 4.7: Hetero-mode 2DCOS correlation plots of 1 mM 2,2'-bipyridine in 0.1 M $KClO_{4(aq)}$ under cathodic polarization from -0.15 V to 0.60 V. Synchronous plots for (A) Au(111) and (B) Au(100) as well as asynchronous plots for (C) Au(111) and (D) Au(100) are shown.

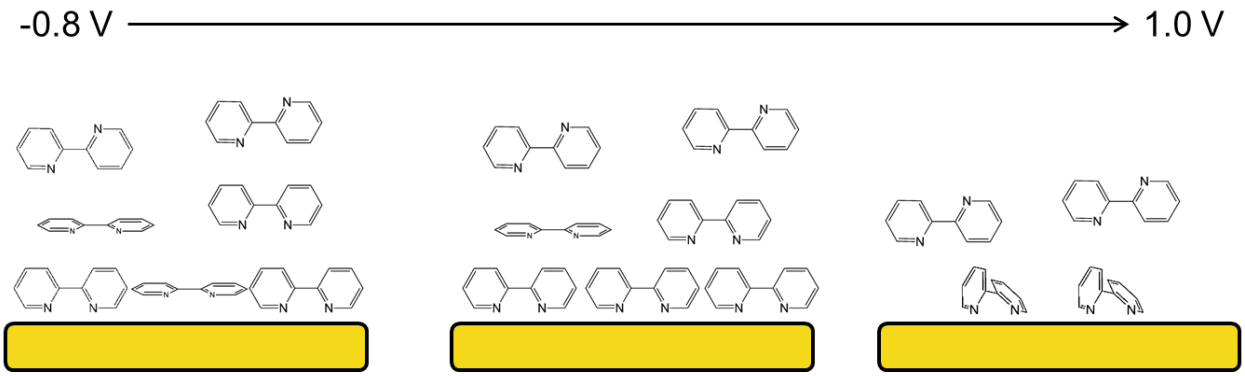

Figure 4.8: Schematic of 2,2'-bipyridine on Au(111) and Au(100) under anodic polarization. Compact adsorption layer at negative potentials along with an extended adsorption layer, followed by continued formation of a compact layer as potential is scanned positive. Desorption through a torsional intermediate occurs at the positive potential extreme.

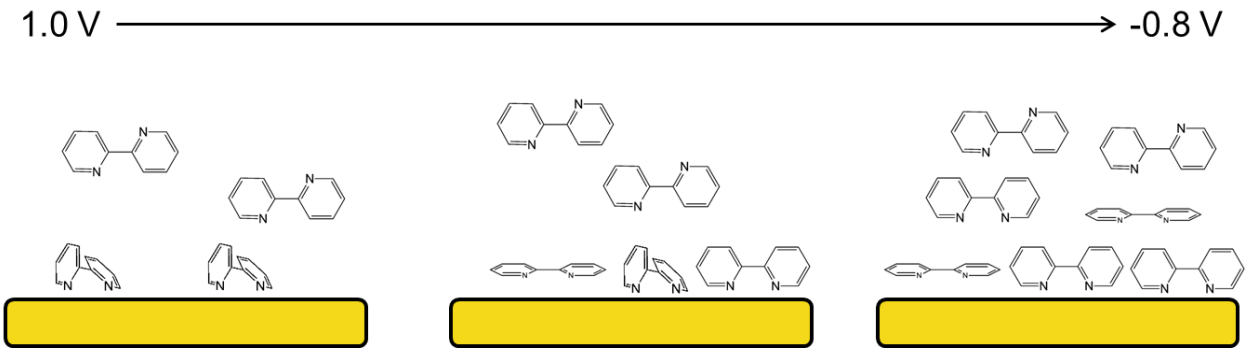

Figure 4.9: Schematic of 2,2'-bipyridine on Au(111) and Au(100) under cathodic polarization. Adsorption through a torsional state occurs at positive potentials. This state is consumed to form the compact layer as potential is scanned negatively.

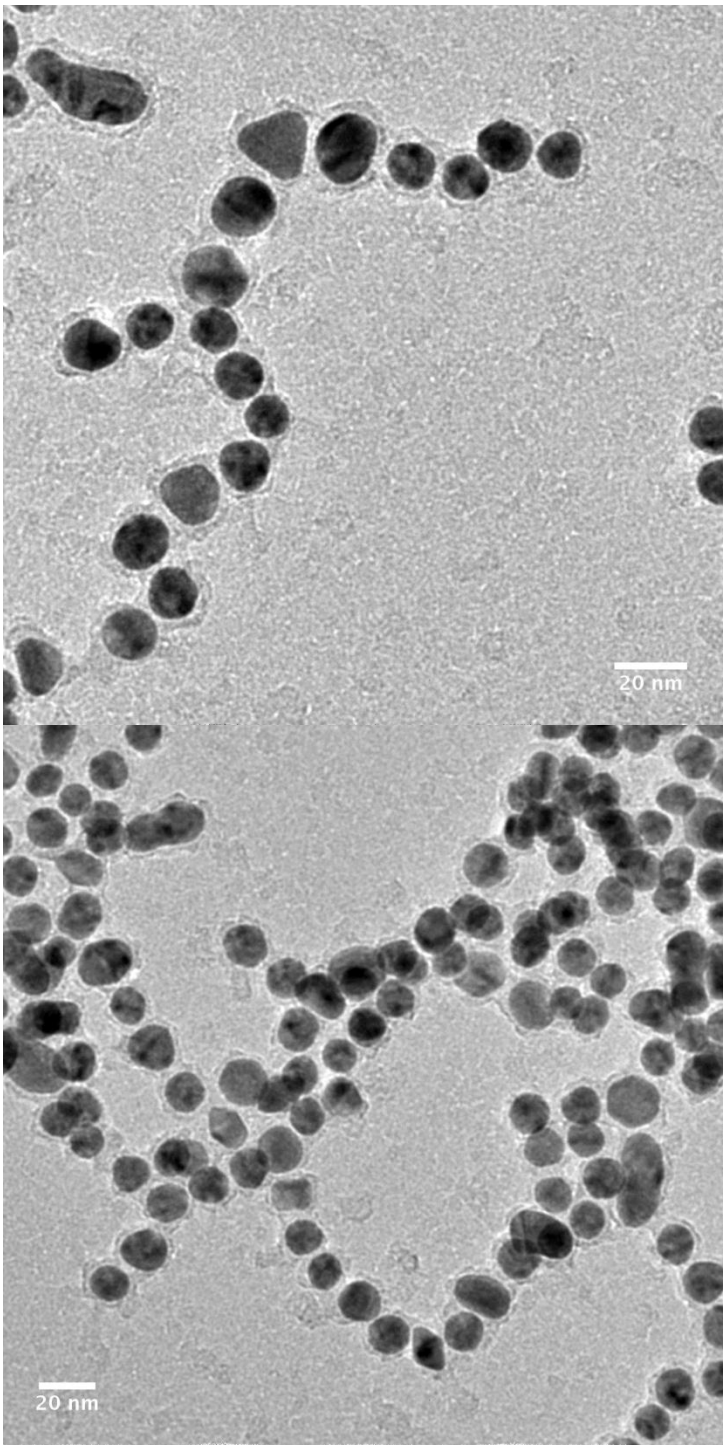

Figure 4.10: TEM images of SiO_2 capped Au nanoparticles with diameter of 16.7 ± 1.8 nm and silica shell thickness to be 2.6 ± 0.7 nm.

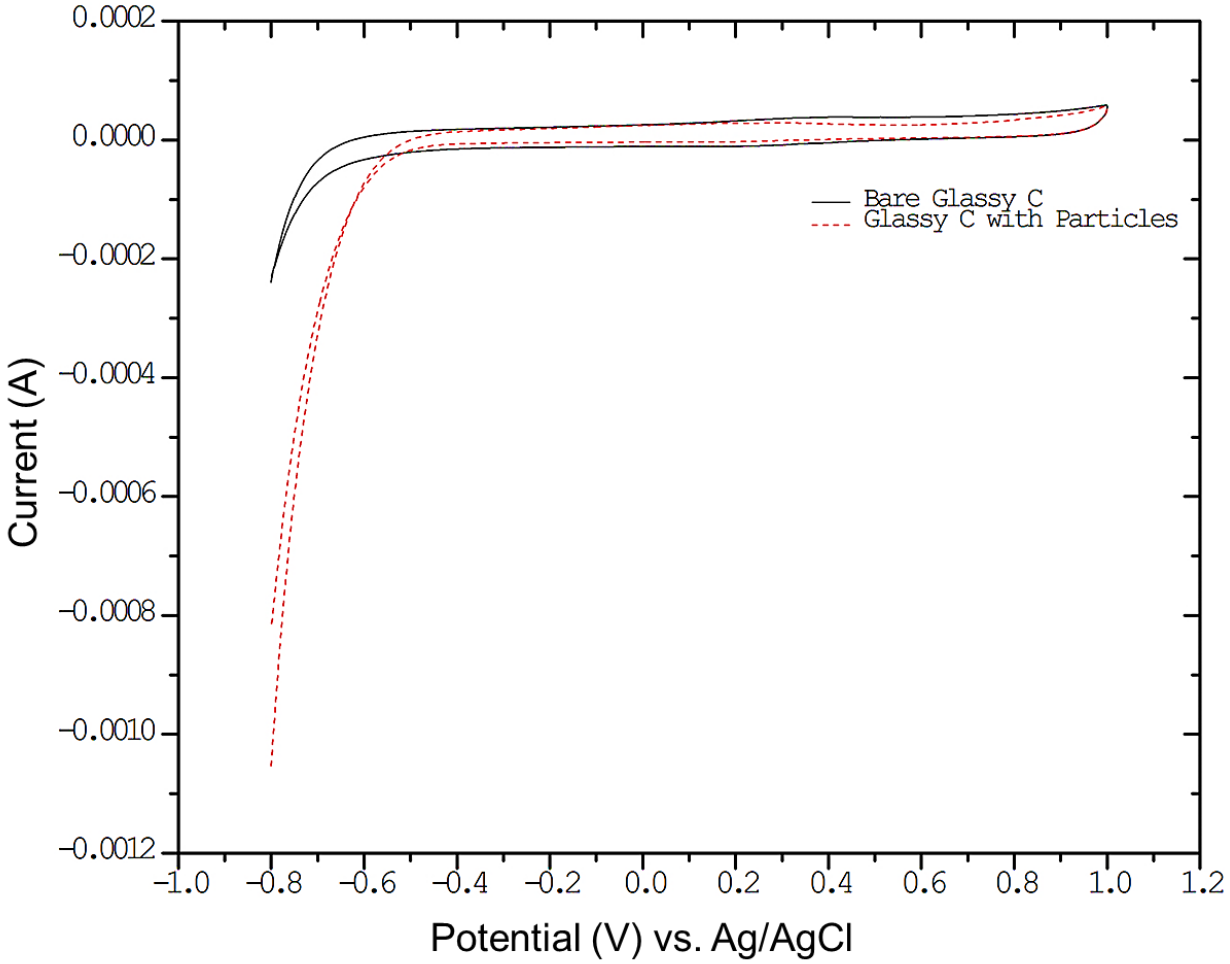

Figure 4.11: Cyclic voltammetry of SHINERS particles dropcast onto glassy C in 0.5 M $H_2SO_{2(aq)}$.

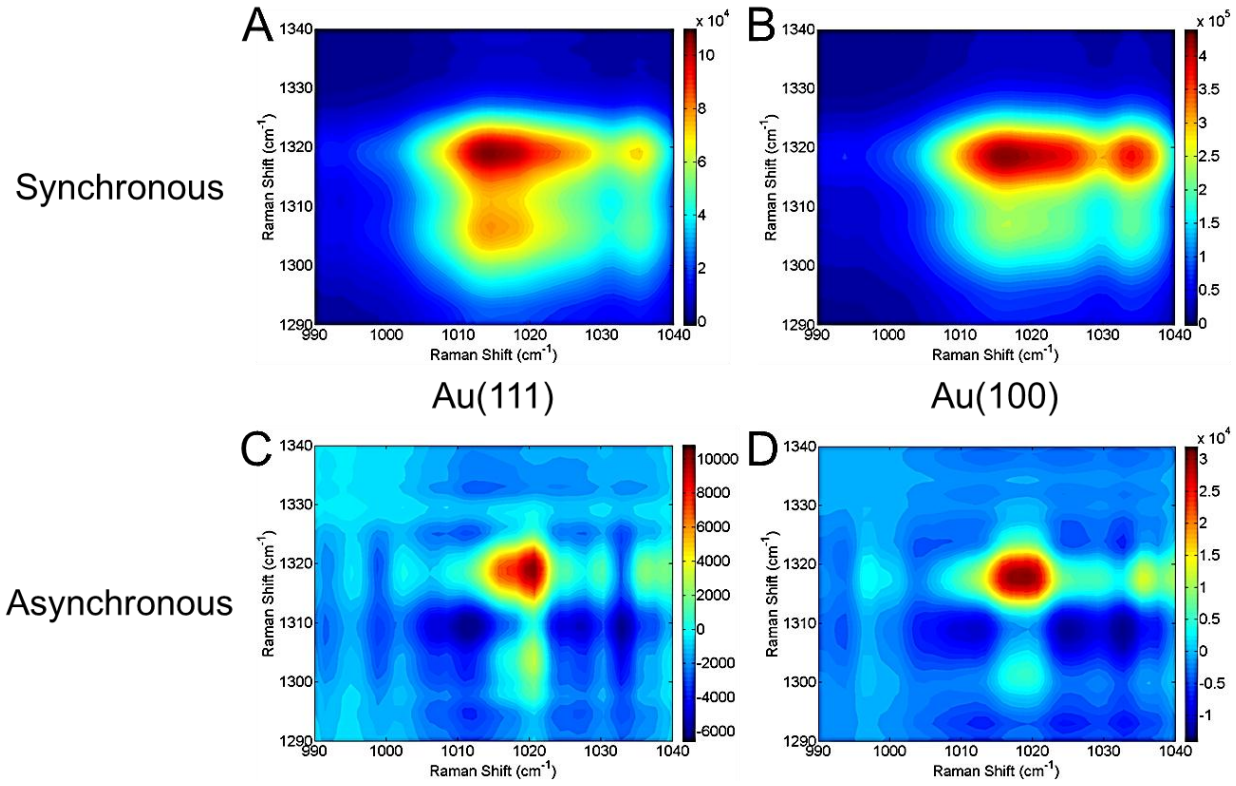

Figure 4.12: 2DCOS of 2,2'-bipyridine adsorbed on Au(111) and Au(100) in the potential range of 0.40 V to 1.0 V during anodic polarization

Chapter 5. Nitrate Reduction Pathways on Cu Single Crystal Surfaces: Effect of Oxide and Cl^-

Reproduced with permission from Journal of the American Chemical Society, submitted for publication. Unpublished work copyright 2012 American Chemical Society. Stefano P. Boulos conducted the synthesis of SiO_2 coated Au nanoparticles.

Introduction

Nitrate contamination of groundwater poses serious health risks at high levels of exposure including methemoglobinemia (blue-baby syndrome) and increased incidence of certain gastrointestinal cancers.[165-167] This contamination is mostly the byproduct of agricultural runoff from fertilizers and animal waste.[167-169] Remediation of nitrate in nuclear waste is also a critical issue for the nuclear industry.[170] Additionally, nitrate is used as a starting material to produce useful chemicals such as ammonia, hydroxylamine, hydrazine, and azides.[171] Thus, effective methods and materials to reduce nitrate is of considerable interest. Electroreduction is considered ideal as a method to reduce nitrate in water because reduction products can be tuned by altering pH, concentration, electrode material, and applied potential.[37, 166, 172] Many metal surfaces have been investigated, with Cu representing one of the most active nitrate electrocatalysts available.[34, 173]

On copper surfaces in acidic media, nitrate reduction occurs through an eight electron reduction as shown in equation **1**.[80, 174]

$$NO_3^- + 8e^- + 10H^+ \rightarrow 3H_2O + NH_4^+ \qquad (\mathbf{1})$$

$$E^\circ = 0.68 \text{ V vs. Ag/AgCl}$$

Previous investigations observed intermediates to reaction **1**, particularly nitrite (NO_2^-)[80, 174] and gaseous nitric oxide (NO)[173] in aqueous acidic conditions. A full suite of intermediate reactions are considered for nitrate reduction to ammonia on Cu, similar to reactions studied on

Pt surfaces and Cu decorated Pt.[34, 37, 172, 175] The rate determining step on all surfaces is considered the initial two electron reduction of nitrate to nitrite as seen in equation **2**.[80, 171-172, 174]

$$NO_3^- + 2H^+ + 2e^- \rightarrow NO_2^- + H_2O \qquad (\mathbf{2})$$

Reduction of nitrite to nitric oxide through a one electron reduction has been demonstrated on Pt as in equation **3**.[171-172]

$$NO_2^- + 2H^+ + e^- \rightarrow NO + H_2O \qquad (\mathbf{3})$$

Adsorbed NO is then reduced to NH_3 comparatively fast according to equation **4**.[172]

$$NO + 5H^+ + 5e^- \rightarrow NH_3 + H_2O \qquad (\mathbf{4})$$

Nitric oxide reduction to ammonia can be further broken down into a three step sequence as demonstrated by equations **5** through **7**.

$$NO + H^+ + e^- \leftrightarrow HNO \qquad (\mathbf{5})$$

$$HNO + H^+ + e^- \rightarrow H_2NO \qquad (\mathbf{6})$$

$$H_2NO + 3H^+ + 3e^- \rightarrow NH_3 + H_2O \qquad (\mathbf{7})$$

Direct protonation of adsorbed NO results in an equilibrium between NO and HNO. This is followed by a rate determining step of the one electron reduction of HNO to H_2NO, followed by the rapid three electron reduction of H_2NO to NH_3.[171]

While the intermediate situation is well-described for Pt surfaces, there is not yet a full understanding regarding the nature of intermediates on Cu and how these intermediates influence the electroreduction activity.[37] We demonstrated previously that Cu(111) is more active for

nitrate reduction than Cu(100).[174] The origin of this differential reactivity is not yet clear, in part because it is not known whether the same intermediates occur on both Cu faces. On polycrystalline electrodes SERS data showed the presence of adsorbed nitrate and nitrite.[80] DFT calculations and STM observations suggest a two O atom binding mode to bridge sites of the Cu surface for nitrate and nitrite on both Cu(111) and Cu(100). Dima et al. compared nitrate reduction on multiple transition metal surfaces and found using differential electrochemical mass spectrometry (DEMS) that NO desorbs from Cu into the solution because it exhibits a weaker binding energy than NO bound to Pt or other metals.[173] As a result, neither N_2O nor N_2 were observed as products of reduction on bulk Cu.

Shell-isolated nanoparticle enhanced Raman spectroscopy (SHINERS) expands the domain of adsorption and reaction processes that can be spectroscopically monitored at a surface.[41, 43-46, 65, 176] Typically, such studies using surface enhanced Raman spectroscopy (SERS) or tip-enhanced Raman spectroscopy (TERS) are limited by low detection sensitivity and substrate capable of surface enhancement at visible wavelengths (Cu, Ag, or Au).[131-134] Additionally, these techniques lack the surface specificity achieved by SHINERS because of electrochemical roughening or interference from deposited nanoparticles to achieve enhancement.[176] SHINERS eliminates these drawbacks by coating a Au nanoparticle, active for Raman enhancement, with a SiO_2 shell to prevent signal from analyte adsorbing to the Raman enhancing Au core.

In order to probe the reaction intermediates on the different faces of Cu to determine the origin of the differential reactivity observed and provide insight into the overall reaction mechanism, we here use SHINERS to interrogated nitrate reduction on Cu(100), Cu(111), and Cu(110). The higher sensitivity attendant the SHINERS technique means that different

intermediates may be observed. In particular, nitrite can associate with Cu in several different ways, as depicted in Figure 5.1. The Figure shows the N-bound nitro, O-bound nitrito, doubly O-bound chelating nitrito, N- and O-bound bridging nitro, N-bound nitroxyl, and N-bound nitrosyl (nitric oxide) modes of association. Nitric oxide and nitroxyl are considered to bind through lone pairs of the nitrogen atoms at bridge sites on Cu while nitrate may bind through two O atoms to bridge sites on the Cu surfaces.[80]

Results

Figure 5.2 displays the linear sweep voltammogram of nitrate reduction on Cu(100), Cu(111), and Cu(110) during cathodic polarization from 0 V to -0.8 V. Starting at 0 V, near the open circuit potential, very low current density is observed. As the system is subjected to more negative potentials, reductive current becomes apparent, most notably for Cu(111) and Cu(110). A small peak in the voltammogram from -0.05 V to -0.2 V is present for these surfaces, but not for Cu(100). This peak is attributed to NO_3^- reduction to NO_2^- through a 2 e^- reduction, as reported previously.[80] The onset for nitrate reduction on Cu(100) is around -0.2 V. We also noted the difference in voltammetric behavior between the Cu(100) and Cu(111) surfaces, as Cu(100) demonstrated a more negative potential onset reduction than Cu(111).[174] By -0.2 V, all three surfaces exhibit reductive current density, with Cu(111) and Cu(110) retaining slightly higher overall current densities than Cu(100) until -0.8 V.

Using the same potential range, 0 V to -0.8 V, SHINERS spectra were collected for each surface during cathodic polarization to investigate the nature of adsorbed intermediates during nitrate reduction. Table 5.1 compiles and identifies the peaks observed during nitrate reduction

on Cu(100), Cu(111), and Cu(110) as well as normal Raman spectra of $NaNO_{2(s)}$, $NaNO_{2(aq)}$, $NaNO_{3(s)}$, $NaNO_{3(aq)}$, and $HNO_{3(aq)}$ for comparison.

SHINERS spectra were also collected on Cu(100), Cu(111), and Cu(110) during cathodic polarization in a solution containing only 0.1 M $HClO_4$. Figure 5.10 displays these spectra and on all three surfaces; there are no discernible peaks related to nitrate or to Cu_2O.

Figure 5.3 presents SHINERS spectra obtained during nitrate reduction on Cu(100) from 0 mV (bottom) to -800 mV (top). At the positive potential extreme, the only peaks apparent result from the Cl-O stretch from perchlorate in solution at 931 cm^{-1} (peak **F**), the symmetric NO_3^- stretch at 1044 cm^{-1} (peak **G**) from solution nitrate, and symmetric (1350 cm^{-1}, peak **K**) and antisymmetric (1372 cm^{-1}, peak **L**) N-O stretches from the NO_2 moiety associated with adsorbed NO_3^-.

As the potential is scanned to more negative potentials, a suite of peaks associated with intermediates of nitrate reduction begin to appear by -300 mV. Peaks at 1200 cm^{-1} (peak **I**, N-O stretch) and 1372 cm^{-1} (peak **M**, N=O stretch) are associated with nitrito binding to the Cu surface due to the similarity of these energies with that found in complexes such as $K_4[Ni(NO_2)_4(ONO)_2]$.[177-178] Peaks at 1180 cm^{-1} (peak **H**, symmetric NO_2^- stretch) and 1281 cm^{-1} (peak **J**, antisymmetric NO_2^- stretch) are also assigned to NO_2^- in the chelating nitrito configuration from comparison to $Co(Ph_3PO)_2(NO_2)_2$ and $Ni(\alpha\text{-pic})_2(NO_2)_2$ complexes.[178-179] The N=O stretch of the bridging nitro conformation appears at 1434 cm^{-1} (peak **N**) and compares well to the ν(N=O) from bridging nitro groups in $[Ni(\beta\text{-pic})_2(NO_2)_2]_3 \bullet C_6H_6$.[178, 180] A final strong peak at 1528 cm^{-1} (peak **O**) is assigned as the N=O stretch of HNO by comparison with free HNO[181] and the N=O stretch in [Ru(HNO)(‘$py^{bu}S_4$’)][182]. There is also evidence of a low

intensity shoulder around 1535 cm^{-1} (peak **P**) growing in by -800 mV, assigned as a HNO stretching and bending combination mode. Assignment of peak **P** is based upon the presence of HNO bending and stretching combination mode at slightly higher frequency than N=O stretching in the SPARTAN calculated Raman spectrum of HNO shown in Figure 5.11. The nitroxyl peak (**O**) exhibits the highest relative intensity of this group on Cu(100). An additional NO_2^- bending mode appears at 801 cm^{-1} as peak **D** at -400 mV.

Figure 5.4 displays the SHINERS spectra obtained during nitrate reduction on Cu(111) from 0 mV (bottom) to -800 mV (top). At 0 mV, as on Cu(100), only peaks associated with perchlorate and nitrate are observed. Peak **F** appears at 931 cm^{-1}, Peak **G** at 1044 cm^{-1}, and peaks **K** and **L** at 1353 cm^{-1} and 1373 cm^{-1}, respectively. Additionally, low intensity peaks at 502 cm^{-1} (**A**) and 621 cm^{-1} (**B**), assigned as Cu_2O, indicate that the surface of the Cu(111) is partially oxidized.

Upon scanning to negative potentials, intermediates associated with nitrate reduction, including nitrite and nitroxyl, begin to appear. At -250 mV, peaks assigned to nitrito, chelating nitrito, bridging nitro, and nitroxyl begin to grow in as nitrate is reduced on the surface. Nitrito peaks grow in at 1202 cm^{-1} (**I**) and 1374 cm^{-1} (**M**). Chelating nitrito peaks grow in at 1181 cm^{-1} (**H**) and 1288 cm^{-1} (**J**). The bridging nitro orientation presents at 1435 cm^{-1} (**N**). Nitroxyl peak **O** first grows in at 1528 cm^{-1}, then by -450 mV, a second peak associated with nitroxyl bending (**P**) appears at 1534 cm^{-1} and continues to become more prominent until -800 mV. On Cu(111), peaks **I**, **O**, and **P** have the highest relative intensity of this set of peaks, indicating a preference for the adsorption of NO_2^- in the nitrito configuration as well as adsorption of nitroxyl. The NO_2^- bending mode (**D**) appears with a strong relative intensity by -300 mV at 800 cm^{-1}.

Figure 5.5 presents the SHINERS spectra obtained during nitrate reduction on Cu(110) from 0 mV (bottom) to -800 mV (top). Peak **F** appears at 931 cm^{-1}, Peak **G** at 1027 cm^{-1}, and peaks **K** and **L** at 1349 cm^{-1} and 1373 cm^{-1}, respectively. Additionally, moderate intensity peaks at 509 cm^{-1} (**A**) and 619 cm^{-1} (**B**), assigned as Cu_2O, indicate that the surface of the Cu(110) is partially oxidized.

Upon scanning to negative potentials, intermediates associated with nitrate reduction, including nitrite and nitroxyl, begin to appear. At -200 mV, peaks assigned to nitrito, chelating nitrito, bridging nitro, and nitroxyl begin to grow in as nitrate is reduced on the surface. Nitrito peaks grow in at 1208 cm^{-1} (**I**) and 1374 cm^{-1} (**M**). Chelating nitrito peaks grow in at 1183 cm^{-1} (**H**) and 1272 cm^{-1} (**J**). The bridging nitro orientation presents at 1431 cm^{-1} (**N**). Nitroxyl peak **O** first grows in at 1531 cm^{-1}, and peak P does not appear as on Cu(100) and Cu(111). On Cu(110), peaks **I** and **J** have the highest relative intensity of this set of peaks, indicating a preference for the adsorption of NO_2^- in the nitrito and chelating nitrito configuration. The NO_2^- bending mode (**D**) appears with a strong relative intensity by -250 mV at 801 cm^{-1}. An additional peak at 817 cm^{-1} (**E**) also appears as a shoulder of peak **D** by -250 mV. This is assigned as a second NO_2^- bending mode.

In order to examine the effect of surface adsorbates on the course of the nitrate reduction reaction, we added Cl^- to the reaction mixture. Cl^- is known to form overlayer arrays on Cu over a potential region starting at –300 mV vs. RHE (roughly -500 mV vs. Ag/AgCl) and through the anodic potential range.[183-185] Cl^- has also been demonstrated to poison the nitrate reduction process on copper and cause a negative nitrate reduction potential shift.[186-187] Linear sweep voltammetry from a solution containing 0.1 M $HClO_4$ + 0.05 M HNO_3 + 10 mM HCl is presented in Figure 5.6. In contrast to the Cl^- free situation in Figure 5.2, the onset for nitrate

reduction occurs at much more negative potentials as a result of Cl^- adsorption on the Cu surfaces. Cu(111) and Cu(110) display reduction beginning near -0.4 V. Interestingly, in the presence of Cl-, there is no initial onset of current (presumably associated with nitrate to nitrite reduction) before nitrate reduction occurs. Cu(100) exhibits reductive current density beginning around -0.5 V. As in the Cl^- free case, Cu(100) nitrate reduction onset is more negative than on Cu(111) and Cu(110). Overall current densities reach a maximum between -1.5 and -2 mA/cm^2 at -800 mV. This is significantly lower than the current densities of approximately 9 mA/cm^2 at -800 mV from Figure 2 for Cl^- free Cu surfaces.

Figure 5.7 shows SHINERS spectra of nitrate reduction on Cu(100), Cu(111), and Cu(110) in a solution containing 0.1 M $HClO_4$ + 0.05 M HNO_3 + 0.01 M HCl, in panels A, B, and C, respectively. As in Figures 5.2, 5.3, and 5.4, peaks associated with free perchlorate and free nitrate (**F** and **G**) are apparent around 930 cm^{-1} and 1040 cm^{-1} on each surface. In contrast to the Cl^- free systems, there is no evidence of adsorbed nitrite or nitroxyl species as the potential is scanned from 0 mV to -800 mV. Instead, on Cu(100) there are faint peaks associated with NH_3 and NH_4^+ that appear by -500 mV. Peaks at 765 cm^{-1} (**Q**, $\rho_r(NH_3)$ rocking), 1307 cm^{-1} and 1377 cm^{-1} (**S**, δ_s(HNH) deformation) and 1582 cm^{-1} (**V**, δ_a(HNH) of NH_3) are attributed to NH_3 formation at potentials more negative than -500 mV. Cu(111) differs and only shows a faint product peak at 1479 cm^{-1} (peak **U**) associated with the $\nu(T_4)$ antisymmetric NH_2 deformation of NH_4^+.

Cu(110) exhibits much stronger peak formation as the potential is scanned in the cathodic direction, with similar frequencies to Cu(100). Peaks at **Q**, **S**, **T**, **U**, and **V** all indicate the formation of NH_3 and protonation to NH_4^+ near the surface. Peaks at **V** are particularly complicated as several vibrations overlap and do not allow full identification. In addition to the

δ_a(HNH) of NH_3, vibrations of δ(E) antisymmetric NH_2 def. of NH_4^+ also fall in the 1560 cm^{-1} to 1614 cm^{-1} range.

In order to provide more mechanistic detail in the nitrate reduction process, Tafel plots were constructed and are displayed in Figure 5.8. The data was collected from solutions containing 0.1 M $HClO_4$ + 1 mM HNO_3 for panel A, and 0.1 M $HClO_4$ + 1 mM HNO_3 + 0.01 M HCl for panel B. The Tafel plot obtained from the bare Cu surfaces exhibits a stepwise behavior, with at least four different Tafel regions. This behavior is reminiscent of that found during the oxygen reduction reaction on Pt, where two different Tafel slopes are observed; the potential regions associated with these different slopes is associated with different mechanisms on the Pt surface.[35] The stepwise behavior here likewise suggests the presence of a stepwise reduction process whereby nitrate is successively reduced in discrete reactions that are made more apparent by the logarithmic scale. For the Cl^- coated surfaces, there is a broad region from -0.1 V to -0.45 V where there is no significant reductive current. The NO_3^- reduction then turns on by -0.45 V for Cu(111) and Cu(110), and by -0.55 V for Cu(100), as also seen in the cyclic voltammetry in Figure 5.6. Tafel slopes for the initial reduction of nitrate on bare Cu surfaces are -190 mV/dec, -191 mV/dec, and -295 mV/dec for Cu(100), Cu(111), and Cu(110), respectively. The corresponding values are -50 mV/dec on Cu(100), -83 mV/dec on Cu(111), and -102 mV/dec on Cu(110) on the Cl^- coated surfaces.

Density Functional Theory (DFT) calculations were performed to determine the adsorption energies of NO_2^- and NO_3^- to Cu(100), Cu(111), Cu(110), Cu_2O(100), Cu_2O(111), and Cu_2O(110). The adsorption energies are displayed in Table 5.3 for comparison. Adsorption energies for NO_3^- and NO_2^- adsorption have previously been reported by us on Cu(111) and Cu(100).[80] The results reported here closely follow those calculations. NO_2^- adsorption energies

were determined on each surface in both the nitrito and chelating nitrito configurations on Cu(100), Cu(111), and Cu(110). For both conformations, as well as for nitrate, the adsorption energy of nitrite decreases in the sequence Cu(110) > Cu(100) > Cu(111).

Adsorption energies of nitrate and nitrite on Cu_2O(100), Cu_2O(111), and Cu_2O(110) differ from the trend from the Cu surfaces. The oxide surfaces are indexed to the corresponding Cu surfaces during growth, making such comparisons relevant.[188] In the case of both nitrate and nitrite, the adsorption energies follow the trend of Cu_2O(111) > Cu_2O(110) > Cu_2O(100). Figure 9 presents a picture of the orientation of nitrate and nitrite on each oxidized surface. In each case, the adsorbing molecules orient themselves to most effectively bind O atoms to exposed Cu atoms on the surface. Qualitatively, the Cu_2O(100) surface has Cu atoms that are less accessible to nitrate and nitrite O atoms than are either Cu_2O(111) or Cu_2O(110). The oxide surfaces shown here are consistent with those suggested by Besenbacher for oxidized single crystal Cu surfaces.[189]

Discussion

The results presented in this work deliver a new level of detail concerning the reduction of nitrate in acidic conditions on Cu(100), Cu(111), and Cu(110). The work suggests that there are a number of different intermediate species occurring during nitrate reduction on these surfaces. Additionally, the work provides insight into the origin of the differential reactivity observed between Cu(100) and the other two low Miller index faces of Cu. Finally, this work provides insight into other catalysts exhibiting nitrate reduction activity.

Reaction Intermediates on Bare Cu Surfaces

The higher signal to noise available with the SHINERS technique and the ability to perform this technique on single crystal surfaces provides an opportunity to fully inventory intermediates attending the electroreduction of NO_3^- on Cu surfaces. The nitrate to nitrite process is well understood to be catalyzed by copper, thus making it a good candidate for overall nitrate reduction.[173, 175, 186, 190]

On the basis of STM images and calculations, we suggested previously that nitrate and nitrite preferentially adsorb in a chelating configuration through 2 oxygen and 2 copper atoms.[80] The data here, however, suggest that the intermediate situation is substantially more involved as there are indications of adsorption of nitrite through the singly bound nitrito, bridging nitro, chelating nitrito, and nitroxyl conformations. In particular, SHINERS spectra shown in Figures 5.3, 5.4, and 5.5 provide extensive detail regarding the nature of the intermediates on the low Miller index Cu surfaces. Peaks **H** and **J** are assigned as the chelating nitrito configuration, peaks **I** and **M** as the singly bound nitrito configuration, peak **N** as the bridging nitro configuration, and peaks **O** and **P** as the nitroxyl molecule. This observation may provide some rational for the dispersion of products seen during nitrate reduction on Cu[37], which generally results in formation of NO and NH_3. For example, a DEMS study [173] shows evolution of nitric oxide from an acidic solution from a Cu surface as a byproduct and Pletcher demonstrated NH_3 production in solution electrochemically[186], while other electrode surfaces like Pd or Pt can yield N_2O, NH_2OH and N_2.[34] We suggest that the presence of these intermediates and adsorption to the surface may lead to different products and suggest the origin of the multiple pathways for nitrate reduction on Cu.

The relative intensities of peaks related to the configurations of intermediates differed between the surfaces. From Figure 5.3, peaks **H**, **J**, **I**, and **M** as well as peak **D**, associated with

nitrite configurations, all feature lower relative intensity than the same sets of peaks from Figures 5.4 and 5.5 for Cu(111) and Cu(110). This could be explained by a lower density of nitrite on the Cu(100) surface, (vide infra). We note that the Cu(100) surface is less active for nitrate reduction relative to the other two faces.

Peak **O** from nitroxyl grows strongly on the Cu(100) and Cu(111) surfaces. Additionally, as potential is scanned to more negative potentials, peak **P** from the HNO bending and stretching combination mode begins to appear, and is rather prominent for the Cu(111) surface in particular. An additional difference between the reaction intermediates between the surfaces is that a second NO_2^- bending mode appears with peak **E** only on Cu(110). We speculate that this second bending mode is visible because of a higher density of NO_2^- on Cu(110), as evidenced by the high relative intensities of both the nitrito and chelating nitrito vibrations in Figure 5.5. It is not clear that these interesting observations directly affect the reduction activity, but simply show slightly different configurations that are favored on each unique face.

Reaction Intermediates in the Presence of Cl^-

From the spectra in Figure 5.7, there are also unique molecules and configurations generated in the presence of Cl^-. All three surfaces exhibit at least some peaks attributed to NH_3 or NH_4^+. In particular, Cu(110) reveals a suite of strong peaks attributed to both species. We propose that the reduction yields NH_3 as a product that is loosely bound to the surface in the presence of a protecting layer of Cl^-. Protonation and coordination with the Cl^- then leads to a surface bound adduct of NH_4Cl that is detected primarily on the Cu(110) surface, but whose presence cannot be excluded on the Cu(100) or Cu(111) surfaces. No oxygenated species are evolved on a Cl^- protected surface, likely because these species can't be effectively stabilized by

the electrode in the presence of Cl^-. STM investigations have revealed that bare Cu surfaces can only be imaged beyond the potential of Cl^- desorption (-500 mV vs. Ag/AgCl).[183, 185] Because nitrate is not stabilized by the surface, the reduction does not occur until more negative potentials relative to the case where nitrate and nitrite reduction are facilitated by adsorption to the Cu surface and interaction with surface Cu_2O that is present on Cu surfaces near the anodic potential extreme.

Origin of Differential Surface Reactivity

Among the most interesting results presented here is the fact that nitrate reduction on Cu(100) occurs at more negative potentials compared to Cu(111) and Cu(110). This trend is observed in the electrochemistry[174] and in SHINERS spectra where peaks associated with adsorbed nitrite and nitroxyl begin to grow in on Cu(111) and Cu(110) at potentials more positive than on Cu(100). The work function for Cu(100) is 4.59 eV which is in between and not that different from the work function for Cu(111) (4.94 eV) or Cu(110) (4.48 eV).[191] Thus work function (and hence pzc) differences between the three faces likely is not the origin of the differential reactivity.

The origin of this differential reactivity is also not immediately obvious from DFT calculations of the energetics of NO_3^- and NO_2^- adsorption to bare Cu surfaces. Specifically, Table 5.3 shows that both the reactant and product, nitrate and nitrite, bind most strongly to Cu(110), then to Cu(100) and finally most weakly to Cu(111). Models of reaction rate dependence on surface association strength, invoking the principle of Sabatier, suggest that intermediate strength association of both reactant and product to a surface should yield the highest rate.[192] However, exactly the opposite trend is observed here, where Cu(110) and

Cu(111) are more active than Cu(100) toward nitrate reduction. This experimental trend also cannot be reconciled with the nearly identical reactivities of Cu(110) and Cu(111), which exhibit different energies of nitrate and nitrite adsorption. Duca[175] and Dima[173] have previously shown the importance of the Sabatier principle in regards to nitrate reduction on Cu by demonstrating a tendency for an NO byproduct to form during the reduction process because of weak association of NO with the metal. Because of this, there is also a conspicuous absence of N_2O and its reduction product N_2, which ordinarily appears during the reduction process on other metals.

There are two possible ways to reconcile the observed trend with the calculation. First, it is possible that the nitrate reduction event is more complicated than indicated here, and perhaps involves species different from the nitrate and nitrite used in the calculation. In particular, the experimental observation of different nitrite orientations and coordination geometries suggests that these must all be considered. However, as shown in Table 5.3, different nitrate and nitrite geometries follow the same calculated trend described above. This calculation, coupled with the experimental observation of both nitrate and nitrite on the surface, suggests that these are the correct species to be used here. Thus, the adsorption energies of nitrate and nitrite to bare Cu, and by extension the relative ability of the surface to stabilize these ions, do not determine the observed difference in reduction activity.

The second possibility to reconcile calculation and experiment is that a bare Cu surface might not be the correct site of reduction activity. We note in particular the presence of features in the SHINERS indicating the formation of Cu_2O arising as a consequence of nitrate exposure to the Cu surface, even in strong acid, features that were suggested in AFM studies of this interface.[174] Thus, we consider the relative association energies of nitrate and nitrite with Cu_2O grown on each of the three Cu faces considered here. Table 5.3 shows that both nitrate and

nitrite are significantly more stabilized on $Cu_2O(111)$ and $Cu_2O(110)$ relative to the same molecules on $Cu_2O(100)$. The increased stabilization is likely the reason for the increased activity on (110) and (111) relative to (100).

The association between nitrate reduction activity and the presence special surface features, including oxides, at the reactive interface is well established. For example, hydrided Ge adsorbed on Pt or Pd increase the nitrate reduction activity and improve selectivity toward hydroxylamine by inhibiting adsorption of poisoning anions.[193] Sn coated surfaces have been shown to increase activity on Pt by providing a favorable site for binding O from NO_3^-, resulting in partial oxidation of the Sn.[194] In has also been demonstrated as a promoter on Pd.[195] While the association of nitrate (or nitrite) with each of these complex interfaces is not yet clear, the work here suggests an important role for oxide and oxophilic surfaces for facilitating nitrate reduction.

We next consider the rate of formation of the Cu_2O active surface. It is known that the corresponding Cu_2O oxide grows epitaxially on the underlying Cu surface for each of the three faces considered here.[188-189] However, oxidation of Cu(110) to form regions of Cu_2O occurs at a faster rate than on Cu(100) because higher surface energy leads the Cu(110) surface to be less stable; an additional factor is that the close packed nature of Cu(100) relative to Cu(110) allows less O diffusion into the metal and encourages more Cu_2O island growth.[188] Cu(111) oxidizes by a more layer by layer deposition because it serves as a perfect template for oxide layer formation, which allows for a faster rate of Cu_2O island nucleation than on either Cu(100) or Cu(110)[37].[188] Thus, the different susceptibilities of the surfaces to oxidation differentiate their activity toward autocatalytic reduction of NO_3^- to NO_2^-, leading to the difference in potential onset of reductive current observed in Figure 5.2. We showed previously that oxide like features

were present on Cu(111) in the presence of nitrate, but that these features were largely absent on Cu(100).[174]

Similar formation in aqueous systems of thin Cu_2O layers on Cu(100)[62], Cu(111)[196], and Cu(110)[197] has been demonstrated, even at potentials and pH not amenable to bulk Cu_2O formation.[196] Given the tendency of Cu(110) and Cu(111) to oxidize more readily than Cu(100), we suggest that another origin of the differential reactivity observed relates to the rate of oxide formation on these surfaces upon exposure to nitrate. Thus, we propose that an oxygen atom from the nitrate is transferred to these particular copper surfaces, resulting in an autocatalytic reduction to nitrite by the equations below.

$$NO_3^- + Cu(111) \rightarrow NO_2^- + Cu_2O(111) \qquad (\mathbf{8})$$

$$NO_3^- + Cu(110) \rightarrow NO_2^- + Cu_2O(110) \qquad (\mathbf{9})$$

$$NO_3^- + Cu(100) \rightarrow NR \qquad (\mathbf{10})$$

The Cu_2O surface then forms the catalytically active site. SHINERS spectra from Figures 5.3, 5.4, and 5.5 bolster this argument by demonstrating no noticeable Cu_2O formation on Cu(100) and strong oxidation on Cu(110) with Cu_2O vibrations present at 509 cm^{-1} and 619 cm^{-1}. The Cu(111) case was spectroscopically less conclusive, though evidence of low intensity Cu_2O vibrations is seen at 502 cm^{-1} and 621 cm^{-1}.

Poisoning the Cu surface with adsorbed Cl^- leads to significant changes to nitrate reduction activity. First, the potentials for nitrate reduction in Figure 5.6 occur some 300 mV more negative relative to that absent halide. Additionally, the current density for the reduction of nitrate is significantly reduced at the negative potential extreme. Second, species seen in the

SHINERS during nitrate reduction from the Cl^- decorated surface are different from those seen absent the halide. In particular, peaks observed in Figure 5.7 do not match those of any known NO_x or other partially oxygenated nitrate reduction species. There is no observation of Cu_2O, adsorbed nitrate, nitrite, or nitroxyl groups in the SHINERS spectra on Cu(100), Cu(111), or Cu(110). Instead, peaks in Figure 5.7 are associated with NH_3 and NH_4^+ species, possibly coordinated through Cl^- to the Cu electrode surface. Cl^- is known to inhibit the formation of Cu_2O on Cu surfaces. Additionally, once Cl^- is desorbed from the copper surface around -500 mV[183, 185], Cu will not oxidize to Cu_2O at such negative polarization according the Pourbaix diagram.[198]

In the Cl^- free situation, Cu_2O can linger because the surface has access to nitrate, which autocatalyzes to form an oxide and adsorbed nitrite as the reaction proceeds. Eventually even this process breaks down, as is observed most prominently in Figure 5.5 of nitrate reduction on Cu(110) where peaks associated with Cu_2O largely disappear by -500 mV. We thus conclude nitrate reduction follows a direct formation pathway to yield NH_3 when the Cu is decorated with Cl^-, but at greater overpotentials because the surface is not available to be oxidized to facilitate the reaction. This observation supports the notion that an oxided surface is a key component to nitrate reduction catalysis. Cl^- effectively blocks the Cu surface and prevents the adsorption of NO_3^- on each surface and the autocatalytic reduction to nitrite on Cu(111) and Cu(110). Since the NO_3^- to NO_2^- reduction is the rate determining step, Cl^- blocking of the surface has a significant effect on the overall activity. The bare Cu(100) surface still experiences the lowest activity toward nitrate reduction because of its greater relative stability, meaning fewer Cu^+ ions will be present to catalyze the reduction.[199] The Cl^- layer on the Cu(100) may also be slightly more stable than on the (111) or (110) surfaces, resulting in delayed Cl^- desorption.

Further investigation of the reaction mechanism was performed by constructing Tafel plots of the nitrate reduction process in Cl^- free and Cl^- containing solutions, as displayed in Figure 5.8. Examining the Cl^- free situation in Figure 5.8A, we find the most striking feature to be the multiple steps to the reduction process, corresponding to the stepwise reduction of NO_3^- to NO_2^-, NO, HNO, and then NH_3. This behavior contrasts sharply with the Cl^- containing solution where there is no faradaic current passed until much more negative potentials on each surface. The onset at these more negative potentials is followed by a strong, one step reduction event very near the negative end of the potential window. The desorption of halide is associated with rapid reactivity leading directly to NH_3.

Conclusions

We show that the SHINERS technique provides insight into reactivity on different faces of Cu with and without the presence of Cl^-. Nitrate reduction proceeds via formation of different modes of association of nitrite to the electrode surface, particularly the nitrito and nitroxyl geometries. All three faces show similar intermediates, suggesting the same mechanism is operative on all of them. Absent Cl^-, nitrate reduction proceeds with concomitant surface oxidation, the rate of which controls subsequent reactivity and provides an explanation for the differential reactivity seen between Cu(100) and the other two low Miller index faces. The early onset of cathodic current density, along with earlier onset of SHINERS peaks associated with nitrite, on Cu(111) and Cu(110) compared to Cu(100) are associated with the different rates of surface oxide formation and with the decreased stability of both reactants and products on Cu_2O(100) relative to the other two oxide faces. The importance of the oxidized Cu surface for nitrate reduction activity is also made apparent by the extra overpotential required for Cu surfaces protected by Cl^-. SHINERS observations indicate a unique reaction mechanism from

the Cl^- free situation, featuring direct reduction to NH_3. That the presence of Cu_2O modulates activity gives additional direction for the engineering of effective nitrate reduction catalysts.

Acknowledgements

We thank the National Science Foundation (NSF) for their generous support. We also recognize Dr. Catherine J. Murphy and Stefano Boulos for performing the synthesis of SiO_2 coated Au nanoparticles for the SHINERS experiments and for helpful discussions.

Tables

Table 5.1: Raman scattering peaks for nitrate and nitrite species.

	Raman Shift (cm^{-1})									
Peak	$NaNO_2$ (s)	$NaNO_2$ (aq)	$NaNO_3$ (s)	$NaNO_3$ (aq)	HNO_3 (aq)	Cu(100)	Cu(111)	Cu(110)	Assignment	Ref.
A							502	509	Cu_2O	80
B							621	619	Cu_2O	80
C			723	778	782					
D	826	814				801	800	801	NO_2^- bending	80, 200-202
E								817	NO_2^- bending	
F						931	931	931	ν(Cl-O)	
G			1066	1031 1047	1031 1047	1044	1044	1027	ν_s NO_3^- stretch	178, 203-208
H						1180	1181	1183	ν_s NO_2^-, chelating nitrito	178-179
I				1269	1291	1200	1202	1208	ν(N-O), nitrito orientation	177-178
J						1281	1288	1272	ν_a NO_2^-, chelating nitrito	178-179
K						1350	1353	1349	ν_s NO_2 of NO_3^-	80, 202, 209-210
L			1384	1408	1427	1372	1373	1373	ν_a NO_2 of NO_3^-	80, 200, 202, 210
M	1324	1326				1372	1374	1374	ν(N=O), nitrito orientation	177
N						1434	1435	1431	ν(N=O), bridging nitro	178
O						1528	1528	1531	ν(N=O), nitroxyl	181-182, 211
P							1534		HNO bend and stretching, nitroxyl	

*ν_s is symmetric stretch, ν_a is antisymmetric stretch

Table 5.2: Raman scattering peaks for ammonia and ammonium products of nitrate reduction in a solution containing Cl^-.

	Raman Shift (cm^{-1})				
Peak	Cu(100)	Cu(111)	Cu(110)	Assignment	Ref.
Q	765		763	$\rho_r(NH_3)$ rocking	[178]
F	933	931	931	ν(Cl-O)	
R	1018	1015	1013	$\nu_s(NO_3)$ adsorbed NO_3^-	[178, 203-208]
G	1047	1045	1045	$\nu_s(NO_3)$	[178, 203-208]
S	1307		1309	δ_s(HNH) deformation	[178]
T	1377		1374	δ_s(HNH) deformation	[178]
U	1481	1479	1480	$\nu(T_4)$ antisymmetric NH_2 def. of NH_4^+	[212-214]
V	1582		1560, 1591, 1614	δ_a(HNH) of NH_3 and δ(E) antisymmetric NH_2 def. of NH_4^+	[178, 212-214]

Table 5.3: Adsorption energies of nitrate, nitrito, and chelating nitrito configurations on Cu(100), Cu(111), Cu(110), Cu_2O(100), Cu_2O(111), and Cu_2O(110).

Surface Orientation	Adsorption Energy, E_{ad} (eV)†		
	Cu(100)	Cu(111)	Cu(110)
Nitrate	-2.69	-2.28	-2.80
Nitrito	-1.42	-1.21	-1.47
Chelating Nitrito	-1.97	-1.65	-2.12
	Cu_2O(100)	Cu_2O(111)	Cu_2O(110)
Nitrate	-0.24	-9.65	-4.22
Chelating Nitrito	-0.48	-9.08	-3.50

† $E_{ad} = E[NO_x/Cu(hkl)] - E[NO_x] - E[Cu(hkl)]$

Figures

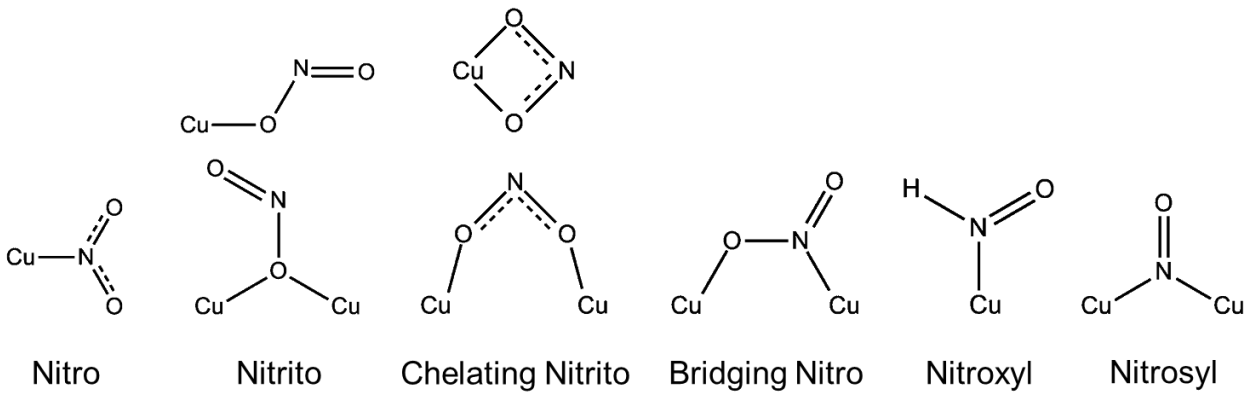

Figure 5.1: Conformations for the adsorption of NO_2^-, NO, and HNO onto a Cu surface

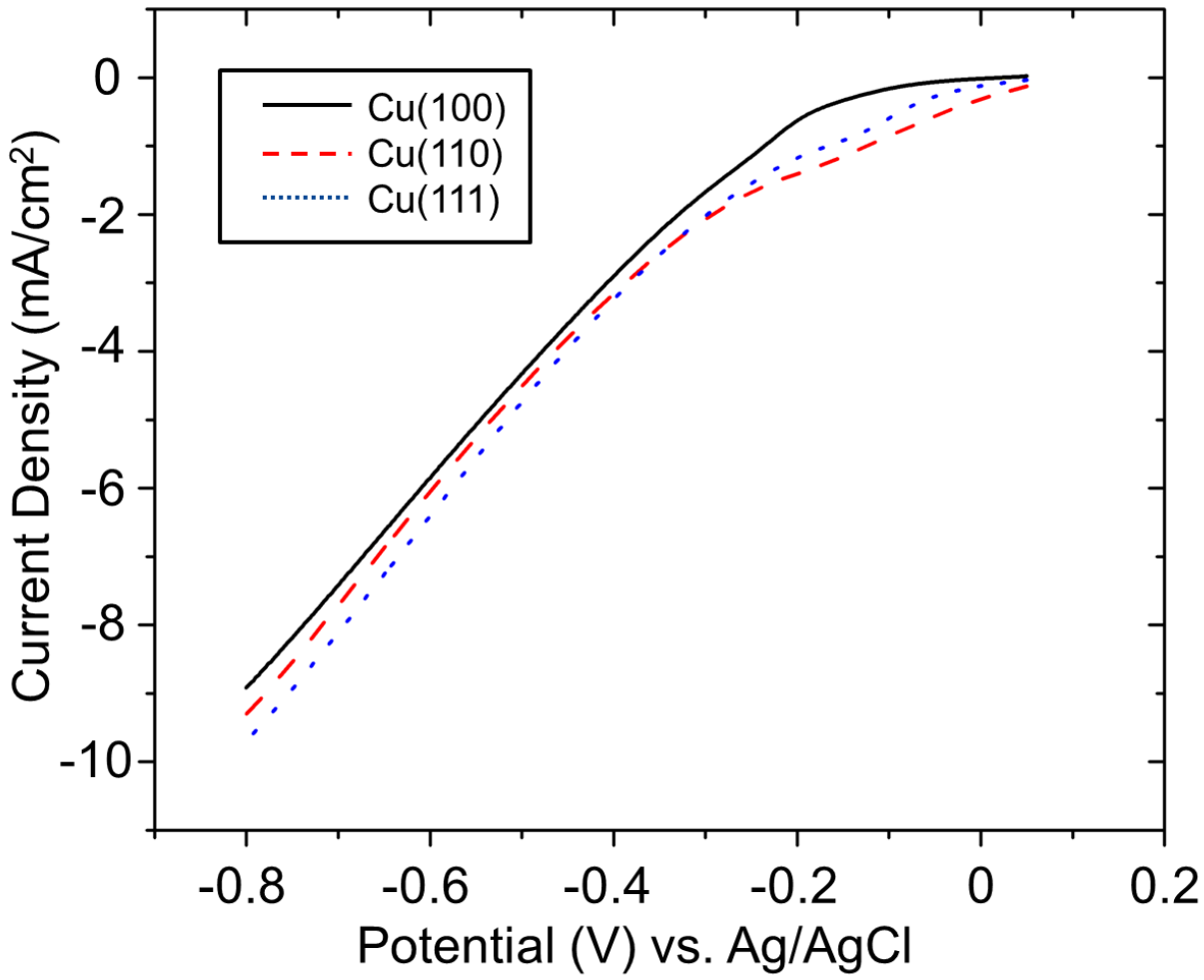

Figure 5.2: Linear sweep voltammetry collected from Cu(100), Cu(110), and Cu(111) in a solution containing 0.1 M $HClO_4$ + 0.05 M HNO_3 from 0 V to -0.8 V vs. Ag/AgCl

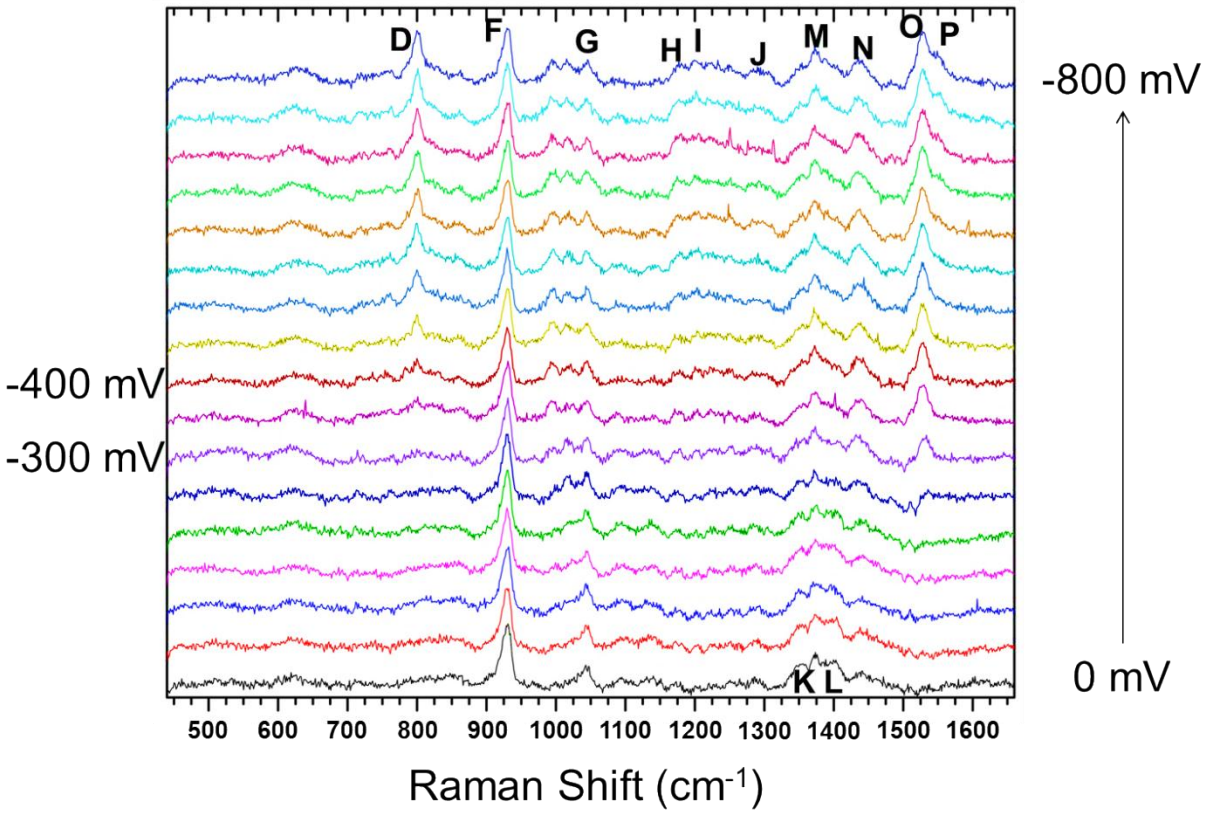

Figure 5.3: SHINERS obtained from a Cu(100) crystal in a solution containing 0.1 M $HClO_4$ + 0.05 M HNO_3 during cathodic polarization from 0 mV to -800 mV vs. Ag/AgCl

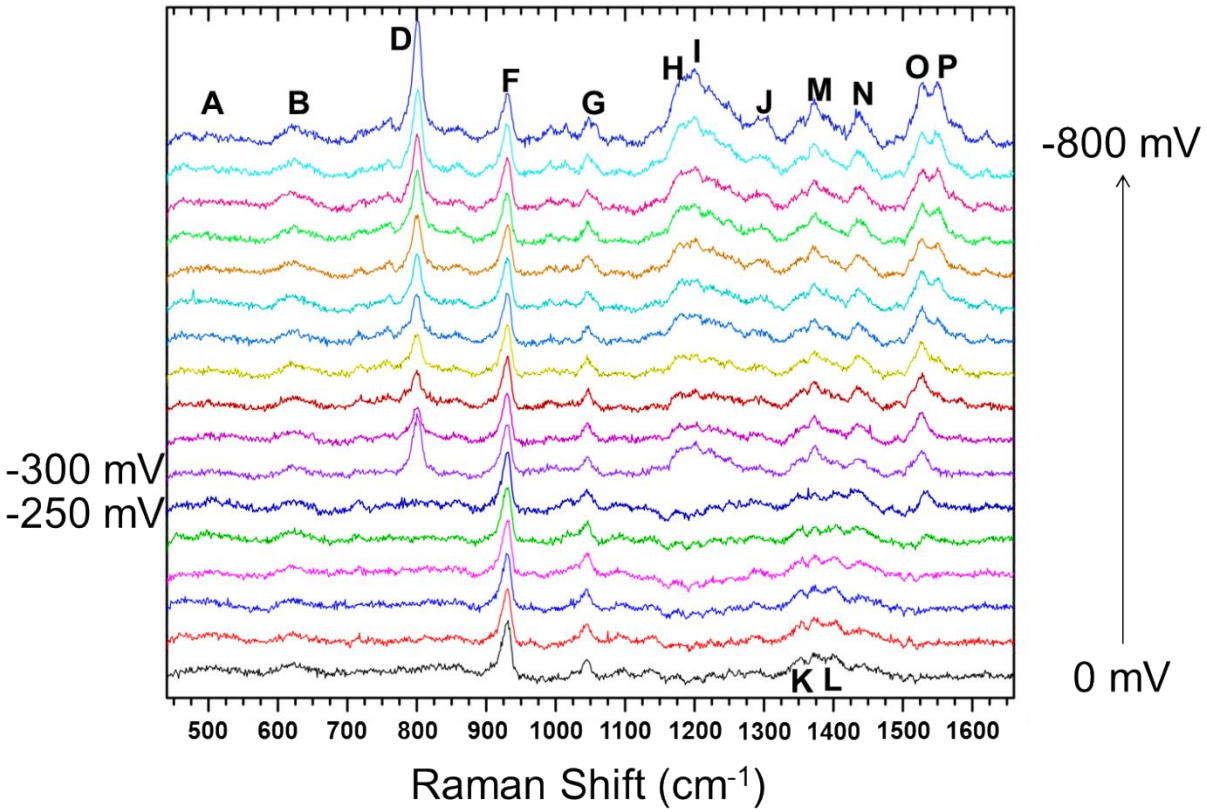

Figure 5.4: SHINERS obtained from a Cu(111) crystal in a solution containing 0.1 M $HClO_4$ + 0.05 M HNO_3 during cathodic polarization from 0 mV to -800 mV vs. Ag/AgCl

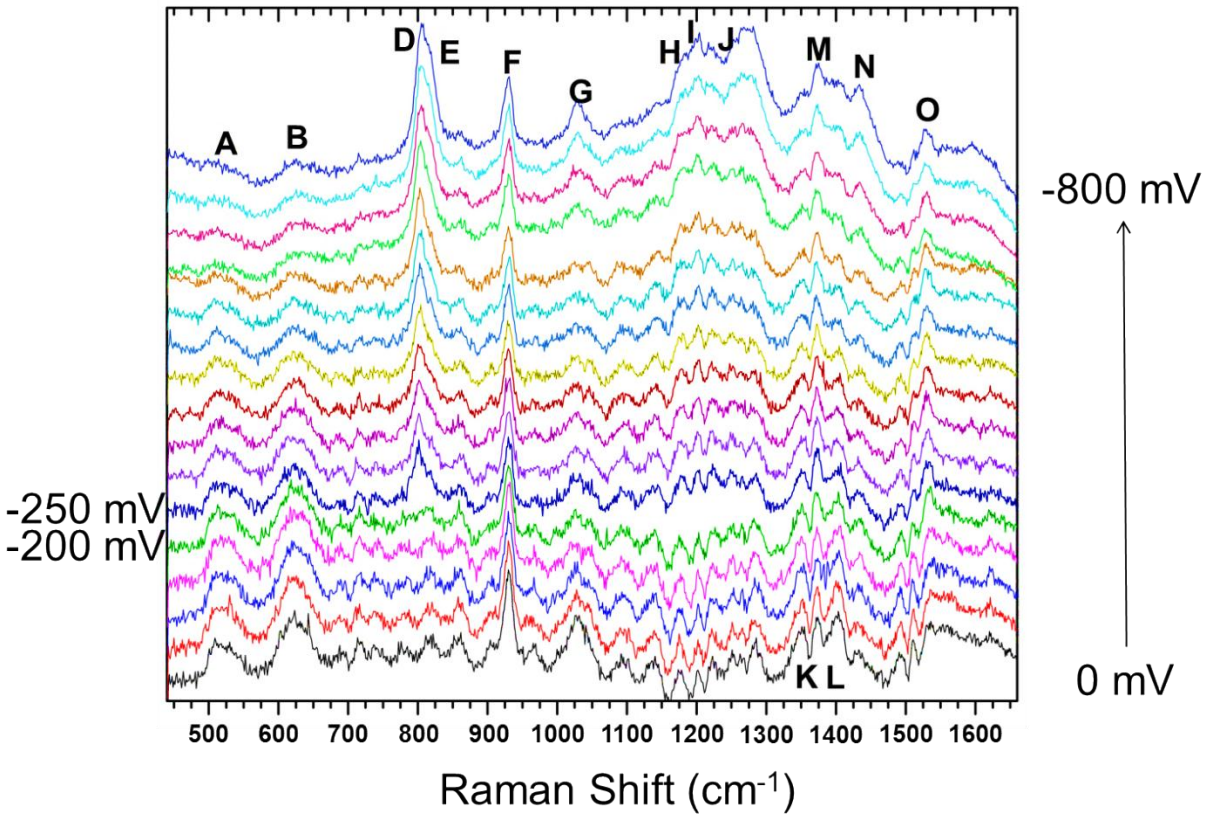

Figure 5.5: SHINERS obtained from a Cu(110) crystal in a solution containing 0.1 M $HClO_4$ + 0.05 M HNO_3 during cathodic polarization from 0 mV to -800 mV vs. Ag/AgCl

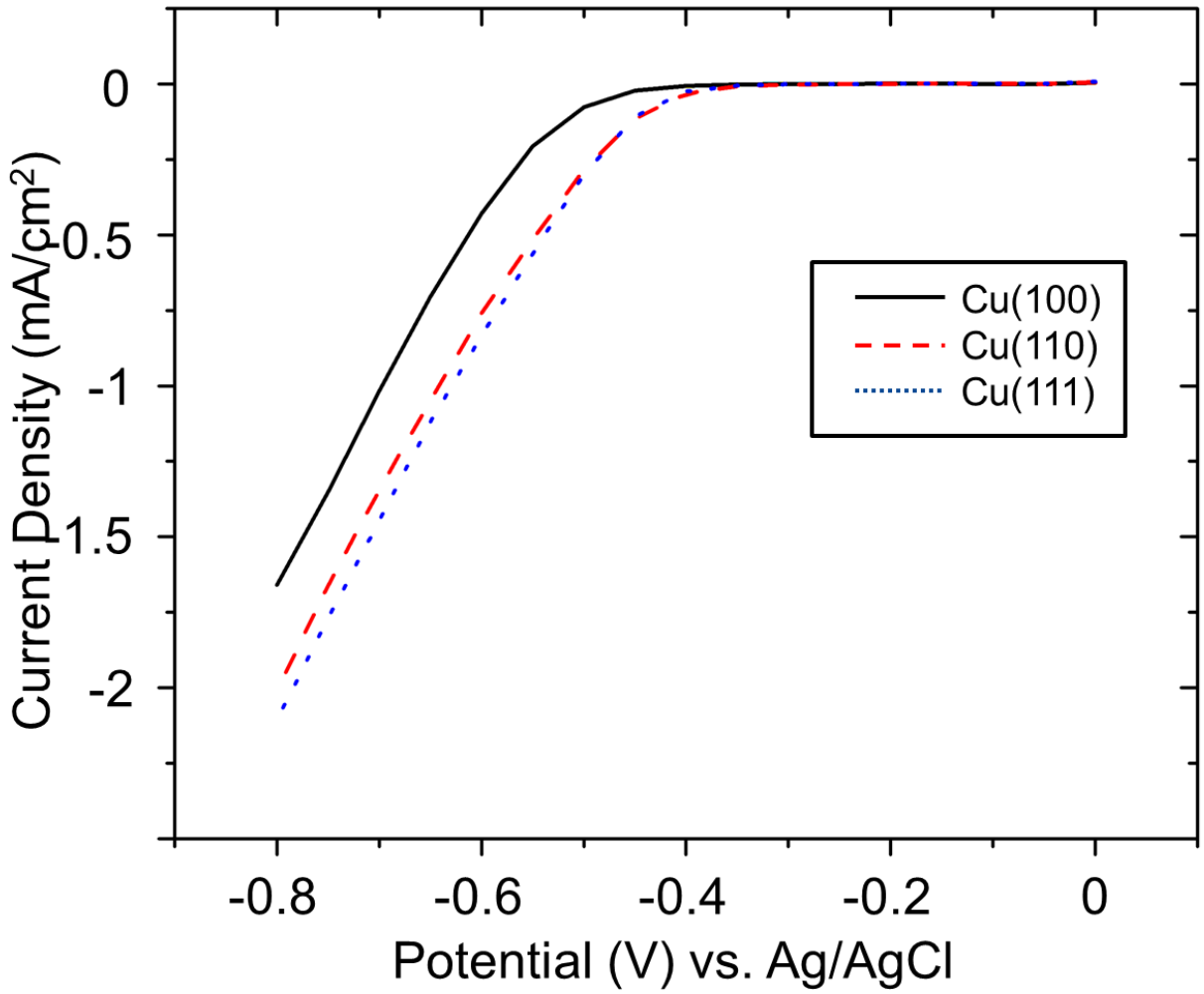

Figure 5.6: Linear sweep voltammetry collected from Cu(100), Cu(110), and Cu(111) in a solution containing 0.1 M $HClO_4$ + 0.05 M HNO_3 + 10 mM HCl from 0 V to -0.8 V vs. Ag/AgCl

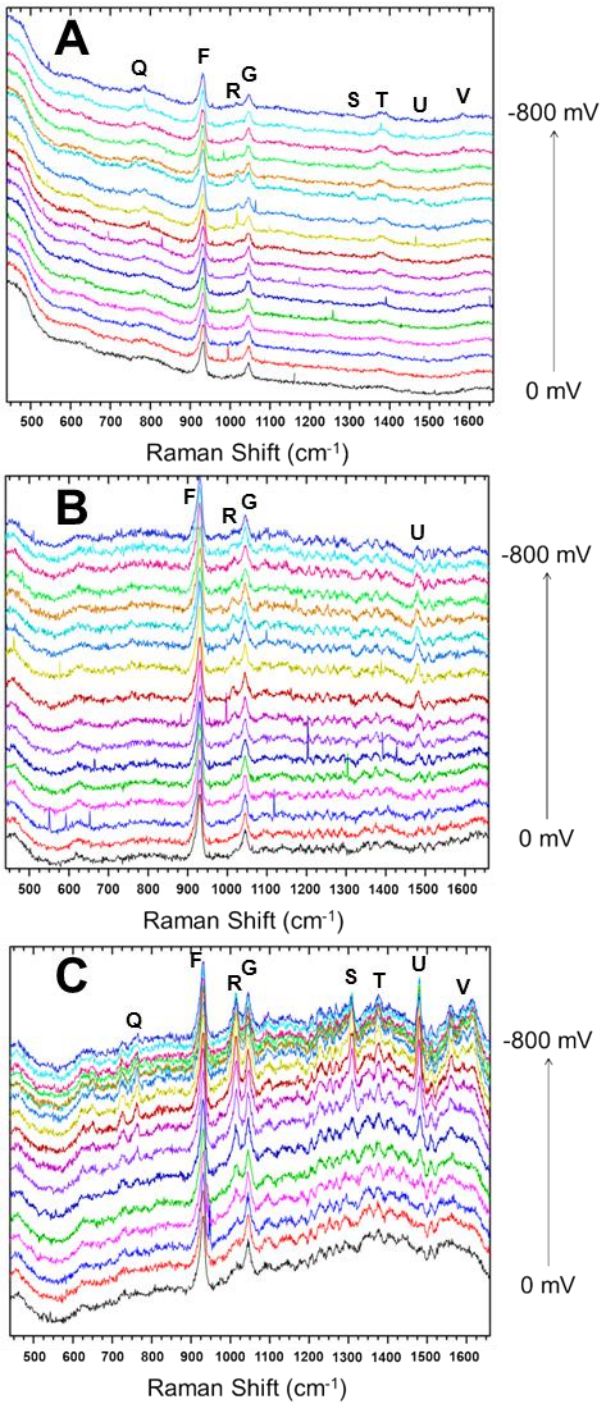

Figure 5.7: SHINERS obtained from (A) Cu(100), (B) Cu(111), and (C) Cu(110) in a solution containing 0.1 M $HClO_4$ + 0.05 M HNO_3 + 10 mM HCl during cathodic polarization from 0 mV to -800 mV vs. Ag/AgCl.

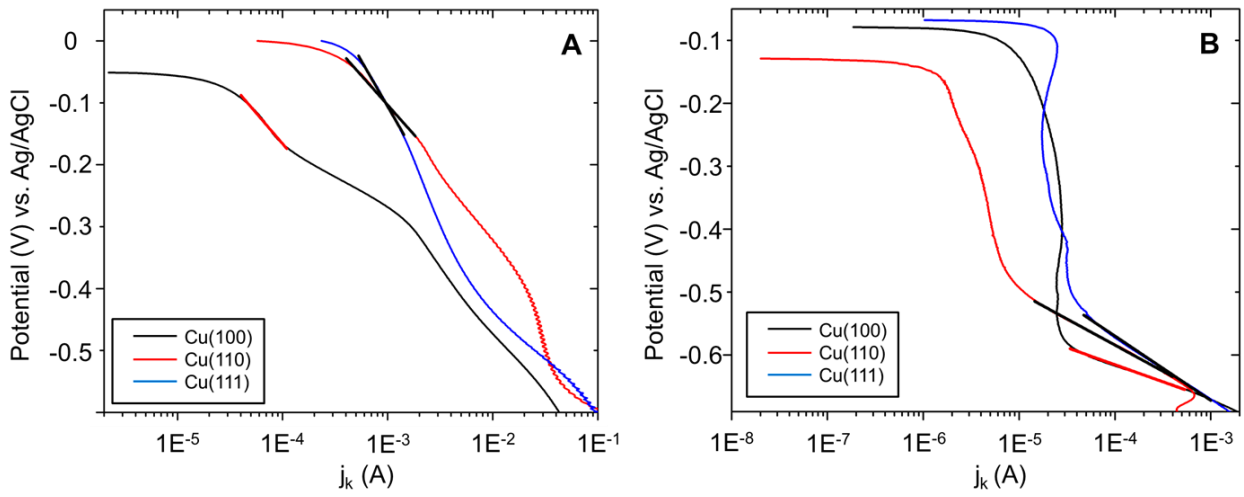

Figure 5.8: Tafel plots for Cu(100), Cu(111), and Cu(110) in solutions containing (A) 0.1 M $HClO_4$ + 1 mM HNO_3 and (B) 0.1 M $HClO_4$ + 1 mM HNO_3 + 0.01 M HCl.

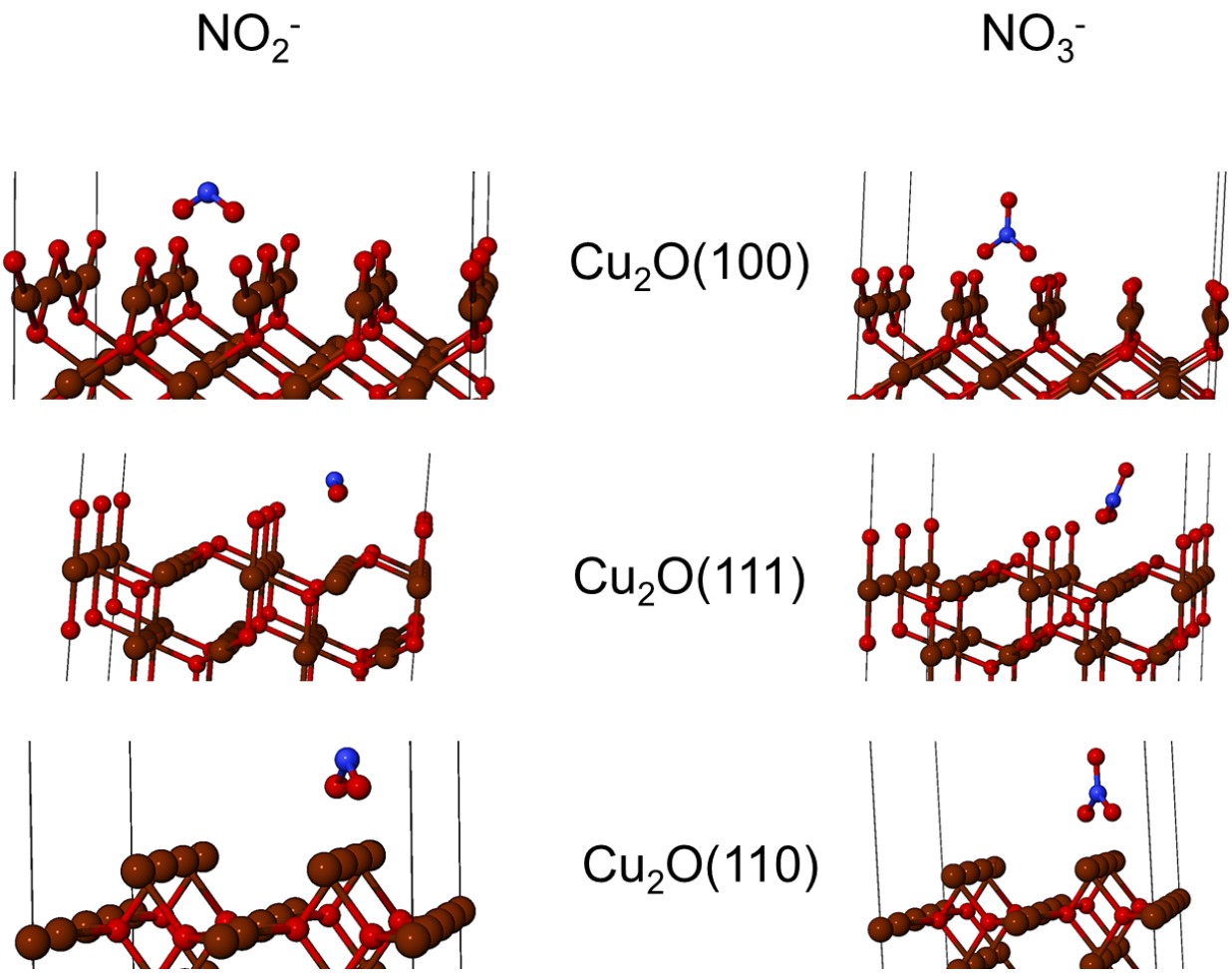

Figure 5.9: Minimized structure of nitrate and nitrite on $Cu_2O(hkl)$ surfaces from VASP calculations.

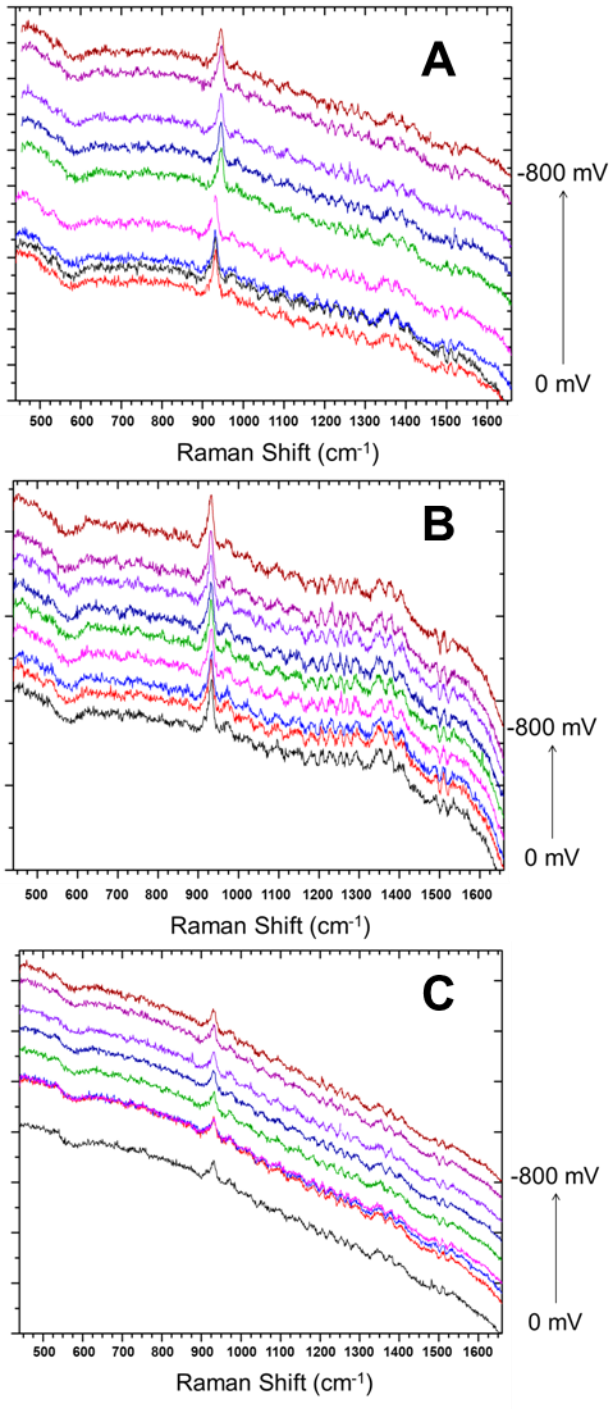

Figure 5.10: SHINERS obtained from (A) Cu(100), (B) Cu(111), and (C) Cu(110) in a solution containing 0.1 M $HClO_4$ during cathodic polarization from 0 mV to -800 mV vs. Ag/AgCl

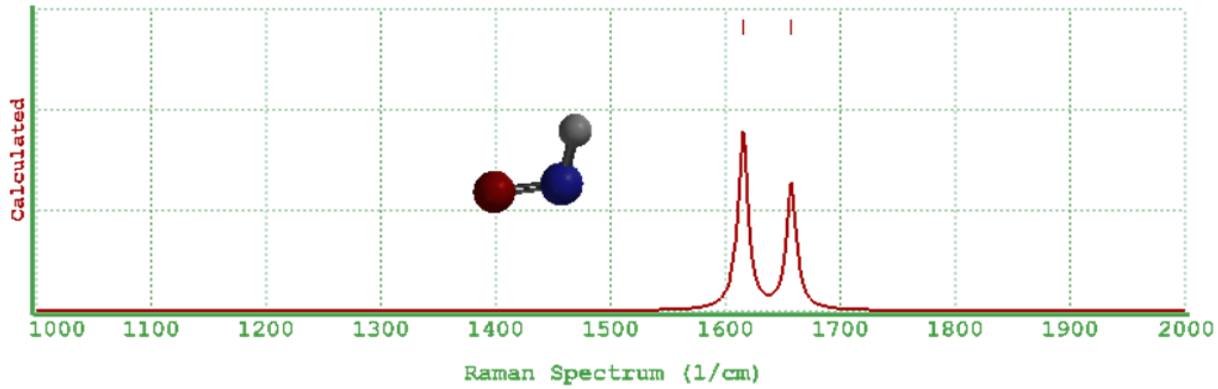

Figure 5.11: SPARTAN simulation of the Raman spectrum of free HNO in water.

Chapter 6. Variable Temperature STM and Computational Studies Examining Water and Potassium Adsorption on Au(100)

Reproduced with permission from Leung, T.Y.B., Butcher Jr., D.P., Gewirth, A.A. J. Phys. Chem. C ***2012****, 116, 555-562. Becky Leung conducted the initial VT-STM experiments and the analysis of the micrographs. Dennis P. Butcher Jr. performed supporting VASP calculations and subsequent analysis and reconciliation with experimental observations.*

Introduction

Hydration of potassium ions is of paramount importance in various disciplines. Recent studies suggested that the interaction between aromatic residue and hydrated K^+ governs the selectivity of potassium channels in biological membranes.[215-217] Hydration of K^+ and other simple cations governs the geochemical cycling of these vital metal nutrients.[218-219] The interaction of K^+ with surfaces and solvents may also be relevant to developing battery technologies.

Sass introduced the idea of double layer simulation by adsorbing ions and solvent molecules on a clean metal surface in ultra-high vacuum (UHV).[220] The UHV experiment has as an advantage the ability to control the identity and quantity of species on the surface in a systematic manner. In this way, it is possible to create an artificial double layer of known type. Studies of the association of water with metals are itself a vast enterprise which has seen substantial reviews.[221-223] Ordering has been observed in H_2O adsorbed on hexagonal faces of metals such as Pt at low temperatures where the characteristic 'bilayer' structure forms.[223-225]

Measurements examining these artificial double layers typically utilize vibrational spectroscopies, temperature programmed desorption (TPD), low energy electron diffraction (LEED), or other UHV-based techniques to interrogate the solvent associated with surface and cation or anion.[226-228] With regard to K ion solvation, these studies have shown that addition

water to small amounts (ca. 0.05 ML) of K adsorbed on surfaces leads to water reorientation around the cation.[229] This water-induced reorientation is also observed for other alkali cations, such as Na^+ on Ru(0001). Research suggests that the tilt of the plane of the water molecule increases with the strength of the alkali-surface dipole (i.e., in the order Na < K < Cs). These authors also found that the tilt for a particular alkali is stronger for substrates with a weaker water-metal interaction. Alternatively, large amounts of K cause H_2O dissociation, and lead to the formation of solvated KOH and other hydride species on the surface[230-232] through the reactions

$$K + H_2O \rightarrow KOH + \tfrac{1}{2}H_2$$

$$K + H_2O \rightarrow K^+ + (H_2O)_n^-$$

Vibrational spectroscopic studies of the coadsorbtion of K and water at Pt[233], and graphite[234-235] surfaces indicates that KOH formation occurs after deposition of a critical coverage of K and features solvation of the hydroxide by additional water and K association with the surface. Unclear from these efforts is the structure adopted by the solvated hydroxide and water and the way in which water coadsorbtion restructures the surface.

As a first step in examining the interplay of solvent and cation at a metal surface, we examined the way in which solvent molecules alone like water[74] and dimethyl sulfoxide[236] interact with Au metal surfaces. On Au(111), dimethyl sulfoxide (DMSO) orders only at step edges, while no ordering of water was observed. On Au(100), DMSO was observed to order at low temperatures, but this is not the case for water. In solution, different cations exhibit different potential dependent degrees of water association.[33] In this paper we examine how water interacts with simple cations adsorbed on a metal surface. In particular, we present measurements of adsorption of water and potassium on Au(100) surfaces using variable temperature scanning

tunneling microscopy (STM). DFT calculations are used to explain some of the observed structures.

Results

Structure of Au (100) and K/Au(100)

Figure 6.1a is an STM image of a clean Au(100) surface in UHV exhibiting rows with a periodicity of 1.44 nm are along the nearest neighbor (NN) directions. This structure occurs as the Au(100) surface reconstructs into a cell of ca. (5 × 20), the driving force for which is to expose (111) facets which are at lower energy.[237-238] The atomic density is ca. 20-25% higher in this top layer, and along the <110> direction every fifth atomic row is bunched outward by ca. 0.1 nm. This gives rise to the characteristic row structures seen in Figure 6.1a.

After adsorption of *ca.* 0.25 ML of K, STM images reveal a structure different in several respects as shown in Figure 6.1b. First, the (5 × 20) reconstruction is completely lifted, leading to a featureless surface at the atomic scale. Second, the STM reveals the formation of a two-level system, a cross section profile through which along the arrow in Figure 6.1b is shown in Figure 6.1c. The upper level is above the lower level by the height of one gold atomic step (0.204 nm). Also, comparison of Figure 6.1a and 6.1b shows that the boundaries of the two levels are along the two reconstruction NN directions.

The adsorption of potassium on Au(100) has been well studied[75, 239-240] and the results reported here are identical with these earlier efforts. On the basis of STM and LEED results consistent to a (1 × 2) lattice, Barth, et al. proposed a model based on conservation of gold atoms.[75] In this model, the top hexagonal layer of Au(100) restructures into two layers upon the adsorption of potassium. In the first layer, gold atoms arrange as the bulk lattice with a Au atom

coverage of 1.0 ML. The remaining 0.5 ML of Au atoms arrange as a (1 × 2) missing-row structure on top of the first layer, and K atoms occupy the troughs of the missing-row structure. The model suggests that the (5 × 20) reconstruction is completely lifted by adsorption of 0.25 ML of K. Schroeder and coworkers showed that at low temperature formation of the (1×2) phase was inhibited, suggesting that a K-Au alloy might be present, particularly with higher (θ_K = 0.38) K dosages.[240] It is not clear why the (1×2) missing row structure is not imaged in previous work[75] or the present study -- even at 50 K (result not shown) -- but featureless images are typically interpreted in terms of surface atom fluxionality on the time scale of STM imaging. Indeed, Barth et al. observed 'frizzy' step edges at room temperature – features typically associated with adatom mobility.[241]

Addition of water; H_2O/K ratio is 2:1 Striped phase

In order to examine the interaction between K and H_2O, the K-modified Au(100) surface (θ_K = 0.25) was then cooled to 80 K and exposed to water. Figure 6.2a shows an image acquired after adsorption of ca. 0.5 ML of water, assuming the sticking coefficient of water is one. Like the K/Au(100) image shown in Figure 6.1b, this image retains the two level structure. However, instead of imaging an essentially featureless terrace region, the terraces of both levels now evince a series of stripe-like features. The stripes are oriented parallel and perpendicular to each other, and by comparison with images of the clean Au(100) surface are found to be arranged along the two orthogonal NN directions.

The stripes have a width that we define as the shortest distance from a minimum to the next minimum in cross-section profiles of the stripes. Figure 6.2b plots a cross-sectional profile along line B in Figure 6.2a, Figure 6.2c is a cross sectional view of a 'no-stripe' region denoted

by line C, and Figure 6.2d is a cross-sectional view perpendicular to a series of stripes marked by line D. Typically, the stripes exhibit periodicities of 1.4 to 1.6 nm upon examination of 10 images. The labyrinthine structure in Figure 6.2a features bright areas that we associate with material on the surface, and dark areas that are associated with bare Au. The width of the bright features, measured at half height on the stripes, ranges from ca. 0.7 nm to 1.1 nm. These measurements do not account for the possibly convoluting influence of the tip, and must be considered approximate.

The height of the stripes is found to be ca. 0.10 nm. Also, the cross-section profile shows that the difference in height between a stripe in the upper level and one in the lower level equals to 0.20 nm, which is same as one gold atomic step. This difference in height is identical to that found in the water-free two level system shown in Figure 6.1b.

The stripes do not decorate the entire terrace. The 'no-stripe' regions are at the border of the two-level system, as shown in the cross section in Figure 6.2c. They are elongated and are arranged along the NN directions. From Figure 6.2c, the width of one of the 'no-stripe' regions is found to be (1.22 ± 0.08) nm.

In order to gain insight into the labyrinthine stripe structure observed in Figure 6.2a, we performed DFT calculations examining the adsorption of KOH on a Au(100) surface. The labyrinthine structure observed suggests that the energy required to grow orthogonally to a row direction is similar to that required to continue along the row direction.

We first examined the interaction of two or more KOH molecules with each other and the Au surface. Both the (1×2) reconstructed and the unreconstructed Au(100) surfaces were examined, with qualitatively equivalent results; reported here are results for the (1×2)

reconstructed surface. Calculations were performed with 2 KOH molecules in parallel (Configuration 1), antiparallel (Configuration 2), and side-on (Configurations 3 and 4) conformations in close contact with the Au(100) surface. For DFT calculations, the adsorption energy is calculated by subtracting the energies of KOH molecules in the gas phase and a clean Au(100) slab from the total energy of the KOH/Au system.[242-243] Table 6.1 features the calculated adsorption energies of KOH on (1×2) reconstructed Au (100) as calculated by the general equation $E_{ads} = E_{KOH/Au} - E_{slab} - xE_{KOH}$, with x being the number of KOH adsorbed on the Au surface. The antiparallel Configuration 2 displays an adsorption energy of -2.10 eV and aligns itself into a stripe along the reconstructed surface as seen in Figure 6.3. The side-on Configurations 3 and 4 have adsorption energies of -2.90 eV and -2.54 eV, respectively, while the parallel Configuration 1 has an energy minimum of -2.65 eV. These configurations are displayed in Figure 6.6 and show no particular order or possible direction of propagation.

Further calculations were performed with 3 KOH molecules on the (1×2) reconstructed Au(100) surface to elucidate the way in which turns in the labyrinthine structure may arise; the associated energies are displayed in Table 6.1. In each configuration, 2 KOH molecules are arranged antiparallel and the third is brought into contact perpendicular to these two initial molecules to model a turn or corner as observed in Figure 6.2a. Configuration 5 has the third molecule approach in an electrostatically favored manner with K^+ approaching OH^- and OH^- approaching K^+, while configuration 6 is the opposite situation with K^+ approaching K^+ and OH^- approaching OH^-. Configuration 5 has an energy minimum of -2.89 eV while Configuration 6 has a minimum energy of -3.29 eV. Configurations 9 and 10 represent situations where the third KOH approaches one of the antiparallel KOH molecules side-on. Configuration 9 has the KOH approach with the K^+ closest to the nearby OH^-, while Configuration 10 has OH^- closest to this

same OH^-. The result is Configuration 9 has a lower energy minimum, -4.15 eV, than Configuration 10**,** -2.84 eV. Configurations 5 and 9 display alignment of KOH along the (1×2) reconstructed Au(100) directions and are displayed in Figure 6.3. Configurations 6 and 10 show no particular direction of propagation and are shown in Figure 6.7.

Images with a reduced H_2O/K ratio

In order to assess the role of water in developing the striped structure seen in Figure 6.2a, we constructed K/H_2O/Au(100) surfaces using a lower ratio of water to K. Figure 6.4a is an image acquired after adsorption of 0.20 ML of water on a Au(100) surface which was pre-adsorbed with 0.33 ML of K. There are similarities between this image and Figure 6.2a. First, there are two levels. The stripes are found at both levels, and they are mostly oriented in the two orthogonal NN directions of the substrate. Second, there are regions without stripes, and these 'no-stripe' regions are also oriented to the two orthogonal NN directions. Figure 6.4b is a cross-section profile along the arrow in Figure 6.4a. The difference in height between a stripe in the upper level and one in the lower level equals to one gold atomic step (see symbol ♦ in the profile).

This image is different from images obtained with the higher water to potassium ratio in several ways. The stripes are less ordered and are wider in general, thus the spacing between stripes, as determined by examination of 10 images, varies more widely from 1.0 nm to 3.1 nm while the width of these ranges vary from 0.9 to 1.2 nm. Moreover, the sample has more 'no-stripe' regions, which locate around the border of the levels. Interestingly, the widths of the 'no-stripe' regions are not random, but rather fall into four distinct values. Figure 6.4b depicts the cross-section profile across 'no-stripe' region 2. The profile shows that region 2 is 5.8 nm wide.

Cross-section profiles of other 'no-stripe' regions were analyzed, and the widths of regions 1, 2, 3, 4, 5, and 6 are 2.9 nm, 5.8 nm, 2.7 nm, 2.9 nm, 4.4 nm, and 1.2 nm, respectively. The absolute errors of these measurements are ± 0.17 nm. These spacings are integral multiples of five times the Au(100) nearest neighbor spacing of 0.29 nm.

Discussion

The results presented here show that the K/Au(100) surface is considerably altered when exposed to water. This exposure leads to the formation of stripes and to 'no stripe' zones close to step edges.

Origin of the stripes

The stripes are observed after the K-modified Au surface is exposed to water. At low coverages of K (0.06 ML) on Pt, water is adsorbed molecularly. However, at higher coverages, water must dissociate to form KOH, an effect observed on Ag and Pt surfaces in several photoemission studies. For example, Bonzel et al. showed that water dissociated when the coverage of K is 0.06 ML or higher on Pt(111).[244] And on Ag(111) surfaces, coadsorption of K and H_2O leads to water dissociation.[231] Thus, we expect that the stripes relate to the formation of KOH on the Au(100) surface. The water molecules dissociate as they adsorb on the Au(100) surface which is preadsorbed with 0.25 ML of K.

The images show that the two-level system formed as a consequence of adsorption of K on clean Au(100) remains after dosing with water. The stripes form at both levels and are directed along the two orthogonal NN directions (see Figure 6.2a). This result suggests that adsorption of water does not affect the underlying Au surface structure, but rather that the water

interacts with the (1 × 2) missing-row structure[75] on this surface; a schematic of this interaction is shown in Figure 6.5a. In other words, the results indicate that there is no subsurface K with which the water could interact. This idea is consistent with vibrational spectroscopic measurements on Pt, which found no evidence for subsurface K.[233]

The stripes are oriented along the directions formed by the row structure. The interesting labyrinthine structure observed on the surface likely arises from kinetic effects whereby growth of the stripe is nucleated and proceeds preferentially down one of the NN directions until stopped by stripe growth orthogonal to this direction. In this sense the growth found here mimics that found for growth of Al on Si(100) and related systems where the growing ends of the metallic stripes in that case form preferential sites for the subsequent growth of the chain.[245-246] The structures found here are also similar to those found in the growth of $Ce_{1-x}Gd_xO_{2-y}$ nanowires on $LaAlO_3$, the branching of which is ascribed to a kinetic effect arising from attractive interactions between orthogonal rows.[247] The two-fold symmetry on the Au(100) surface means that growth in either NN direction is possible, unlike the case for Al growth on the reconstructed Si(100) lattice. The labyrinthine structure likely derives from a multiplicity of nucleation sites on this surface. We were unable to observe the initial stages of the growth of water on this surface and so do not have a clear idea of the exact form of the nucleation site itself.

The kinetic effect implicated in the labyrinthine structure found here is different from effects giving rise to labyrinths in other systems. For example, labyrinthine patterns are found in thin liquid films[248], bilayers[249], magnetic materials[250], certain metal on metal systems[251-252], and ionic liquid/electrode interfaces[253-254]. The origin of these patterns is usually ascribed to spinodal decomposition, in which instability arises from phase separation, and the labyrinthine structure is a manifestation of this phase separation. In all these cases, however, the symmetry of

the underlying lattice is not registered in the overlayer. Rather, the spinodal decomposed systems typically evince worm-like features, the spacing of which depends on system specifics[248-254]. Figure 6.2a shows clearly that the 0.5 ML water/ 0.25 ML K overlayer is registered with the Au(100) substrate. The appearance of 90° angles is inconsistent with the 'worm-like' behavior expected in the spinodal case. At lower water coverages (Figure 6.4a), registry with the substrate is relaxed, yet even here registration with the substrate can be seen.

The widths of the stripes also provide a crucial hint as to their structure. The ionic radii of K^+ and OH^- are both 0.133 nm. The measured width of the stripes (0.8 – 1.0 nm) is much larger than that expected for KOH alone (lattice constant = 0.578 nm). The discrepancy in width is likely due to the presence of water adlayers around the KOH centers, as has been described by Bonzel[244]. Thus, we associate the stripes with hydrated KOH ad-layers, with the water lying to the side of the KOH. The measured height of the stripes (ca 0.1 nm) is too small to accommodate water on top. Images obtained with increased K^+/H_2O ratio (Figure 6.4a) also point out the crucial role of water in stabilizing the labyrinthine structure observed.

Using the van der Waals dimensions of water and the ionic radii of K^+ and OH^-, a possible structure of the stripe is shown in Figure 6.5b. In the model, the K^+ to H_2O nearest neighbors distance and the OH^- to H_2O nearest neighbors distance are assumed to be 0.292 nm, which are same as the K^+ to H_2O neighbors distance and the OH^- to H_2O neighbors distance measured by X-ray diffraction of KOH solutions.[255] The K^+ and OH^- reside around the trough of the (1×2) missing-row structure. KOH has a rock salt crystal structure.[256-257] One face of this crystal can well fit into the stripes observed. In the model, K^+ and OH^- have a separation equal to the sum of their ionic radii. The alternating K^+ and OH^- pattern is identical to that found in

the crystalline material. The van der Waals diameters of water, K^+, and OH^- are 0.282 nm, 0.266 nm, and 0.266 nm, respectively. As shown in Figure 6.5b, the stripes can arrange along the two orthogonal NN directions. The calculated width of the stripes in this model, including the van der Waals diameter of water, is 1.13 nm. We note that this is very near four times the Au lattice spacing, which is equal to 1.154 nm.

DFT calculations show that 2 KOH molecules adsorbed in an antiparallel configuration on Au(100) was plausible, showing that alternating lines of KOH molecules can be stable on the surface relative to side-on and parallel configurations. The side-on Configurations 3 and 4 also feature good stability because of the lack of electrostatic repulsions. The low energy configurations for these configurations are shown in Figure 6.3 and Figure 6.6.

Because it exhibits agrees with observations, the antiparallel Configuration 2 was used as the starting point to examine how the KOH array might turn a corner or intersect as two perpendicular stripes as depicted in Figure 6.5b. We note that this is despite the fact that Configurations 1, 3, and 4 registered lower energy minima, which we propose occurs because these configurations remove the strong electrostatic repulsions. These configurations, however, do not match the STM observations as they are not indicative of stripe propagation.

As a first test of forming perpendicular stripes of KOH on the surface of Au(100), Configurations 5 and 6 are compared. Interestingly, Configuration 5, featuring 2 antiparallel KOH molecules with a third approaching with K^+ and OH^- in electrostatically favored position, has a higher energy minimum following a dynamics simulation than the opposite case in Configuration 6. As seen in Figure 6.7, this occurs because the Configuration 6 structure relaxes in energy by moving electrostatically repellant groups away from each other, leading to low

energy structure incompatible with the observed labyrinthine structure in Figure 6.2a. Configuration 5 still yields an energy minimum close to that of Configuration 6, but with a structure that could plausibly form perpendicular stripes on the surface.

Simulations using Configurations 9 and 10 explore the same 2 antiparallel KOH molecules, but with the third KOH approaching in a side-on fashion similar to in Configurations 3 and 4. In this case, Configuration 9 produces a much lower energy minimum than Configuration 10 along with vastly different final structures. Configuration 9, starting with a more electrostatically favored orientation, relaxes into a structure that can propagate stripes in two orthogonal directions. Configuration 10, like Configuration 6, achieves a minimum energy structure by charge repulsion. These simulations provide some indication that a striped structure can be formed on Au(100) surfaces. This is particularly true as K coverage is increased and a scheme with closer packing is necessary to accommodate the entire amount of adsorbed K and H_2O.

We performed similar simulations on both the unreconstructed Au(100) surface and on a Au surface with coadsorbed H_2O, but results obtained from these calculations were very similar to those reported above absent the reconstruction and adsorbed H_2O. K to Au and O to Au distances are tabulated for KOH on unreconstructed Au(100) in Supporting Information in Table 6.2. These values are close to the expected distances based solely on ionic and atomic radii (3.17 Å K^+ to Au; 3.19 Å O^{2-} to Au) and indicate that the KOH is in fact interacting with the Au slab in the calculation. Thus, DFT calculations provide further support for the suggestion that hydrated KOH is the source of the labyrinthine stripe structure.

The model requires a K: H_2O ratio of 1:3 while experimentally, this ratio is 1:2. Thus, the model as described would leave a large amount of unreacted K on the surface. Some of this K might be in the 'no stripe' region as described below. Alternatively, the hydration might not exhibit the perfection shown in the model. The presence of turns in the labyrinthine structure will reduce the K requirement. Defects in the model, possibly giving rise to the heterogeneity in stripe width seen in Figure 6.2a, may also reduce the amount of K required to form the stripes. A model featuring a K:H_2O ratio of 1:2 would exhibit a width of 0.7 nm, which is somewhat smaller than what is actually observed.

Interestingly, images obtained from the surface exhibiting the lower water/K ratio features stripes not nearly as well formed as those from the higher water/K ratio. This result emphasizes the role of water in stabilizing the stripe structure. The reduced water level may result in less KOH formation, leaving more unreacted K on the Au surface. The difficulty in imaging this K adlayer, possibly due to fluxionality, has been noted above.

The 'no-stripe' region

Images in Figure 6.2a and 6.4a were acquired from samples featuring different ratio of K/water ratios. The amount of 'no-stripe' region is greater in the sample featuring the higher ratio of K to water (Figure 6.4a) which suggests that these 'no-stripes' regions are associated with anhydrous K. The 'no-stripe' regions are oriented along the two orthogonal NN directions, reflecting the intrinsic step edge orientation. That the step edges are the location of the no stripe regions implies that it is harder to oxidize K in these regions than it is on the terrace, a result consistent with the expected lower electronegativity (work function) in the step region.

Conclusions

Variable temperature STM is employed to examine adsorption of water and K on Au(100) surfaces. Upon adsorption of K of 0.25 ML to 0.33 ML, a two-level system is formed on Au(100), and the (5 × 20) reconstruction is completely lifted. Adsorption of water on these K-modified Au(100) surfaces at 80 K resulted in the formation of the stripes which are observed at both levels of the two-level system. The stripes are 1.4 nm to 1.7 nm wide and arrange along the two orthogonal, nearest neighbor directions of Au(100) surfaces. The dimensions of the stripes suggest that the stripes are hydrated KOH adlayers. DFT calculations support the conclusion that the observed labyrinthine structure suggests the energy required to grow orthogonally to a row direction is similar to that required to continue along the row direction.

Images show regions where the stripes are not formed. From the measurements of samples with different ratio of K to water, the amount of these 'no-stripe' regions are found to increase with the relative ratio of K to water. This finding suggests that the 'no-stripe' regions are unreacted K.

Acknowledgments

The authors acknowledge Vania Petrova and the staff of the Center for Microanalysis of Materials for their assistance. This work was funded by the National Science Foundation.

Tables

Table 6.1: Calculated KOH Adsorption Energies.

KOH on Au(100) Configurations	Adsorption Energy (eV)*
1	-2.65
2	-2.10
3	-2.90
4	-2.54
5	-2.89
6	-3.29
9	-4.15
10	-2.84

*E_{ads}, calculated as the difference between E_{total} (the total energy for KOH adsorption on the slab) and the sum of E_{KOH} (the free KOH energy) and E_{slab} (the isolated Au(100) slab).

Table 6.2: K to Au and O to Au interatomic distances tabulated from the lowest energy conformation as calculated using VASP on unreconstructed Au(100) surface.

Configuration	KOH to surface distances (Å)			
	Potassium-Gold		Oxygen-Gold	
1	K1-Au3 K1-Au19 K2-Au11 K2-Au27	3.278 3.318 3.2 3.594	O1-Au19 O1-Au23 O1-Au35 O1-Au39 O1-Au3 O1-Au7 O2-Au27 O2-Au23 O2-Au43 O2-Au11 O2-Au39	2.371 2.498 3.686 3.769 3.78 3.861 2.233 2.924 3.462 3.824 3.943

Table 6.2 (Continued):

2	K1-Au7 K1-Au23 K1-Au3 K2-Au23 K2-Au39 K2-Au27 K2-Au43	3.725 3.757 3.977 3.682 3.776 3.827 3.917	O1-Au35 O1-Au19 O2-Au23 O2-Au7 O2-Au27 O2-Au11	2.865 2.908 3.419 3.543 3.648 3.764
3	K1-Au3 K1-Au19 K2-Au27 K2-Au23	3.3 3.631 3.536 3.903	O1-Au23 O1-Au19 O1-Au7 O1-Au39 O1-Au27 O2-Au27 O2-Au31 O2-Au11 O2-Au15	2.33 3.399 3.607 3.806 3.992 2.449 2.951 3.079 3.492
4	K1-Au7 K1-Au3 K1-Au23 K2-Au31 K2-Au27 K2-Au15	3.425 3.702 3.778 3.299 3.686 3.974	 O1-Au23 O1-Au19 O2-Au27 O2-Au11	 2.368 2.586 2.426 3.095
5	K1-Au3 K1-Au19 K1-Au7 K1-Au23 K2-Au43 K2-Au39 K2-Au27 K2-Au23 K3-Au35 K3-Au39 K3-Au51 K3-Au55	3.795 3.812 3.829 3.846 3.695 3.762 3.907 3.97 3.715 3.766 3.793 3.842	 O1-Au23 O1-Au19 O2-Au27 O2-Au23 O2-Au11 O2-Au7 O3-Au39 O3-Au55 O3-Au43	 3.716 3.733 3.364 3.47 3.766 3.861 3.657 3.727 3.978

Table 6.2 (Continued):

6	K1-Au3 K1-Au7 K1-Au19 K1-Au23 K2-Au27 K2-Au23 K2-Au11 K3-Au59 K3-Au55	3.294 3.524 3.636 3.846 3.22 3.54 3.996 3.149 3.444	O1-Au23 O1-Au19 O1-Au39 O2-Au7 O2-Au11 O2-Au55 O3-Au39 O3-Au55 O3-Au43 O3-Au59	2.658 3.423 3.674 2.84 3.303 3.882 2.345 2.726 3.143 3.437
9	K1-Au23 K1-Au7 K1-Au19 K1-Au3 K2-Au27 K2-Au43 K2-Au23 K3-Au55 K3-Au39	3.717 3.756 3.853 3.891 3.617 3.877 3.947 3.416 3.539	O1-Au39 O2-Au11 O2-Au7 O2-Au27 O2-Au23 O3-Au43 O3-Au59 O3-Au39	3.659 2.736 2.898 2.944 3.095 3.087 3.821 3.828
10	 K1-Au7 K1-Au23 K1-Au3 K1-Au19 K2-Au23 K2-Au39 K2-Au27 K3-Au59 K3-Au43	 3.768 3.776 3.863 3.87 3.548 3.885 3.946 3.24 3.656	O1-Au23 O1-Au19 O1-Au39 O1-Au35 O2-Au11 O2-Au27 O2-Au7 O2-Au23 O2-Au6 O3-Au39 O3-Au43 O3-Au55	3.585 3.662 3.871 3.943 2.544 2.77 2.84 3.044 3.949 3.213 3.681 3.771

Table 6.3: Calculated KOH Adsorption Energies on the unreconstructed Au(100) surface.

KOH on Au(100) Configurations	Adsorption Energy (eV)*
1	-1.505
2	-2.096
3	-1.899
4	-1.942
5	-3.131
6	-3.585
9	-3.206
10	-3.132

*E_{ads}, calculated as the difference between E_{total} (the total energy for KOH adsorption on the slab) and the sum of E_{KOH} (the free KOH energy) and E_{slab} (the isolated Au(100) slab).

Figures

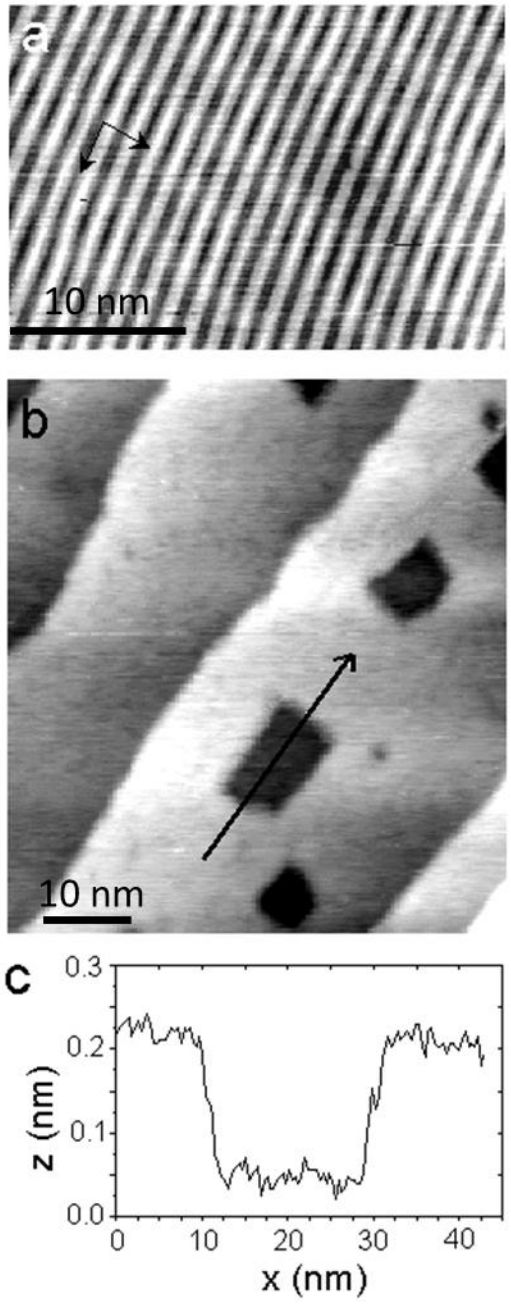

Figure 6.1: (a) 29 nm × 20 nm image of a clean Au(100) surface (V_{tip} = -0.316 V, I = 1.20 nA, T_{sample} = 300 K), (b) 86 nm □ 96 nm image of the surface after adsorption of 0.25 ML of K (V_{tip} = -1.39 V, I = 0.82 nA, T_{sample} = 300 K), (c) a cross-section profile along the arrow in (b).

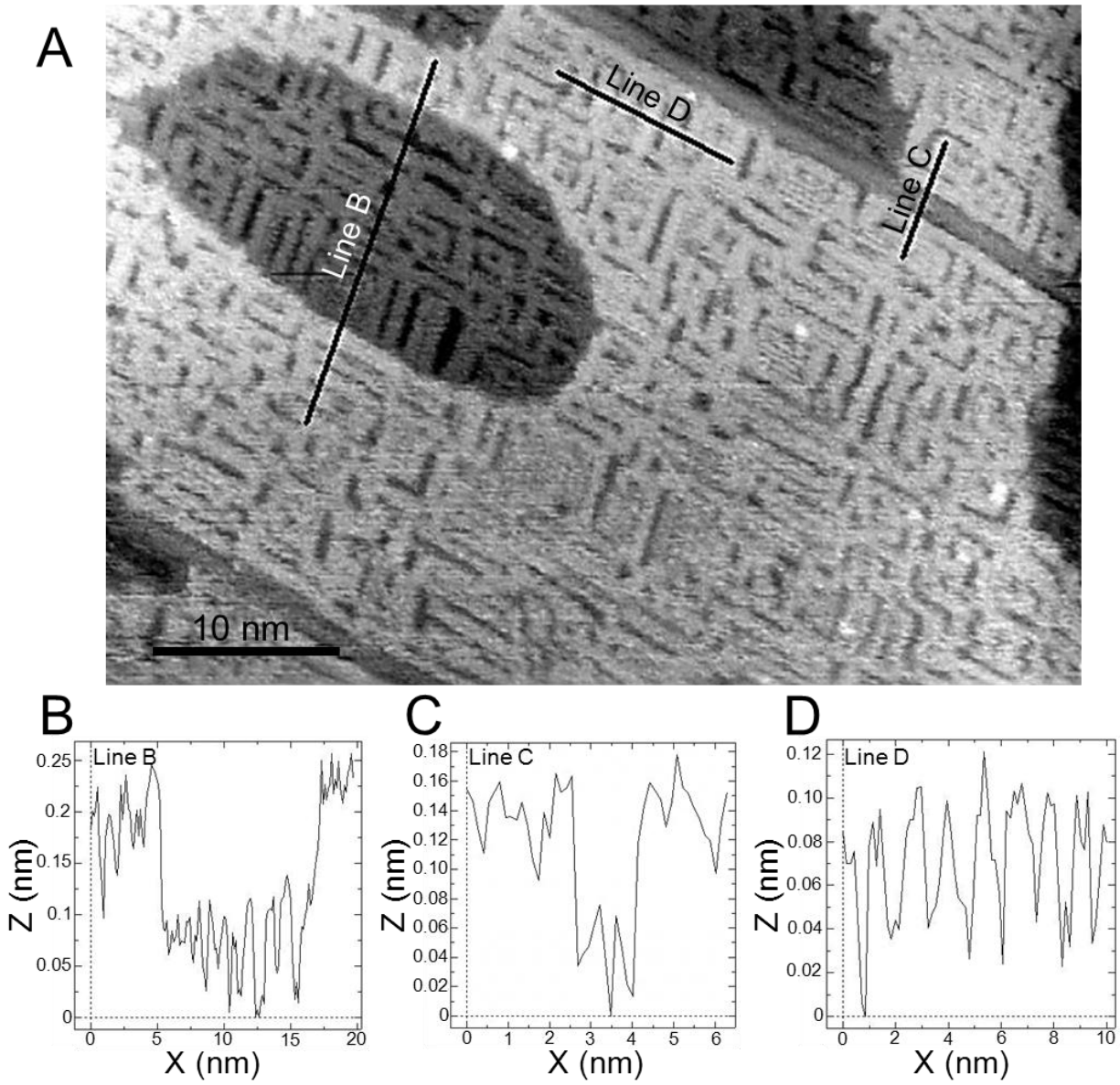

Figure 6.2: (A) 50 nm × 35 nm image of the surface after adsorption of 0.5 ML of water on a Au(100) surface pre-adsorbed with 0.25 ML of K (V_{tip} = -1.5 V, I = 0.41 nA, T_{sample} = 80 K), (B) cross-section profile along the arrow marked 'Line B' in (A). (C) Cross sectional profile along the bar marked 'Line C' in (A). (D) Cross sectional profile along the bar marked 'Line D' in (A).

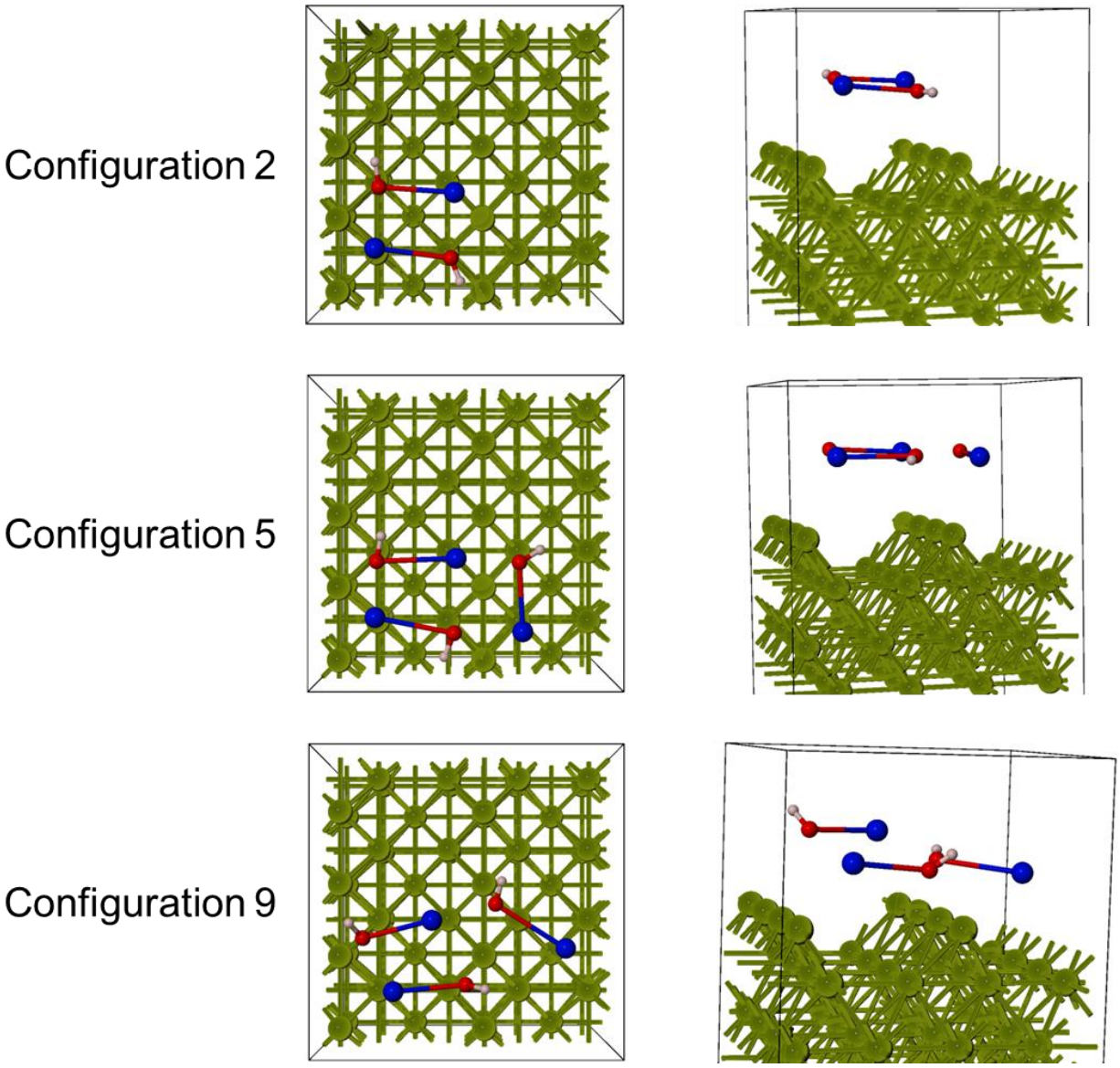

Figure 6.3: Molecular dynamics simulation low energy structures of KOH molecules on Au(100) as calculated using VASP.

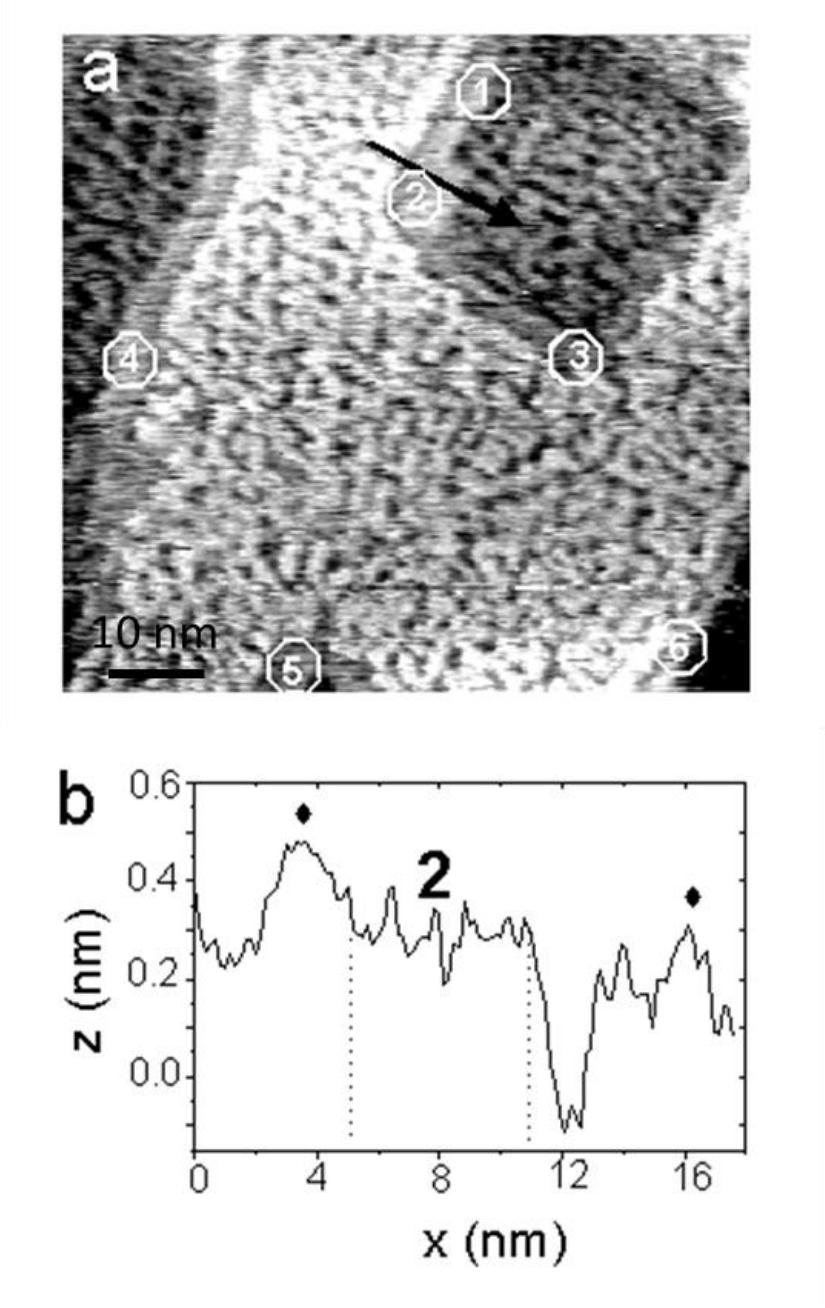

Figure 6.4: (a) 51 nm × 48 nm image of a Au(100) surface dosed with 0.33 ML of K and 0.2 ML of water (V_{tip} = -1.44 V, I = 0.31 nA, T_{sample} = 80 K), (b) a cross-section profile of the arrow in (a). Dotted lines mark 'no-stripes' region □. Symbols ♦ mark the stripes in the upper level and the lower level.

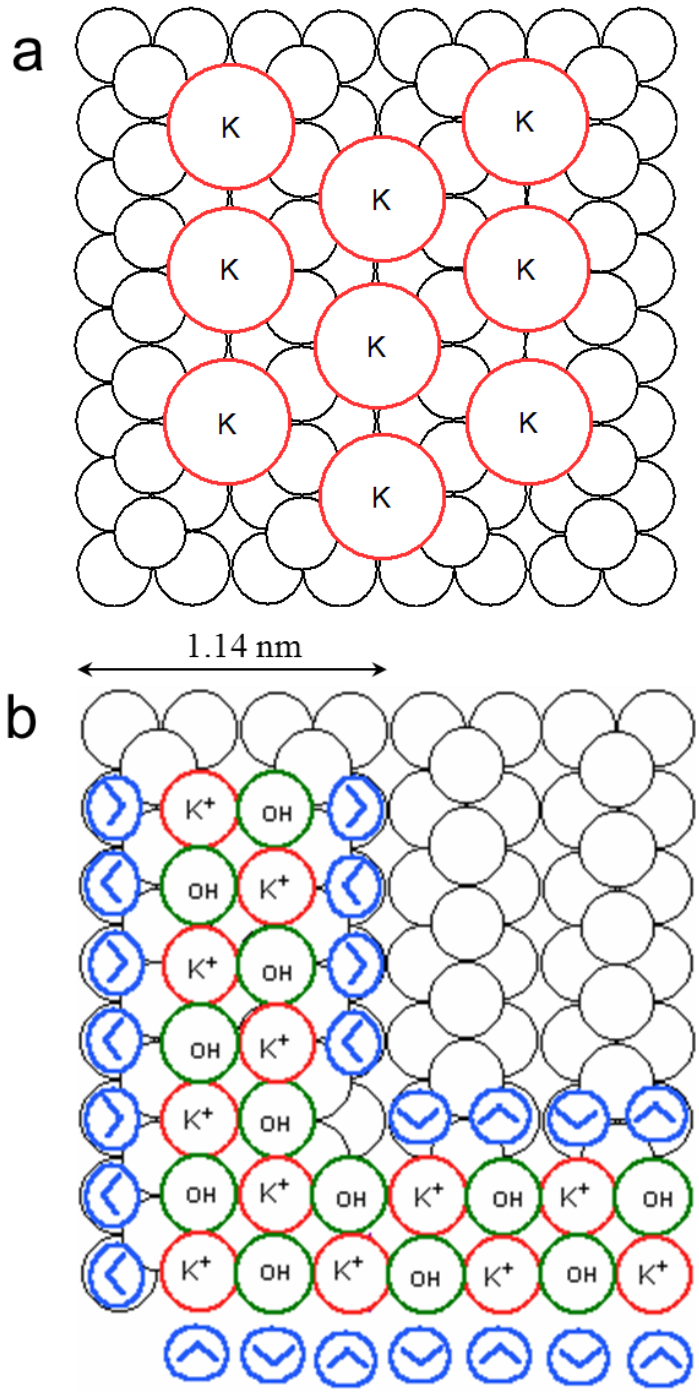

Figure 6.5: (a) Schematics for the (1 × 2) missing-row structure with 0.25 ML of K suggested by Barth et al[75]. (b) Proposed structure for stripes, with blue wedges representing adsorbed water.

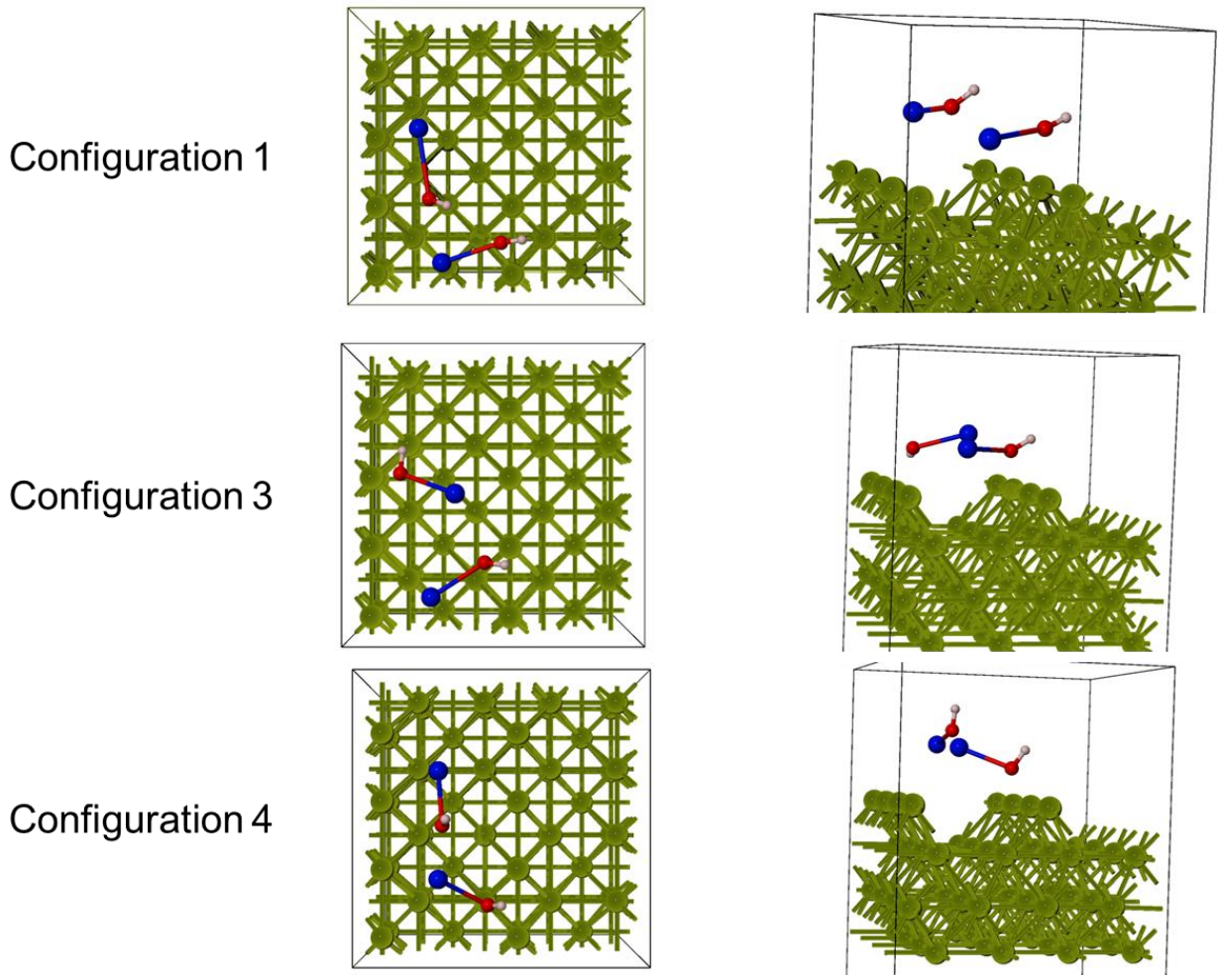

Figure 6.6: Molecular dynamics simulation low energy structures of 2 KOH molecules on (1×2) reconstructed Au(100) as calculated using VASP.

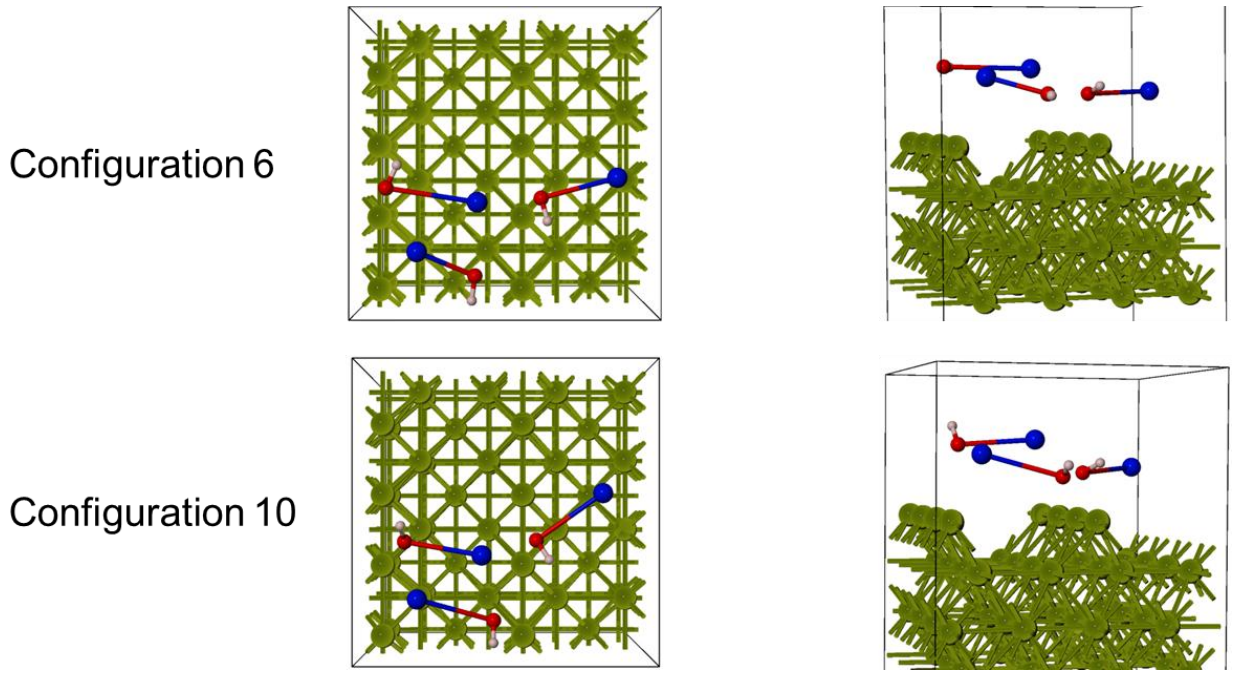

Figure 6.7: Molecular dynamics simulation low energy structures of 3 KOH molecules on (1×2) reconstructed Au(100) as calculated using VASP.

References

(1) Conte, M.; Iacobazzi, A.; Ronchetti, M.; Vellone, R., *Journal of Power Sources* **2001,** *100*, 171.

(2) Lewis, N. S.; Nocera, D. G., *Proceedings of the National Academy of Sciences* **2006,** *103*, 15729.

(3) Serrano, E.; Rus, G.; García-Martínez, J., *Renewable and Sustainable Energy Reviews* **2009,** *13*, 2373.

(4) Yerga, Rufino M. N.; Galván, M. C. Á.; del Valle, F.; Villoria de la Mano, José A.; Fierro, José L. G., *ChemSusChem* **2009,** *2*, 471.

(5) Cortright, R. D.; Davda, R. R.; Dumesic, J. A., *Nature* **2002,** *418*, 964.

(6) Navarro, R. M.; Pena, M. A.; Fierro, J. L. G., *Chemical Reviews* **2007,** *107*, 3952.

(7) Ni, M.; Leung, M. K. H.; Leung, D. Y. C.; Sumathy, K., *Renewable and Sustainable Energy Reviews* **2007,** *11*, 401.

(8) Hoffert, M. I.; Caldeira, K.; Jain, A. K.; Haites, E. F.; Harvey, L. D. D.; Potter, S. D.; Schlesinger, M. E.; Schneider, S. H.; Watts, R. G.; Wigley, T. M. L.; Wuebbles, D. J., *Nature* **1998,** *395*, 881.

(9) Roy, S. C.; Varghese, O. K.; Paulose, M.; Grimes, C. A., *Acs Nano* **2010,** *4*, 1259.

(10) Baxter, J. B., *J. Vac. Sci. Technol. A* **2012,** *30*.

(11) Nazeeruddin, M. K.; Baranoff, E.; Gratzel, M., *Sol. Energy* **2011,** *85*, 1172.

(12) Kumar, P.; Chand, S., *Prog. Photovoltaics* **2012,** *20*, 377.

(13) Jelle, B. P.; Breivik, C.; Rokenes, H. D., *Sol. Energy Mater. Sol. Cells* **2012,** *100*, 69.

(14) Li, G.; Zhu, R.; Yang, Y., *Nat. Photonics* **2012,** *6*, 153.

(15) *Basic Research Needs for Solar Energy Utilization: Report on the Basic Energy Sciences Workshop in Solar Energy Utilization*; Argonne Nat'l Laboratories: 2005.

(16) Krol, R. v. d.; Liang, Y.; Schoonman, J., *Journal of Materials Chemistry* **2008,** *18*, 2311.

(17) Fujishima, A., Honda, K., *Nature* **1972,** *238*, 37.

(18) Lehn, J. M., Sauvage, J. P., Ziessel, R., *Nouveau Journal de Chimie* **1980,** *4*, 623.

(19) Sato, S., White, J.M., *Industrial & Engineering Chemistry Product Research and Development* **1980,** *19*, 542.

(20) Domen, K. N., Shuichi; Soma, Mitsuyuki; Onishi, Takaharu; Tamaru, Kenzi., *Journal of the Chemical Society, Chemical Communications* **1980,** *12*, 543.

(21) Osterloh, F. E., *Chemistry of Materials* **2007,** *20*, 35.

(22) Maeda, K.; Teramura, K.; Lu, D.; Takata, T.; Saito, N.; Inoue, Y.; Domen, K., *Nature* **2006,** *440*, 295.

(23) Maeda, K.; Domen, K., *The Journal of Physical Chemistry C* **2007,** *111*, 7851.

(24) Dolgos, M. R.; Paraskos, A. M.; Stoltzfus, M. W.; Yarnell, S. C.; Woodward, P. M., *Journal of Solid State Chemistry* **2009,** *182*, 1964.

(25) Bard, A. J.; Faulkner, L. R., *Electrochemical Methods*. John Wiley & Sons: New York, 1980.

(26) Palacin, M. R., *Chem. Soc. Rev.* **2009,** *38*, 2565.

(27) Scrosati, B.; Garche, J., *J. Power Sources* **2010,** *195*, 2419.

(28) Feng, F.; Geng, M.; Northwood, D. O., *International Journal of Hydrogen Energy* **2001,** *26*, 725.

(29) Parsons, R., *Electrochimica Acta* **1976,** *21*, 681.

(30) Delahay, P., *Double Layer and Electrode Kinetics*. Interscience Publishers: New York, 1965.

(31) Conway, B. E.; Korzeniewski, C., *The Electrochemical Double Layer - Commemorating Fifty Years of D.C. Grahame's Ground-Breaking Paper*. The Electrochemical Society: Pennington, NJ, 1997; Vol. 97-17.

(32) Ritchie, I. M.; Bailey, S.; Woods, R., *Advances in Colloid & Interface Science* **1999,** *80*, 183.

(33) Ambrosio, R. C.; Gewirth, A. A., *Analytical Chemistry* **2010,** *82*, 1305.

(34) Rosca, V.; Duca, M.; de Groot, M. T.; Koper, M. T. M., *Chem. Rev.* **2009,** *109*, 2209.

(35) Markovic, N. M.; Gasteiger, H. A.; Ross, P. N., *The Journal of Physical Chemistry* **1995,** *99*, 3411.

(36) Thorum, M. S. Oxygen Reduction Electrocatalysis, Ph.D Dissertation. University of Illinois Urbana-Champaign, 2011.

(37) Milhano, C.; Pletcher, D., The Electrochemistry and Electrochemical Technology of Nitrate. In *Modern Aspects of Electrochemistry, No 45*, White, R. E.; Vayenas, C. G.; GamboaAldeco, M., Eds. Springer: New York, 2009; pp 1.

(38) Gewirth, A. A.; Thorum, M. S., *Inorganic Chemistry* **2010,** *49*, 3557.

(39) Stewart, K. L. Copper surface chemistry relevant to chemical mechanical planarization (CMP), Ph.D. Dissertation. University of Illinois at Urbana-Champaign, 2007.

(40) Oliver, M. R., *Chemical Mechanical Planarization of Semiconductor Materials*. Springer: Berlin, 2004.

(41) Anema, J. R.; Li, J. F.; Yang, Z. L.; Ren, B.; Tian, Z. Q., Shell-Isolated Nanoparticle-Enhanced Raman Spectroscopy: Expanding the Versatility of Surface-Enhanced Raman Scattering. In *Annual Review of Analytical Chemistry, Vol 4*, Cooks, R. G.; Yeung, E. S., Eds. Annual Reviews: Palo Alto, 2011; Vol. 4, pp 129.

(42) Huang, Y. F.; Li, C. Y.; Broadwell, I.; Li, J. F.; Wu, D. Y.; Ren, B.; Tian, Z. Q., *Electrochimica Acta* **2011,** *56*, 10652.

(43) Li, J. F.; Huang, Y. F.; Ding, Y.; Yang, Z. L.; Li, S. B.; Zhou, X. S.; Fan, F. R.; Zhang, W.; Zhou, Z. Y.; WuDe, Y.; Ren, B.; Wang, Z. L.; Tian, Z. Q., *Nature* **2010,** *464*, 392.

(44) Li, J. F.; Li, S. B.; Anema, J. R.; Yang, Z. L.; Huang, Y. F.; Ding, Y.; Wu, Y. F.; Zhou, X. S.; Wu, D. Y.; Ren, B.; Wang, Z. L.; Tian, Z. Q., *Appl. Spectrosc.* **2011,** *65*, 620.

(45) Li, J.-F.; Ding, S.-Y.; Yang, Z.-L.; Bai, M.-L.; Anema, J. R.; Wang, X.; Wang, A.; Wu, D.-Y.; Ren, B.; Hou, S.-M.; Wandlowski, T.; Tian, Z.-Q., *Journal of the American Chemical Society* **2011,** *133*, 15922.

(46) Li, S. B.; Li, L. M.; Anema, J. R.; Li, J. F.; Yang, Z. L.; Ren, B.; Sun, J. J.; Tian, Z. Q., *Z. Phys. Chemie-Int. J. Res. Phys. Chem. Chem. Phys.* **2011,** *225*, 775.

(47) Shanthil, M.; Thomas, R.; Swathi, R. S.; George, T. K., *Journal of Physical Chemistry Letters* **2012,** *3*, 1459.

(48) Mirabella, F. M., *Modern Techniques in Applied Molecular Spectroscopy*. John Wiley & Sons: New York, 1998.

(49) Long; Cai; Kisch, H., *The Journal of Physical Chemistry C* **2007,** *112*, 548.

(50) Kohn, W., Sham, L.J., *Phys. Rev. A* **1965,** *140*, 1133.

(51) Clark, S. J. S., Matthew D.; Pickard, Chris J.; Hasnip, Phil J.; Probert, Matt I. J.; Refson, Keith; Payne, Mike C., *Zeitschrift fuer Kristallographie* **2005,** *220(5-6)*, 567.

(52) Accelrys; Software; Inc. *Materials Studio Release Notes, Release 4.4*, Accelrys Software Inc.: San Diego, 2008.

(53) Touboul, M.; Toledano, P., *Acta Crystallographica, Section B: Structural Crystallography and Crystal Chemistry* **1980,** *B36*, 240.

(54) Touboul, M.; Ingrain, D., *Journal of the Less-Common Metals* **1980,** *71*, 55.

(55) Perdew, J. P., Wang, Y., *Phys. Rev. B* **1992,** *45*, 13244.

(56) Perdew, J. P.; Chevary, J. A.; Vosko, S. H.; Jackson, K. A.; Pederson, M. R.; Singh, D. J.; Fiolhais, C., *Physical Review B* **1992,** *46*, 6671.

(57) Perdew, J. P.; Burke, K.; Ernzerhof, M., *Phys. Rev. Lett.* **1996,** *77*, 3865.

(58) Enustun, B. V.; Turkevich, J., *Journal of the American Chemical Society* **1963,** *85*, 3317.

(59) LizMarzan, L. M.; Giersig, M.; Mulvaney, P., *Langmuir* **1996,** *12*, 4329.

(60) Brolo, A. G.; Jiang, Z.; Irish, D. E., *J. Electroanal. Chem.* **2003,** *547*, 163.

(61) Dretschkow, T.; Wandlowski, T., *Electrochimica Acta* **1999,** *45*, 731.

(62) Cruickshank, B. J.; Sneddon, D. D.; Gewirth, A. A., *Surf Sci* **1993,** *281*, L308.

(63) Schultz, Z. D.; Shaw, S. K.; Gewirth, A. A., *J Am Chem Soc* **2005,** *127*, 15916.

(64) Biggin, M. E. Ph.D. Thesis, *In situ vibrational spectroscopic and electrochemical study of electrodeposition additives on copper surfaces*. University of Illinois at Urbana-Champaign, Champaign, IL, 2001.

(65) Honesty, N. R.; Gewirth, A. A., *Journal of Raman Spectroscopy* **2012,** *43*, 46.

(66) Stewart, K. L.; Zhang, J.; Li, S.; Carter, P. W.; Gewirth, A. A., *Journal of The Electrochemical Society* **2007,** *154*, D57.

(67) Mazet, V.; Carteret, C.; Brie, D.; Idier, J.; Humbert, B., *Chemometrics and Intelligent Laboratory Systems* **2005,** *76*, 121.

(68) Morita, S.; Shinzawa, H.; Noda, I.; Ozaki, Y., *Appl. Spectrosc.* **2006,** *60*, 398.

(69) Watanabe, A.; Morita, S.; Ozaki, Y., *Biomacromolecules* **2006,** *7*, 3164.

(70) Noda, I.; Ozaki, Y., *Two Dimensional Correlation Spectroscopy - Applications in Vibrational and Optical Spectroscopy*. John Wiley and Sons: New York, 2004.

(71) Noda, I.; Dowrey, A. E.; Marcott, C.; Story, G. M.; Ozaki, Y., *Appl. Spectrosc.* **2000,** *54*, 236a.

(72) Sun, S. T.; Tang, H.; Wu, P. Y.; Wan, X. H., *Physical Chemistry Chemical Physics* **2009,** *11*, 9861.

(73) Sun, S. T.; Hu, J.; Tang, H.; Wu, P. Y., *Journal of Physical Chemistry B* **2010,** *114*, 9761.

(74) Ikemiya, N.; Gewirth, A. A., *Journal of the American Chemical Society* **1997,** *119*, 9919.

(75) Barth, J. V.; Schuster, R.; Behm, R. J.; Ertl, G., *Surface Science* **1994,** *302*, 158.

(76) Kohn, W., Sham, L.J., *Physical Review* **1965,** *140*, A1133.

(77) Kresse, G.; Furthm; uuml; ller, J., *Physical Review B* **1996,** *54*, 11169.

(78) Blochl, P. E., *Physical Review B* **1994,** *50*, 17953.

(79) Kresse, G.; Joubert, D., *Physical Review B* **1999,** *59*, 1758.

(80) Bae, S. E.; Stewart, K. L.; Gewirth, A. A., *J Am Chem Soc* **2007,** *129*, 10171.

(81) Kudo, A., *Pure and Applied Chemistry* **2007,** *79*, 1917.

(82) Kong, F. T., Dai, Song-Yuan, Wang, Kong-Jia *Advances in OptoElectronics* **2007,** *2007*.

(83) Jose, R., Thavasi, V., Ramakrishna, S., *J. Am. Cer. Soc.* **2009,** *92*, 289.

(84) Lenzmann, F. O., Kroon, J. M. , *Advances in OptoElectronics* **2007,** *2007*.

(85) Kudo, A.; Niishiro, R.; Iwase, A.; Kato, H., *Chemical Physics* **2007,** *339*, 104.

(86) Khan, S. U. M.; Al-Shahry, M.; Ingler, W. B., Jr., *Science* **2002,** *297*, 2243.

(87) Umebayashi, T.; Yamaki, T.; Yamamoto, S.; Miyashita, A.; Tanaka, S.; Sumita, T.; Asai, K., *Journal of Applied Physics* **2003,** *93*, 5156.

(88) Asahi, R.; Morikawa, T.; Ohwaki, T.; Aoki, K.; Taga, Y., *Science* **2001,** *293*, 269.

(89) Wu, G.; Nishikawa, T.; Ohtani, B.; Chen, A., *Chemistry of Materials* **2007,** *19*, 4530.

(90) Long, M.; Cai, W.; Cai, J.; Zhou, B.; Chai, X.; Wu, Y., *The Journal of Physical Chemistry B* **2006,** *110*, 20211.

(91) Siedl, N.; Elser, M. J.; Bernardi, J.; Diwald, O., *The Journal of Physical Chemistry C* **2009**.

(92) Zou, Z.; Ye, J.; Sayama, K.; Arakawa, H., *Nature* **2001,** *414*, 625.

(93) Ye, J.; Zou, Z.; Arakawa, H.; Oshikiri, M.; Shimoda, M.; Matsushita, A.; Shishido, T., *Journal of Photochemistry and Photobiology A: Chemistry* **2002,** *148*, 79.

(94) Ye, J.; Zou, Z.; Oshikiri, M.; Matsushita, A.; Shimoda, M.; Imai, M.; Shishido, T., *Chemical Physics Letters* **2002,** *356*, 221.

(95) Oshikiri, M.; Boero, M.; Ye, J.; Zou, Z.; Kido, G., *Journal of Chemical Physics* **2002,** *117*, 7313.

(96) Dunkle, S. S.; Helmich, R. J.; Suslick, K. S., *The Journal of Physical Chemistry C* **2009,** *113*, 11980.

(97) Kudo, A., *International Journal of Hydrogen Energy* **2006,** *31*, 197.

(98) Touboul, M.; Melghit, K.; Bénard, P.; Louër, D., *Journal of Solid State Chemistry* **1995,** *118*, 93.

(99) Lide, D. R., *"Atomic Radii of the Elements", CRC Handbook of Chemistry and Physics*. 89th ed.; CRC Press/Taylor and Francis: Boca Raton, FL, 2009.

(100) Lin, H.-Y.; Chen, Y.-F.; Chen, Y.-W., *International Journal of Hydrogen Energy* **2007,** *32*, 86.

(101) Denis, S.; Baudrin, E.; Touboul, M.; Tarascon, J. M., *Journal of the Electrochemical Society* **1997,** *144*, 4099.

(102) Baudrin, D., Orsini, Seguin, Touboul, Tarascon, *Journal of Materials Chemistry* **1999,** *9*, 101.

(103) Bish, D. L.; Reynolds, R. C., *Reviews in Mineralogy and Geochemistry* **1989,** *20*, 73.

(104) Touboul, M., Cuche, C., Ganne, M., Tournoux M., *Zeitschrift für anorganische und allgemeine Chemie* **1974,** *410*, 1.

(105) Goodhew, P. J., Humphreys, J., Beanland, R., *Electron Microscopy and Analysis*. 3rd ed.; Taylor and Francis: New York, 2001.

(106) Müller, N.; Hodes, G.; Vainas, B., *Journal of Electroanalytical Chemistry* **1984,** *172*, 155.

(107) Morisaki, H.; Hariya, M.; Yazawa, K., *Appl. Phys. Lett.* **1977,** *30*, 7.

(108) Pourbaix, M., *Atlas of Electrochemical Equilibria in Aqueous Solutions*. 2nd ed.; National Association of Corrosion Engineers: Houston, TX, 1974.

(109) Cho, I.-S.; Lee, S.; Noh, J. H.; Choi, G. K.; Jung, H. S.; Kim, D. W.; Hong, K. S., *The Journal of Physical Chemistry C* **2008,** *112*, 18393.

(110) Khan, S. U. M.; Akikusa, J., *The Journal of Physical Chemistry B* **1999,** *103*, 7184.

(111) Bard, A. J., Faulkner, Larry R., *Electrochemical Methods: Fundamentals and Applications*. 2nd ed.; John Wiley & Sons, Inc.: Singapore, 2004.

(112) Hashiguchi, H.; Maeda, K.; Abe, R.; Ishikawa, A.; Kubota, J.; Domen, K., *Bulletin of the Chemical Society of Japan* **2009,** *82*, 401.

(113) Matsumoto, Y., *Journal of Solid State Chemistry* **1996,** *126*, 227.

(114) Lide, D. R., *"Electrochemical Series", CRC Handbook of Chemistry and Physics*. 89th ed.; CRC Press, Taylor and Francis: Boca Raton, FL, 2009.

(115) Zhang, L.; Fu, H.; Zhang, C.; Zhu, Y., *Journal of Solid State Chemistry* **2006,** *179*, 804.

(116) Yao, J.-M.; Lee, C.-K.; Yang, S.-J.; Hwang, C.-S., *Journal of Alloys and Compounds* **2009,** *481*, 740.

(117) Oshikiri, M.; Boero, M.; Ye, J.; Aryasetiawan, F.; Kido, G., *Thin Solid Films* **2003,** *445*, 168.

(118) Perdew, J. P.; Levy, M., *Physical Review Letters* **1983,** *51*, 1884.

(119) Zunger, A.; Perdew, J. P.; Oliver, G. L., *Solid State Communications* **1980,** *34*, 933.

(120) Matsushima, S.; Obata, K.; Nakamura, H.; Arai, M.; Kobayashi, K., *Journal of Physics and Chemistry of Solids* **2003,** *64*, 2417.

(121) Zou, Z.; Ye, J.; Arakawa, H., *Chemical Physics Letters* **2000,** *332*, 271.

(122) Chang, H.; Kong, K.; Choi, Y. S.; In, E.; Choi, Y.; Baeg, J.-O.; Moon, S.-J., *Chemical Physics Letters* **2004,** *398*, 449.

(123) Walsh, A.; Yan, Y.; Huda, M. N.; Al-Jassim, M. M.; Wei, S.-H., *Chemistry of Materials* **2009,** *21*, 547.

(124) Janotti, A.; Van de Walle, C. G., *Physical Review B (Condensed Matter and Materials Physics)* **2007,** *76*, 165202.

(125) Lany, S.; Zunger, A., *Physical Review B (Condensed Matter and Materials Physics)* **2008,** *78*, 235104.

(126) Licht, S., *Encyclopedia of Electrochemistry: Volume 6, Semiconductor Electrodes and Photoelectrochemistry*. Wiley-VCH: Weinheim, 2002; Vol. 6.

(127) Campion, A.; Kambhampati, P., *Chemical Society Reviews* **1998,** *27*, 241.

(128) Stiles, P. L.; Dieringer, J. A.; Shah, N. C.; Van Duyne, R. P., *Annual Review of Analytical Chemistry* **2008,** *1*, 601.

(129) Nie, S.; Emory, S. R., *Science* **1997,** *275*, 1102.

(130) Moskovits, M., *Reviews of Modern Physics* **1985,** *57*, 783.

(131) Bin, R.; Guo-Kun, L.; Xiao-Bing, L.; Zhi-Lin, Y.; Zhong-Qun, T., *Analytical & Bioanalytical Chemistry* **2007,** *388*, 29.

(132) Park, S.; Yang, P.; Corredor, P.; Weaver, M. J., *Journal of the American Chemical Society* **2002,** *124*, 2428.

(133) Pettinger, B.; Ren, B.; Picardi, G.; Schuster, R.; Ertl, G., *Physical Review Letters* **2004,** *92*, 096101.

(134) Stöckle, R. M.; Suh, Y. D.; Deckert, V.; Zenobi, R., *Chemical Physics Letters* **2000,** *318*, 131.

(135) Hoon-Khosla, M.; Fawcett, W. R.; Goddard, J. D.; Tian, W. Q.; Lipkowski, J., *Langmuir* **2000,** *16*, 2356.

(136) Yang, D. F.; Bizzotto, D.; Lipkowski, J.; Pettinger, B.; Mirwald, S., *Journal of Physical Chemistry* **1994,** *98*, 7083.

(137) Noda, H.; Minoha, T.; Wan, L.-J.; Osawa, M., *J. Electroanal. Chem.* **2000,** *481*, 62.

(138) Dretschkow, T.; Wandlowski, T., *J. Electroanal. Chem.* **1999,** *467*, 207.

(139) Dretschkow, T.; Lampner, D.; Wandlowski, T., *J. Electroanal. Chem.* **1998,** *458*, 121.

(140) Hoon-Khosla, M.; Fawcett, W. R.; Chen, A. C.; Lipkowski, J.; Pettinger, B., *Electrochimica Acta* **1999,** *45*, 611.

(141) Zawada, K.; Bukowska, J., *Electrochimica Acta* **2004,** *49*, 469.

(142) Morita, S.; Kitagawa, K., *Journal of Molecular Structure* **2010,** *974*, 56.

(143) Ozaki, Y.; Ojima, S.; Noda, I., *Vibrational Spectroscopy* **2004,** *36*, 141.

(144) Ozaki, Y.; Noda, S., *Appl. Spectrosc.* **2000,** *54*, 230A.

(145) Noda, I., *Vibrational Spectroscopy* **2004,** *36*, 143.

(146) Noda, I., General Theory of Two-dimensional (2 D) Analysis. In *Handbook of Vibrational Spectroscopy*, Chalmers, J. M.; Griffith, P. R., Eds. Wiley: 2002; Vol. 3.

(147) De Bonis, A.; Compagnini, G.; Cataliotti, R. S.; Marletta, G., *Journal of Raman Spectroscopy* **1999,** *30*, 1067.

(148) Kim, M.; Itoh, K., *Journal of Physical Chemistry* **1987,** *91*, 126.

(149) Lim, J. K.; Joo, S. W., *Surface and Interface Analysis* **2007,** *39*, 684.

(150) Kamyshny, A. L.; Zakharov, V. N.; Fedorov, Y. V.; Galashin, A. E.; Aslanov, L. A., *Journal of Colloid and Interface Science* **1993,** *158*, 171.

(151) Kim, M.; Itoh, K., *J. Electroanal. Chem.* **1985,** *188*, 137.

(152) Dollish, F. R.; Fately, W. G.; Freeman, F. B., *Characteristic Raman Frequencies of Organic Compounds*. John Wiley & Sons: New York, 1974.

(153) Varsanyi, G., *Vibrational Spectra of Benzene Derivatives*. Academic Press: New York, 1969.

(154) Stolberg, L.; Morin, S.; Lipkowski, J.; Irish, D. E., *J. Electroanal. Chem.* **1991,** *307*, 241.

(155) Lu, T.; Cotton, T. M.; Birke, R. L.; Lombardi, J. R., *Langmuir* **1989,** *5*, 406.

(156) Pockrand, I.; Otto, A., *Solid State Communications* **1980,** *35*, 861.

(157) Khan, M. A.; Tuck, D. G., *Acta Crystallographica Section C* **1984,** *40*, 60.

(158) Basu, A.; Gafney, H. D.; Strekas, T. C., *Inorganic Chemistry* **1982,** *21*, 2231.

(159) Moissette, A.; Batonneau, Y.; Brémard, C., *Journal of the American Chemical Society* **2001,** *123*, 12325.

(160) Muniz-Miranda, M., *Journal of Raman Spectroscopy* **2000,** *31*, 637.

(161) Gao, P.; Weaver, M. J., *Journal of Physical Chemistry* **1985,** *89*, 5040.

(162) Takahashi, M.; Niwa, M.; Ito, M., *The Journal of Physical Chemistry* **1987,** *91*, 11.

(163) Cunha, F.; Tao, N. J., *Physical Review Letters* **1995,** *75*, 2376.

(164) Stolberg, L.; Lipkowski, J.; Irish, D. E., *J. Electroanal. Chem.* **1991,** *300*, 563.

(165) Moorcroft, M. J.; Davis, J.; Compton, R. G., *Talanta* **2001,** *54*, 785.

(166) Gabriela Elena, B., *Electrochimica Acta* **2009,** *54*, 996.

(167) Nolan, B. T.; Hitt, K. J.; Ruddy, B. C., *Environmental Science & Technology* **2002,** *36*, 2138.

(168) Canfield, D. E.; Glazer, A. N.; Falkowski, P. G., *Science* **2010,** *330*, 192.

(169) Galloway, J. N.; Townsend, A. R.; Erisman, J. W.; Bekunda, M.; Cai, Z. C.; Freney, J. R.; Martinelli, L. A.; Seitzinger, S. P.; Sutton, M. A., *Science* **2008,** *320*, 889.

(170) Fanning, J. C., *Coordination Chemistry Reviews* **2000,** *199*, 159.

(171) Taguchi, S.; Feliu, J. M., *Electrochimica Acta* **2008,** *53*, 3626.

(172) Molodkina, E. B.; Ehrenburg, M. R.; Polukarov, Y. M.; Danilov, A. I.; Souza-Garcia, J.; Feliu, J. M., *Electrochimica Acta* **2010,** *56*, 154.

(173) Dima, G. E.; de Vooys, A. C. A.; Koper, M. T. M., *Journal of Electroanalytical Chemistry* **2003,** *554*, 15.

(174) Bae, S. E.; Gewirth, A. A., *Faraday Discuss* **2008,** *140*, 113.

(175) Duca, M.; van der Klugt, B.; Koper, M. T. M., *Electrochimica Acta* **2012,** *68*, 32.

(176) Butcher, D. P.; Boulos, S. P.; Murphy, C. J.; Ambrosio, R. C.; Gewirth, A. A., *J. Phys. Chem. C* **2012,** *116*, 5128.

(177) Goodgame, D. M. L.; Hitchman, M. A., *Inorganic Chemistry* **1967,** *6*, 813.

(178) Nakamoto, K., *Infrared and Raman Spectra of Inorganic and Coordination Compounds*. 5th ed.; John Wiley & Sons: New York, 1997.

(179) Goodgame, D. M. L.; Hitchman, M. A., *Inorganic Chemistry* **1965,** *4*, 721.

(180) Goodgame, D. M. L.; Hitchman, M. A.; Marsham, D. F.; Phavanantha, P.; Rogers, D., *Journal of the Chemical Society D: Chemical Communications* **1969**, 1383.

(181) Clough, P. N.; Thrush, B. A.; Ramsay, D. A.; Stamper, J. G., *Chemical Physics Letters* **1973,** *23*, 155.

(182) Sellmann, D.; Gottschalk-Gaudig, T.; Haussinger, D.; Heinemann, F. W.; Hess, B. A., *Chem.-Eur. J.* **2001,** *7*, 2099.

(183) Pham, D.-T.; Tsay, S.-L.; Gentz, K.; Zoerlein, C.; Kossmann, S.; Tsay, J.-S.; Kirchner, B.; Wandelt, K.; Broekmann, P., *The Journal of Physical Chemistry C* **2007,** *111*, 16428.

(184) Garrido, M. E. H.; Pritzker, M. D., *Journal of The Electrochemical Society* **2008,** *155*, D332.

(185) Keller, H.; Saracino, M.; Nguyen, H. M. T.; Huynh, T. M. T.; Broekmann, P., *The Journal of Physical Chemistry C* **2012,** *116*, 11068.

(186) Pletcher, D.; Poorabedi, Z., *Electrochimica Acta* **1979,** *24*, 1253.

(187) Radovici, O.; Badea, G. E.; Badea, T., *Rev. Roum. Chim.* **2003,** *48*, 591.

(188) Zhou, G.; Yang, J. C., *Journal of Materials Research* **2005,** *20*, 1684.

(189) Besenbacher, F.; Norskov, J. K., *Prog. Surf. Sci.* **1993,** *44*, 5.

(190) Hwang, S., *Int. J. Electrochem. Sci.* **2012,** *7*, 1820.

(191) Gartland, P. O.; Berge, S.; Slagsvold, B. J., *Physical Review Letters* **1972,** *28*, 738.

(192) Masel, R. I., *Principles of Adsorption and Reaction on Solid Surfaces*. Wiley: 1996.

(193) Dima, G. E.; Rosca, V.; Koper, M. T. M., *Journal of Electroanalytical Chemistry* **2007,** *599*, 167.

(194) Tada, K.; Shimazu, K., *Journal of Electroanalytical Chemistry* **2005,** *577*, 303.

(195) Prusse, U.; Hahnlein, M.; Daum, J.; Vorlop, K. D., *Catalysis Today* **2000,** *55*, 79.

(196) Chu, Y. S.; Robinson, I. K.; Gewirth, A. A., *The Journal of Chemical Physics* **1999,** *110*, 5952.

(197) LaGraff, J. R.; Gewirth, A. A., *Surf Sci* **1995,** *326*, L461.

(198) Beverskog, B.; Puigdomenech, I., *Journal of The Electrochemical Society* **1997,** *144*, 3476.

(199) Filimonov, E. V.; Shcherbakov, A. I., *Protection of Metals* **2004,** *40*, 280.

(200) Castro, P. M.; Jagodzinski, P. W., *Spectrochimica Acta Part A: Molecular Spectroscopy* **1991,** *47*, 1707.

(201) Holthoff, E. L.; Stratis-Cullum, D. N.; Hankus, M. E., *Sensors* **2011,** *11*, 2700.

(202) Sylvia, J. M.; Janni, J. A.; Klein, J. D.; Spencer, K. M., *Analytical Chemistry* **2000,** *72*, 5834.

(203) Escribano, R. M.; Fernández-Torre, D.; Herrero, V. J.; Martín-Llorente, B.; Maté, B.; Ortega, I. K.; Grothe, H., *Vibrational Spectroscopy* **2007,** *43*, 254.

(204) Aksenenko, V. M.; Murav'ev, N. S.; Taranenko, G. S., *Journal of Applied Spectroscopy* **1986,** *44*, 70.

(205) Mosier-Boss, P. A.; Lieberman, S. H., *Appl. Spectrosc.* **2000,** *54*, 1126.

(206) Zhou, Z.; Huang, G. G.; Kato, T.; Ozaki, Y., *Journal of Raman Spectroscopy* **2011,** *42*, 1713.

(207) Wetzel, H.; Pettinger, B.; Wenning, U., *Chemical Physics Letters* **1980,** *75*, 173.

(208) Owens, F. J., *Molecular Physics* **2011,** *109*, 667.

(209) da Cunha, M. C. P. M.; Weber, M.; Nart, F. C., *Journal of Electroanalytical Chemistry* **1996,** *414*, 163.

(210) Brooker, M. H.; Irish, D. E., *Inorganic Chemistry* **1969,** *8*, 219.

(211) Ling, Y.; Mills, C.; Weber, R.; Yang, L.; Zhang, Y., *J Am Chem Soc* **2010,** *132*, 1583.

(212) Menzies, A. C.; Mills, H. R., *Proceedings of the Royal Society of London. Series A, Mathematical and Physical Sciences* **1935,** *148*, 407.

(213) Krishnan, R., *Proceedings of the Indian Academy of Sciences, Section A* **1947,** *26*, 432.

(214) Wen, N. P.; Brooker, M. H., *J. Phys. Chem.* **1995,** *99*, 359.

(215) Doyle, D. A.; Cabral, J. M.; Pfuetzner, R. A.; Kuo, A. L.; Gulbis, J. M.; Cohen, S. L.; Chait, B. T.; MacKinnon, R., *Science* **1998,** *280*, 69.

(216) Guidoni, L.; Torre, V.; Carloni, P., *Biochemistry-Us* **1999,** *38*, 8599.

(217) Cabarcos, O. M.; Weinheimer, C. J.; Lisy, J. M., *J Chem Phys* **1999,** *110*, 8429.

(218) Chang, F. R. C.; Skipper, N. T.; Sposito, G., *Langmuir* **1998,** *14*, 1201.

(219) Sposito, G.; Skipper, N. T.; Sutton, R.; Park, S. H.; Soper, A. K.; Greathouse, J. A., *P Natl Acad Sci USA* **1999,** *96*, 3358.

(220) Sass, J. K.; Bange, K.; Dohl, R.; Piltz, E.; Unwin, R., *Ber. Bunsen-Ges. Phys. Chem.* **1984,** *88*, 354.

(221) Thiel, P. A.; Madey, T. E., *Surf. Sci. Rep.* **1987,** *7*, 21.

(222) Henderson, M. A., *Surface Science Reports* **2002,** *46*, 1.

(223) Verdaguer, A.; Sacha, G. M.; Bluhm, H.; Salmeron, M., *Chemical Reviews* **2006,** *106*, 1478.

(224) Doering, D. L.; Madey, T. E., *Surf. Sci.* **1982,** *123*, 305.

(225) Morgenstern, M.; Michely, T.; Comsa, G., *Physical Review Letters* **1996,** *77*, 703.

(226) Villegas, I.; Weaver, M. J., *Journal of Physical Chemistry B* **1997,** *101*, 10166.

(227) Wagner, F. T., Simulation of the Electrical Double Layer in Ultrahigh Vacuum. In *Structure of Electrified Interfaces*, Lipkowski, J.; Ross, P. N., Eds. VCH: New York, 1993; p 309.

(228) Pirug, G.; Bonzel, H. P., Water at Metal Surfaces: The Influence of Coadsorbed Alkali Metals. In *Structure of Electrified Interfaces*, Lipkowski, J.; Ross, P. N., Eds. VCH: New York, 1993; pp 153.

(229) Baumann, P.; Pirug, G.; Reuter, D.; Bonzel, H. P., *Surface Science* **1995,** *335*, 186.

(230) Bonzel, H. P.; Pirug, G.; Winkler, A., *Chem Phys Lett* **1985,** *116*, 133.

(231) Blass, P. M.; Zhou, X. L.; White, J. M., *J. Phys. Chem.* **1990,** *94*, 3054.

(232) Huang, H. H.; Jiang, X.; Siew, H. L.; Chin, W. S.; Xu, G. Q., *Langmuir* **1998,** *14*, 7217.

(233) Klunker, C.; Steimer, C.; Hannon, J.; Giesen, M.; Ibach, H., *Surface Science* **1999,** *420*, 25.

(234) Chakarov, D. V.; Osterlund, L.; Kasemo, B., *Journal of Electron Spectroscopy & Related Phenomena* **1993,** *5*, 279.

(235) Chakarov, D. V.; Osterlund, L.; Kasemo, B., *Langmuir* **1995,** *11*, 1201.

(236) Ikemiya, N.; Gewirth, A. A., *Journal of Physical Chemistry B* **2000,** *104*, 873.

(237) Vanhove, M. A.; Koestner, R. J.; Stair, P. C.; Biberian, J. P.; Kesmodel, L. L.; Bartos, I.; Somorjai, G. A., *Surface Science* **1981,** *103*, 189.

(238) Gibbs, D.; Ocko, B. M.; Zehner, D. M.; Mochrie, S. G. J., *Physical Review B* **1990,** *42*, 7330.

(239) Okada, M.; Iwai, H.; Klauser, R.; Murata, Y., *J Phys-Condens Mat* **1992,** *4*, L593.

(240) Schroeder, S. L. M.; Neumann, A.; Solomun, T.; Lenzsolomun, P.; Christmann, K., *Surface Science* **1995,** *337*, 285.

(241) Giesen, M.; Dietterle, M.; Stapel, D.; Ibach, H.; Kolb, D. M., *Mater. Res. Soc. Symp. Proc.* **1997,** *451*, 9.

(242) Hussain, A.; Curulla Ferré, D.; Gracia, J.; Nieuwenhuys, B. E.; Niemantsverdriet, J. W., *Surface Science* **2009,** *603*, 2734.

(243) Li, X.; Gewirth, A. A., *J Am Chem Soc* **2003,** *125*, 7086.

(244) Kiskinova, M.; Pirug, G.; Bonzel, H. P., *Surface Science* **1985,** *150*, 319.

(245) Brocks, G.; Kelly, P. J.; Car, R., *Physical Review Letters* **1993,** *70*, 2786.

(246) Evans, M. M. R.; Nogami, J., *Phys. Rev. B-Condens Matter* **1999,** *59*, 7644.

(247) Gibert, M.; Garc; iacute; a, A.; Puig, T.; Obradors, X., *Physical Review B* **2010,** *82*, 165415.

(248) Neogi, P., *Journal of Physics: Condensed Matter* **2010,** *22*, 415102.

(249) Yoo, P. J.; Lee, H. H., *Physical Review Letters* **2003,** *91*, 154502.

(250) Chen, S. L.; Liu, W.; Zhang, D.; Gunaratne, G. H., *J Appl Phys* **2008,** *103*.

(251) Schuster, R.; Thron, D.; Binetti, M.; Xia, X. H.; Ertl, G., *Physical Review Letters* **2003,** *91*.

(252) Rougemaille, N.; El Gabaly, F.; Stumpf, R.; Schmid, A. K.; Thurmer, K.; Bartelt, N. C.; de la Figuera, J., *Physical Review Letters* **2007,** *99*.

(253) Dogel, J.; Tsekov, R.; Freyland, W., *J Chem Phys* **2005,** *122*.

(254) Pan, G.-B.; Freyland, W., *Physical Chemistry Chemical Physics* **2007,** *9*, 3286.

(255) Brady, G. W.; Krause, J. T., *J Chem Phys* **1957,** *27*, 304.

(256) Teichert, v. W.; Klemm, W., *Z. Anorg. u. Allgem. Chem.* **1939,** *243*, 138.

(257) Ibers, J. A.; Kumamoto, J.; Snyder, R. G., *J Chem Phys* **1960,** *33*, 1164.

Appendix A. Newport RLC685-35-100 685 nm laser system Standard Operating Procedures (SOP)

Introduction:

This SOP describes the Newport 685 nm laser and power source located on the Raman spectroscopy laser table in room A533 CLSL. This is a class IIIb, continuous wave diode laser. The power output is 34.8 mW and specified wavelength is 684.6 nm.

Hazards, Controls, and Personal Protective Equipment:

The beam is next to a 632 nm HeNe and 532 nm diode laser. Multiple gas cylinders are also present near the power sources of each laser. Computers and potentiostats are all in the vicinity of the instrument detector. There are also multiple inert gas lines running from the cylinders to the optical table. All of these represent trip or mechanical injury hazards.

Care should also be taken in the form of general laser safety protocols. Laser goggles and gloves should be worn in the presence of an operating laser. Laser signs should also be turned on to alert others to the hazard. Additionally, all reflective surfaces on the operator should be removed or covered (rings, watches, etc.).

Beam stops are available and should be used to contain the laser beam during experiment setup and optical alignment (when possible).

Experimental Protocol and Optical Alignment:

The 685 nm laser is operated with a turn-key switch on the front of the power source. Once on, the systems lases after several seconds of warmup time. The focal length is 4 in and the system can be fitted with a fiber optic cable to direct the beam into an in-situ Raman cell.

The beam experiences significant divergence, thus several considerations need to be considered for its use on an optical table that differ from beams used traditionally. A diagram of the optical configuration is presented below in Figure 1.

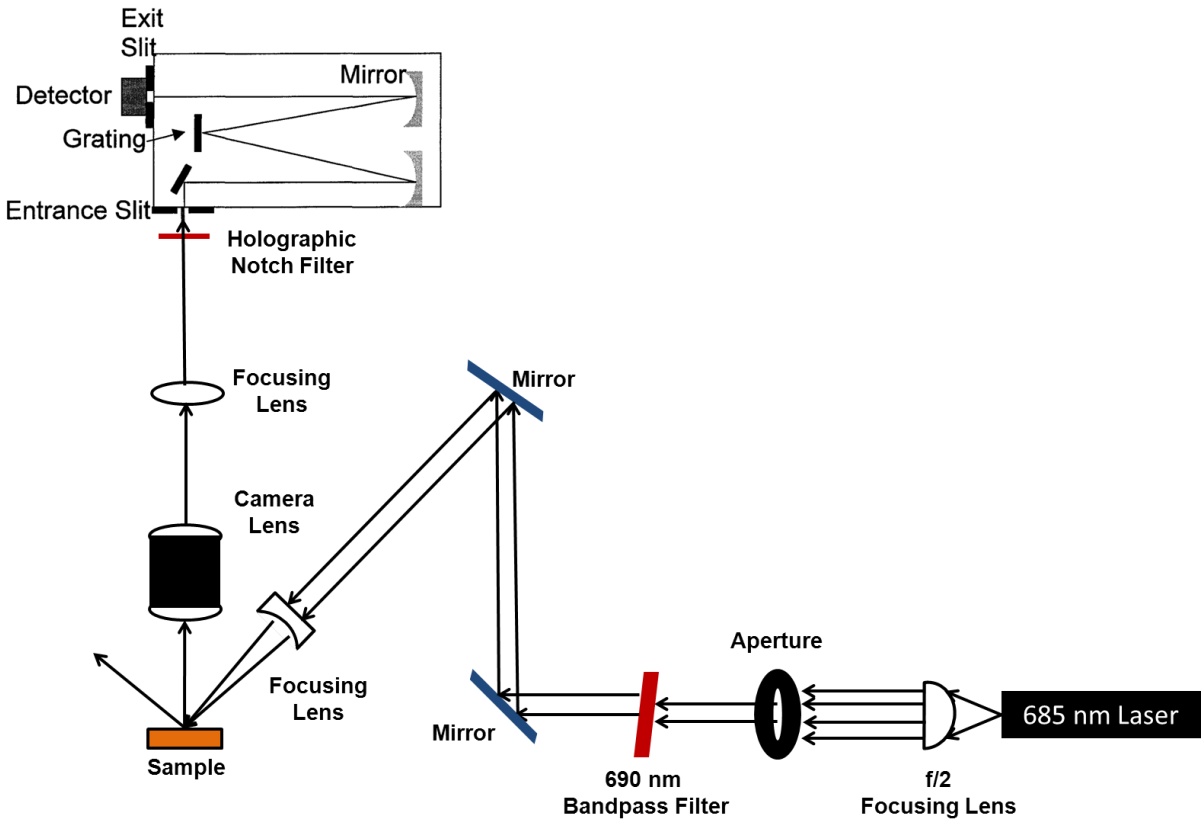

Figure A.1: Experimental Raman setup using the Newport 685 nm laser system

First, the beam needs to be collimated. This is achieved using an f/2 focusing lens placed roughly 1 inch from the laser source. The exact position of the lens relative to the laser can be adjusted as needed to achieve a well collimated beam. There are two sets of divergent beams that become apparent as the central beam is collimated. In order to filter out the outer ring of more divergent light, a medium sized iris aperture is placed after the f/2 focusing lens to only allow the central beam to pass. The beam diameter is roughly ½ inch when the system is set up as described. This beam is then directed through a bandpass filter to remove any abberant light

not centered at 684.6 nm. No bandpass filters are readily available for 685 nm light, so a 690 nm interference bandpass filter has been modified to allow 684.6 nm light to pass.

In order to allow 684.6 nm light to pass, the 690 nm filter (ThorLabs, FB690-10) needs to be tilted away from the perpidicular orientation by 14.6°. This is determined by the following equation:

$$\frac{\lambda_{\Phi}}{\lambda_0} = \frac{\sqrt{N^2 - sin^2\Phi}}{N}$$

λ_{Φ} is wavelength at the angle of incidence Φ (685 nm). λ_0 is wavelength at 0° off of normal (690 nm). N is the effective refractive index (2.1).

After passing through the bandpass filter, the collimated beam is directed off of two mirrors toward the sample surface. Before reaching the surface, the beam is focused again, as with the other laser systems. Scattered light from the surface is then collected with a camera lens and focused with a focusing lens toward the entrance slit. The only other difference when compared to the other laser systems is the use of a different notch filter. A specialty holographic notch filter from Kaiser Optical Systems (HSNF-685.0-1.0, SuperNotch filter). This filter is placed as close as possible to the entrance slit of the spectrometer.

Appendix B. VASP and GoVASP User Guide

Introduction:

This guide describes how to use VASP (Vienna ab-initio simulation package) and GoVASP in Room A504 CLSL. VASP 5.2x license is provided by Prof. Jurgen Hafner of the University of Wien, Austria. GoVASP is a graphical user interface provided by Windiks Consulting. Further updates and support for GoVASP are no longer possible as it has been integrated into the Medea software environment sold by Materials Design.

Most general questions regarding the VASP 5.2.x code or the GoVASP GUI can be addressed by the VASP user manual printed in the lab or at the address http://cms.mpi.univie.ac.at/vasp/vasp/vasp.html. This guide describes the setup parameters and provides example systems to demonstrate how these parameters are implemented. Further support through the VASP website at www.vasp.at is available with the VASP Forum as well as VASP workshop lectures within the Documentation section to explain some of the theory behind VASP. GoVASP support is no longer available online. The GoVASP user guide can be found within the help menu of GoVASP. This guide describes the basic functions of GoVASP and how to perform some of the types of calculations. It also describes the operational hierarchy of the GUI, Jobserver, and Taskserver.

Launching and Operating GoVASP:

1. Turn on the VASP computer and allow it to boot up in the Linux operating system. Windows can be reached by interrupting the boot process when prompted and choosing Windows 7.
2. Login as govasp with the password afms10.
3. Once logged in as govasp, enter the ‘computer’ icon, followed by ‘filesystem’, then ‘opt’, the ‘govasp’. GoVASP may be executed from this folder by entering ‘GoVASP’. When prompted, choose to ‘run in terminal’.

4. Once the GoVASP GUI launches, the user will need to also launch VASP. VASP 4.6 is the most current version that GoVASP supports. To launch, select 'Tools' and choose VASP 4.6 from the drop menu.
5. The user is now ready to construct or import a model to investigate. To construct a model, go to 'File' and then 'New'. A blank cell is created whose dimensions and space group can be changed. Atoms are then added by right clicking and selecting 'Add atom'. Atoms can be added, moved, or frozen in this manner.
6. Premade structures are available within the GoVASP GUI by selecting 'File' and then 'Open'. The User can select a file from disk for most commonly studied materials such as metals, or can select a cell from a previous calculation when prompted.
7. When a model is constructed, VASP calculations can be setup and performed in Single Point Energy, Structural Optimization, or Molecular Dynamics modes after selecting 'VASP 4.6' from the top menu. Once parameters are chosen, the task can be submitted to either the local taskserver, with 1 processor, on the VASP computer, or to the Triton server operating by Computer and Networking Services, which has 32 processors running in parallel.
8. Jobs can be controlled by selecting 'Job Control' from the top menu followed by 'View and Control Jobs'. This gives access to the Jobserver and the Taskserver to monitor progress and view raw results from VASP calculations.
9. Analysis of previous calculations is available from the 'Analysis' tab in the top menu.
10. Visualization tools are also available to generate images of cells or surfaces in order to convert to picture files. Under 'View' in the top menu, the user can choose 'export to POV-Ray', which will generate a picture of the desired image for use in making figures. Exported images are saved in the "govasp's home" folder on the desktop. Further modification of the generated files can be conducted by choosing 'Applications' from the desktop top menu, followed by 'Graphics', followed by 'The GIMP'. POV-Ray images tend to provide poor contrast between certain colors and The GIMP is used to improve visibility and contrast between atoms.